Alma Mater Studiorum - Università di Bologna

SCUOLA DI SCIENZE
Dipartimento di Chimica Industriale "Toso Montanari"

Corso di Laurea Magistrale in
Chimica Industriale
Classe LM-71 - Scienze e Tecnologie della Chimica Industriale

Supported metal nanoparticles for sustainable green catalytic processes

Tesi di laurea sperimentale

CANDIDATE
Francesca Martelli

SUPERVISOR
Prof. Stefania Albonetti

CO-SUPERVISOR
Prof. Nikolaos Dimitratos
Eleonora Monti

Session III

Academic Year 2018/2019

CONTENT

SCOPE

Nanostructured catalysts composed by metal nanoparticles supported and stabilized by a variety of materials have proven to be a promising class of materials[1], able to perform a wide range of reactions[2]. Nanoparticle preparation has been widely studied the last 30 years and now several methods are available to obtain the desired combination in nanoparticle size, shape and metal-support interaction. Amidst this variety, the supported nanoparticles used for catalytic purposes in this study were prepared following two of the available methods. One is generally known under the name of sol immobilisation (SI) and the other is cluster beam deposition (CBD)[3].

A CBD novel technique available at Swansea University (UK), under the name of "matrix assembly cluster source" or MACS, was used to prepare Ag and Au nanoclusters supported on commercial TiO_2 as the first materials ever prepared with a new machine that aims to a production of 1g of catalyst/hour. Ag/TiO_2 and Au/TiO_2 were characterized by TEM imaging, XPS, ICP-AES, and BET. The materials were tested for the catalytic mineralization of 4-nitrophenol, a model pollutant in industrial and urban wastewaters, with ozone[4]. The same materials were also tested for 4-nitrophenol reduction with $NaBH_4$ to 4-aminophenol. This reaction represents another pathway to the transformation of 4-NP to a less harmful molecule and, most importantly, in recent years has become a model reaction for the evaluation of metal nanoparticle catalytic activity[5].

Sol-immobilization technique was used to synthesize a range of Au nanoparticles supported on active carbon and TiO_2, varying the stabilizer and the stabilizer concentration in respect to Au. The polymeric stabilizers investigated were polyethylene glycol (PEG), polyvinyl pyrrolidone (PVP) and polyvinyl alcohol (PVA).

These materials were characterized by ultraviolet-visible (UV-vis) spectroscopy, dynamic light scattering (DLS) analysis, x-ray diffraction (XRD), and transmission electron microscopy (TEM) imaging. The prepared materials were studied as catalysts for two reactions, glucose oxidation to glucaric acid and 4-nitrophenol reduction to 4-aminophenol, to discuss the effect of the stabilizing agent nature and concentration in respect to the metal nanoparticles on the catalytic activity of Au nanoparticles supported on AC. Eventually, TiO_2 was used as support for Au nanoparticles in comparison to AC-supported Au NPs to investigate the effect of nanoparticle-support interactions.

Abbreviations

4-NP: 4-nitrophenol

AC: activated carbon

BET: Brunauer-Emmett-Teller

CBD: cluster-beam deposition

DLS: dynamic light scattering

HAADF: high-angle annular dark field

HPLC: high-performance liquid chromatography

ICP-AES: inductively coupled plasma atomic emission spectroscopy

kapp: apparent reaction rate

MACS: matrix assembly cluster source

NPs: nanoparticles

PEG: polyethylene glycol

PVA: polyvinyl alcohol

PVP: polyvinyl pyrrolidone

SPR: surface plasmonic resonance

STEM: scanning transmission electron microscopy

UV-vis spectroscopy: ultraviolet visible spectroscopy

TEM: transmission electron microscopy

XPS: x-ray photoemission spectroscopy

XRD: x-ray diffraction

1. Introduction

1.1. Nanomaterials in catalysis

Catalysis by nanomaterials has been known for a long time. Looking back, it is possible to notice that 60 years ago catalysts with a nanometric structure were already regularly prepared, either being nanometric metallic crystallites or zeolites with nanopores, where size effect was acknowledged and exploited advantageously[1]. It was known that the position of metal atoms in the crystallite (edge, corner, facets) could show different reactivity and this allowed to establish structure-reactivity correlations with the techniques available at the time, such as transmission electron microscopy and chemisorption of gases, which were nevertheless of a very different resolution from today's instrumentation[6].

Over the years, nanomaterials have gained an increasing interest from the scientific community for the potential in a wide range of applications, such as non-linear optical materials[7], microelectronics [8,9], energy harvesting[10], and catalysis[11]. It resulted in the development of synthesis methods able to deliver metal nanoparticles with a very narrow nanoparticle size distribution, and of adequate characterisation techniques such as X-ray photoemission spectroscopy and aberration-corrected transmission electron spectroscopy[12].

One of the main reasons of using metal nanoparticles is mainly due to the possibility to modify optical, electronic, mechanical, redox and catalytic properties by controlling the morphology in terms of particle size and shape. This particular size effect is explained by orbital theory[13]. Group VIII metals, copper (Cu), silver (Ag) and gold (Au), have the d-band fully occupied. As the vacancies of the d-band is generally known to be responsible for catalytic activity of other transition metals, copper, silver and gold were seen as catalytically inert or with low catalytic activity as bulk materials in their metallic state. Thanks to two independent researchers, prof. M. Haruta[14] and prof. G. J. Hutchings[15], and their parallel discoveries on gold catalytic activity when the particles' size falls below the 10 nm scale[16], a new path was opened.

1.2. Preparation methods

Nanoparticle preparation has been widely studied the last 30 years and now several methods are available to obtain the desired combination in nanoparticle size, shape and metal-support interaction. Amidst this variety, the supported nanoparticles used for catalytic purposes in this study were prepared following two of the available methods. One is generally known under the name of sol immobilisation (SI) and the other is cluster beam deposition (CBD).

1.2.1. Sol immobilisation

Sol immobilisation (SI) is a method that was introduced for the first time by Prati and Martra in 1999 to overcome some of the challenges posed by previously established gold nanoparticle preparation methods[17]. One of their aims was to synthesise nanoparticles with controlled nanoparticle size, less sensitive to pH and to extend the range of usable supports and increase overall control over nanoparticle size, shape, metal-support interaction and final morphology (including also the control of oxidation state of the nanoparticle).

Sol immobilisation consists in forming the metallic nanoparticles as a sol prior to immobilising them onto a support, therefore synthesising preformed metal nanoparticles. The sol is formed by reacting a metal inorganic precursor, such as $HAuCl_4$, with a reducing agent with weak, mild or strong reducing power, like sodium citrate, sodium borohydride or molecular hydrogen. Sometimes, the reducing agent can also act as a stabiliser to prevent nanoparticle aggregation and agglomeration, as with sodium citrate (electrostatic interaction). The method is also known under the name of Turkevich's method and is based on the electrostatic stabilisation the citrate ions provide to the nanoparticle (figure 1).
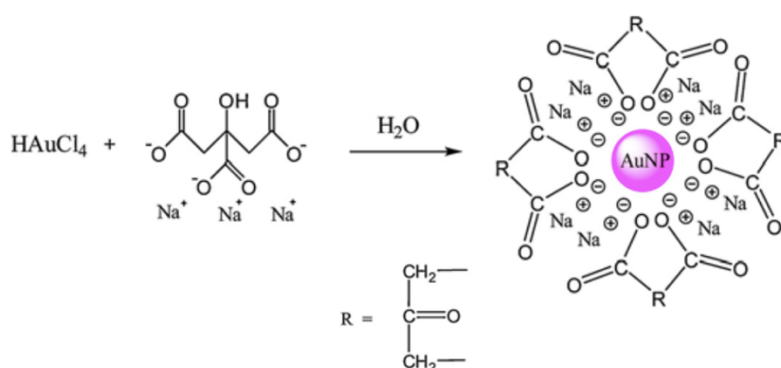
Figure 1 – Gold nanoparticle formation and stabilisation by Turkevich's method: citrate ions first reduce gold precursor to Au(0); the excess citrate ions surround the formed Au nanoparticle thanks to electrostatic interactions.

Ions in solution are attracted to the metal nanoparticle, easily polarisable, and form an electric double layer that leads the stabilised nanoparticles to repel each other. Another way to control nanoparticle formation is with sterical stabilisers. In this category are found polymeric macromolecules such as poly(vinyl pyrrolidone) (PVP) and poly(vinyl alcohol) (PVA). In this case the stabilisation is provided by the polymers that act as a template for the nanoparticles, keeping the distance from one another and preventing precipitation.
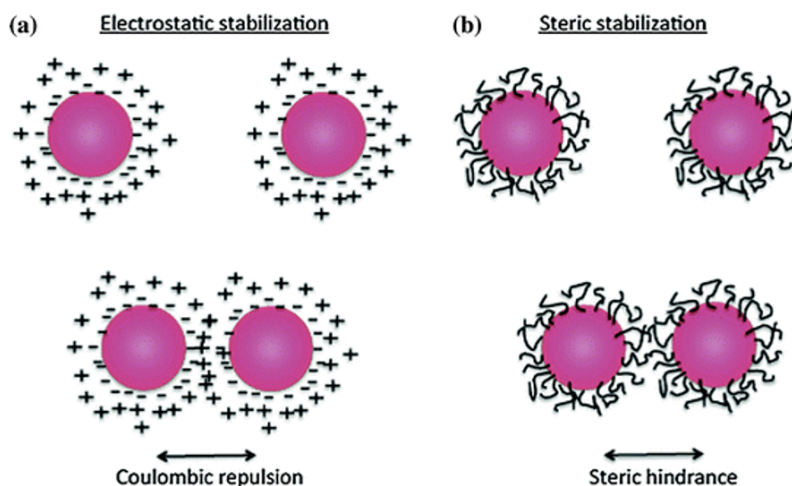
Figure 2 – Metal nanoparticle stabilisation can be a) electrostatic, where columbic repulsion pushes nanoparticles apart avoiding coalescence, or b) steric, where long-chained molecules such as polymers or proteins surround the metal nanoparticle acting like a shell.

Steric stabilisation is preferred rather that electrostatic because the latter is sensitive to ionic strength and pH changes in the colloidal solution. Adding a strong electrolyte such as NaCl to a citrate-stabilised Au colloidal solution can easily cause agglomeration and precipitation of the gold nanoparticles. Steric stabilisation is stronger, and agglomeration is minimised over a wider range of experimental conditions. A combination of steric and electrostatic stabilisation is found in polymers with charged functional groups, like polysaccharides[18] or poly methylacrilate (PMA)[19].

Another advantage of pre-forming the nanoparticles is given by the control on their shape. Recent studies[20] showed that it is possible to obtain gold nanocrystals with different shapes (octahedra, rhombic dodecaherda, cubes) by changing the ionic environment of growth. Other experimental parameters that influence nanoparticle morphology are: metal concentration, stabilising agent concentration, and reducing agent[21,22].

Once the nanoparticles are formed, it is possible to support them to obtain the final catalyst. Immobilisation of the nanoparticles on the support is carried out by lowering the pH of the solution below the support's isoelectric point to favor electrostatic interactions between metal nanoparticles and support. The presence of polymers surrounding the metal nanoparticles doesn't limit the immobilization step, but rather prevents nanoparticle agglomeration and enhances long-term stability of the supported nanoparticles.

1.2.2. Cluster beam deposition

Cluster beam deposition is a physical vapour deposition method that allows to synthesise metal clusters in a vacuum environment, hence resulting in a solvent-free preparation. In this method, the starting material is vaporised from a hot source, either by Joule heating (thermal), thermal plasma or laser ablation. Metal cluster formation is due to homogeneous nucleation of the supersaturated vapor

and particle growth happens by condensation and coagulation of metallic atoms[23]. Therefore, the difference of CBD compared to chemical preparations is the production of ultraclean clusters, not needing any stabilising ligands[3], hence allowing the study of the intrinsic catalytic properties of the materials so prepared. Another great advantage that CBD methods bring forward is the possibility to generate sub-nanometric metal clusters containing 1-500 metal atoms[24], a target almost impossible to reach by wet chemistry methods.

There are many types of cluster sources that work on the principles of CBD, the majority of which rely on the coupling of the cluster source to a carrier gas that also acts as a thermal bath for cooling[23]. A good control in size, shape and composition is normally available for bimetallic nanoclusters. For example, magnetron-sputtering is a cluster source that has the capability to synthesise multimetallic nanoclusters via the use of two or more starting materials[3]. However, traditional CDB techniques all present the same disadvantage: scalability is a hard task. A conventional cluster source can attain a cluster beam deposition rate of 0,05 -0,5 µg Au_{100} clusters/h, implying that in order to obtain 1 g of 1 wt% metal loading (10 mg of Au_{100} clusters) a prohibitive amount of time is required.

In order to overcome this drawback, a new cluster source - the Matrix Assembly Cluster Source (MACS) (figure 3) - was invented by Palmer and coworkers and it is currently being developed by the Nanomaterials Lab in Swansea University (UK), with the aim of reaching a deposition rate of 1g of catalyst per hour, or 10 mg Au_{100} clusters/h.
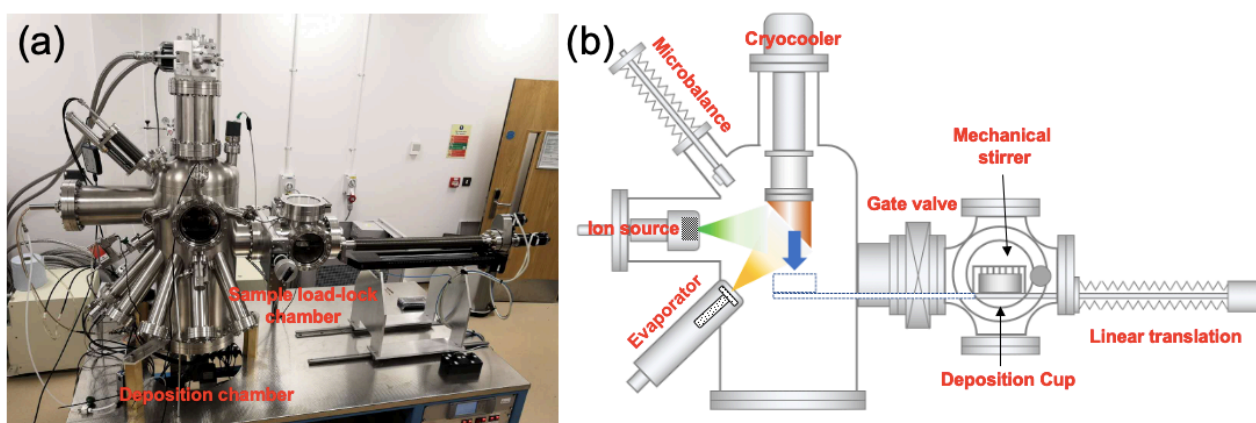
Figure 3 – a) Photograph and b) schematic diagram of the MACS system for the preparation of cluster catalysts

The formation of metal clusters in the MACS technique can be divided in two consecutive moments (figure 4). First of all, a solid matrix of inert gas atoms (normally Ar) containing metal atoms is formed. The inert gas is admitted into the matrix chamber and directed towards a surface cooled to a temperature around 15 K due to a continuous-flow liquid helium cryostat. The low temperature is needed in order to condense the Ar atoms on it. At the same time, metal atoms are evaporated from the starting material, e.g. bulk Ag bars of purity 99,99%, using a thermal evaporator towards the same cryo-cooled surface. The result is an Ar three-dimensional solid matrix in which metal atoms are

embedded. Once the desired thickness of the matrix is reached, evaporation and condensation are stopped, and the following step is cluster formation. An ion beam (Ar^+) impacting the matrix is used to start a cascading process of collisions that lead to the coalescence of the metal atoms.
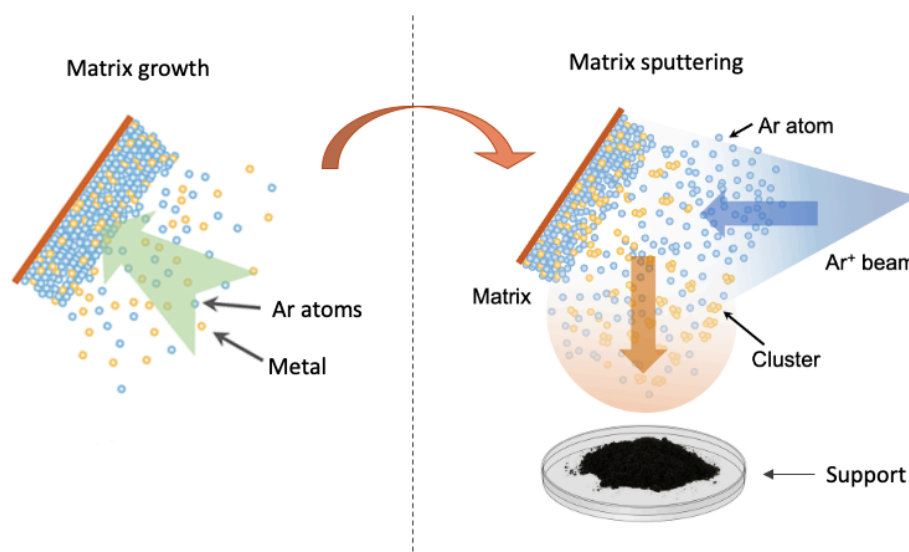
Figure 4 – Matrix growth by condensation of metal and Ar atoms on the cryo-cooled support; following, the matrix is sputtered by Ar+ ions causing melting of the Ar matrix and cascading impacts between the metal atoms. The produced

The ripened clusters sputtered out of the matrix are collected on the support, which can be either a powder or a flat surface. Cluster size and rate deposition are respectively controlled by the concentration of metal atoms in the matrix and the ion beam current, as roughly 1 cluster is emitted per 100 Ar^+ ion impacts. For an Ag metal concentration of 2,3% in the Ar matrix, Ag clusters of about 200 atoms were obtained; as the metal loading in increased to 3,6%, the produced Ag clusters contain in average about 350 atoms[25].

1.2.3. Other methods: impregnation, co-precipitation, deposition-precipitation

Supported nanoparticle preparation started from more classical preparation methods such as impregnation and co-precipitation.

Impregnation method starts from a solution containing the desired amount of metal precursor, generally a metal salt. The volume of solvent in which the metal precursor is dissolved is equal to the total pore volume of the support (incipient wetness point). Once all the precursor solution is mixed to the support, a thick paste is obtained. Once the solvent is evaporated, the supported metal precursor is reduced to the metallic (0) state and nanoparticles are formed. Though, this method is not apt for the preparation of highly dispersed Au catalysts, as the average nanoparticle size is normally above 10 nm. This effect is owed to the presence of Cl^- ions on the support surface deriving from the Au precursor, $HAuCl_4$, that causes Au nanoparticles to aggregate[26,27].

An early alternative to impregnation was co-precipitation, a popular technique to produce mixed metal oxides. Carbonates or hydroxides of the desired metals are precipitated by addition of aqueous alkali (NaOH, Na_2CO_3, or K_2CO_3) to a solution of soluble metal salts. Metal oxides are obtained by calcination in air. Co-precipitation can be used to prepare Au nanoparticles because $Au(OH)_3$ during the calcination treatment in air is reduced to metallic Au, forming gold nanoparticles, while the other metal hydroxides are converted to the respective metal oxide. This technique is applicable to the formation of well-dispersed Au nanoparticles on MnO_2, Fe_2O_3, ZnO, NiO, Co_3O_4[26], characterised by robust nanoparticle-support interaction[26]. Au nanoparticle average size can be moderately controlled through the calcination temperatures, as lower temperatures give smaller nanoparticles.

For those metal oxides that cannot be easily obtained through precipitation, such as Al_3O_3 and TiO_2, an alternative method was developed: deposition-precipitation. Here, an aqueous suspension of the support medium and an aqueous solution of the metal precursor salt are mixed; the pH is increased until the metal hydroxide precipitates, the support particles acting as nucleating agent. The as obtained material can be calcined in air and reduced, if needed, to obtain the final supported metal nanoparticles.

1.3. Examples of catalytic reactions by nanoparticles

A considerable place in heterogeneous catalysis is occupied by supported gold nanoparticles as it has been proved to be a powerful and versatile catalyst for a variety of reactions that include CO oxidation, alcohol oxidation, reduction of nitro derivatives to aniline derivatives, hydrogenation of C=C bonds and several others[2].

The first reaction that saw the application of gold nanoparticles as an heterogenous catalyst was CO oxidation to CO_2 in atmospheric air. This reaction is particularly valuable for environmental applications as it allows the conversion of a toxic compound in air to a harmless one without the loss of the valuable H_2. Another great advantage of this reaction is that it can operate at low temperature[16], from ambient conditions down to -76˚C. A thorough study of this reaction led to many significant findings on gold nanoparticle catalysis, among which the conclusion that the support plays a fundamental role in catalytic activity. It was reported that Au NPs supported on activated carbon or polymers such as PMMA are substantially inactive for CO oxidation even at higher temperatures above 373 K. At the same time, metal oxides are excellent supports as gold nanoparticles and clusters deposited on TiO_2, α-Fe_2O_3, Co3O4, NiO, $Mg(OH)_2$ and $Be(OH)_2$ are highly active[28].

In the field of organic chemistry, alcohol oxidation in water by supported gold nanoparticles discovered by Prati et al.[17] sparked another stream of research. Au NPs allow a green approach to this reaction that is of fundamental importance to industry. Traditional oxidants are not only toxic but are

needed in stoichiometric amounts, whilst metal nanoparticles anchored to a support are easily recoverable and rely on molecular oxygen as the oxidant[29]. The research in this area focuses on controlling not only activity but most importantly selectivity, for the partial oxidation of primary alcohols to aldehydes needs a delicate balance between the two. The efforts deployed by many researchers have produced a huge variety of combinations of supports and catalyst morphologies, from traditional C, SiO_2, zeolites to more advanced MOFs, CNTs and nano oxides.

Hydrogenation of C=C bonds and more generally of π-π systems (alkenes, dienes, alkynes, and aromatics) by gold nanoparticles is another application that has been widely investigated. In particular, the selective hydrogenation of alkynes to alkenes by metal oxide supported Au NPs shows a selectivity of 100% towards C_2H_4 even in presence of C_2H_4 in the feed[30]. It was demonstrated that a non-competitive adsorption of C_2H_2 and C_2H_4 on the surface of Au NPs is the key point for such selectivity. In explanation, the C-C triple bond of acetylene is specifically adsorbed on the edge sites of Au_{19}, which does not happen for the C-C double bond counterpart. These results were demonstrated by DFT (density functional theory) calculations and experiments over Au/CeO_2 and represent a turning point from the traditional Pd-based catalysts. As a matter of fact, Pd adsorbs unselectively double and triple bonds. Hence, Au-based catalysts represent a promising replacement for acetylene removal from C2 and C3 cuts from steam crakers[31].

Generally speaking, AuNPs-based catalysts seem to offer a cleaner route toward the obtention of many intermediates at the base of chemical industry. PO (propylene oxide) synthesis from propylene, molecular O_2 and H_2[32], methyl methacrylate by oxidative esterification of methacrolein[33], vinyl chloride monomer from a mercury-free acetylene hydrochlorination, are just a few of the crucial processes that are being utterly renovated thanks to this new set of knowledge.

1.4. Reactions in this study
1.4.1. Catalytic 4-nitrophenol reduction by sodium borohydride

The reduction of 4-nitrophenol by $NaBH_4$ is considered as a model reaction for evaluation of catalytic activity by gold-based nanoparticles as it does not proceed in absence of catalyst[34]. Moreover, the only product of this reaction od 4-aminophenol and the kinetics can be treated in terms of the Langmuir-Hinshelwood (LH) model, as is has been showed that both reactants adsorb on the catalyst surface before the reaction[35]. The competition of the reactants for the active sites on the nanoparticle surface was indicated by a decrease in the rate constant as 4-nitrophenol concentration is increased and by the presence of a maximum in the rate constant when increasing the $NaBH_4$ concentration

(pseudo first-order rate constant (k_{app}) due to the presence of excess $NaBH_4$ compared with nitrophenols).

As first step, the borohydride ion decomposes to give activated hydrogen on the Au nanoparticle surface, and $B(OH)_4^-$. Then, the adsorbed 4-NP reacts with the Au-H bonds in what is considered to be the rate-limiting step, to give the 4-amminophenol and H_2O. The reduction reaction could be summarised in the following equation[5] (figure 5).

$$4 \; \text{(4-nitrophenol)} + 3 \; NaBH_4 \xrightarrow{\text{Nano-gold catalyst}} 4 \; \text{(4-aminophenol)} + 3 \; NaBO_2 + 2 \; H_2O$$
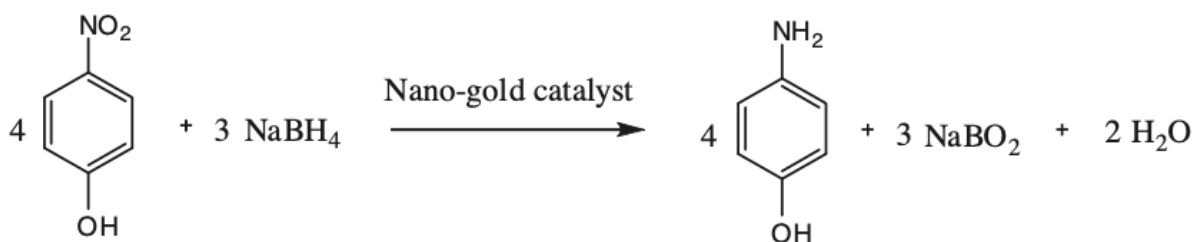
Figure 5 – Chemical equation for 4-nitrophenol reduction by sodium borohydride catalysed by gold nanoparticles.

The nitro group adsorbs on the nanoparticle by delocalisation of the electrons from the oxygen atoms to the nanoparticle surface, weakening the O-N bonds as represented in figure 6. Once the nitro group has been reduced to its corresponding amine, the molecule desorbs from the surface.
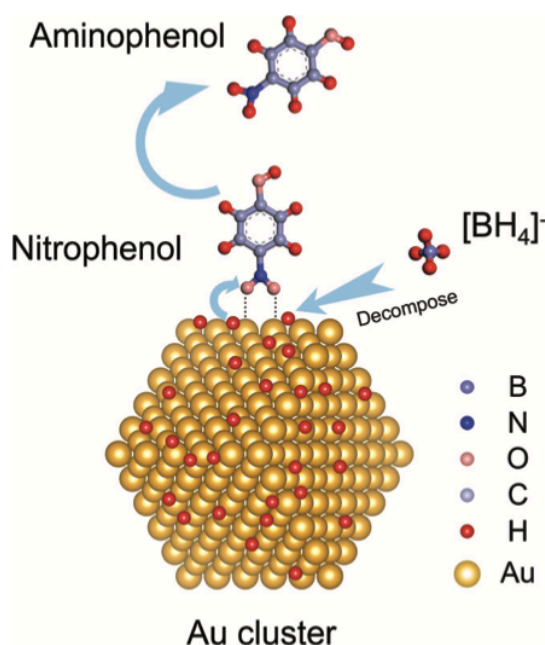
Figure 6 – Schematic representation of the reduction of 4-nitrophenol by NaBH4 on the Au nanoparticle surface by adsorption of the reactants following a Langmuir-Hinshelwood model.

Since this reaction has become a model reaction for the evaluation of Au nanoparticle catalytic activity, there are a great number of studies where this reaction has been applied to Au nanoparticles varying support, stabilisers, catalyst morphology, anisotropy of nanoparticles (table 1).

Metallic NP	Support or stabiliser	NaBH$_4$ (eq.)	k$_{app}$ (s^{-1})	Comment	ref
Au	Polymer, PEO-b-PPA	300	$9,5*10^{-3}$	The hydrophilic block co-polymer acts as template for Au nanoparticle synthesis.	[36]
Au	Dendrimer, PPI	100	$1,47*10^{-2}$	Catalytic activity is influenced by concentration of dendrimers.	[37]
Au	Carbon, r-CD	75	$9,75*10^{-4}$	Carbon dots (CD) can reduce and stabilize Au NPs during their synthesis, but a lack of surface available on Au NPs hinders the catalytic activity.	[38]
Au	Oxide, Fe$_3$O$_4$@TiO$_2$	80	$1,03*10^{-2}$	Magnetic Fe$_3$O$_4$ core for magnetic separation, double TiO$_2$ shells with encapsulate Au NPs.	[39]
Au	Anisotropic, Au nanocages	300	$9,3*10^{-2}$	Hollow structures, superior catalytic activity due to confinement of reactants inside the cavity.	[40]
Ag	Carbon, GO	114	$3,5*10^{-3}$	Lower cost than Au, but also less active.	[41]
Cu	NC s	165	$8,2*10^{-3}$	Shows good catalytic properties but has a tendency to oxidise to CuO.	[42]
Pd	Graphene	100	$2,35*10^{-3}$	Pd NPs show increased catalytic activity towards 4-NP reduction that Au NPs but have toxicity problems.	[43]
Au-Pd	Spherical polyelectrolyte brushes (SPB)	Excess	$2,9*10^{-3}$	Alloyed nanoparticle size in 1 to 3 nm range showed higher catalytic activity that monometallic Au or Pd NPs.	[44]

Table 1 – Comparison of various metallic nanoparticles (Au, Ag, Cu, Pd and bimetallic Au-Pd) as catalysts for the reduction of 4-nitrophenol from literature.

1.4.2. 4-nitrophenol degradation by O$_3$

Advanced oxidation processes (AOPs) are a method to generate strong oxidant species *in situ*. These mainly include •OH radicals, but also other oxidizing species based on sulphate and chlorine radicals. They have long been studied especially for drinking water which needs to be cleaned from micro-organisms and polluting chemicals, namely pharmaceuticals and hormones. Those substances pose the difficulty of being found in traces, so traditional physical and biological methods are often ineffective[4]. The model pollutant used in this study was 4-nitrophenol. Its source being mainly industrial wastewater, nitrophenols and nitroaromatic compounds in general represent a risk for human health and environment[45]. Their toxicity slows biodegradation down as it causes damage to microorganisms, so other methods are needed in order to mineralise nitrophenols and other trace organic pollutants[46–48]. Exposure to 4-NP represent a risk to human health, as it can cause damage to blood cells and the central nervous. The Environmental Quality Standards Directive produced by the European Commission in 2006 set the acceptable 4-NP concentration to 100 µg/L in surface water near industrial and urban areas. An investigation of polar organic pollutants in european rivers, where 122 samples from 27 watercourses were analysed[49], 4-NP was detected in 97% of the samples with a maximum concentration of 3741 µg/L.

Therefore, there is a need to remove 4-NP from wastewaters to keep its concentration below the prescribed limits, to safeguard the environment and human health.

Gu et al. studied the degradation of 4-NP in water by O_3 and activated carbon[50]. They identified reaction intermediates including aromatic compounds and low-mass acids that allowed to propose the reaction mechanism in figure 7. They observed that the AC-promoted radical oxidation of 4-NP occurred primarily at basic pH, by addition of a radical scavenger and carrying out the reaction at pH 4 and 10. The reaction rate at pH 10 showed a significant decrease upon addition of radical scavenger, whereas the reaction rate at pH 4 was unchanged. Hydroxyl radicals are then to be considered the principal actor in advanced oxidation of 4-nitrophenol.
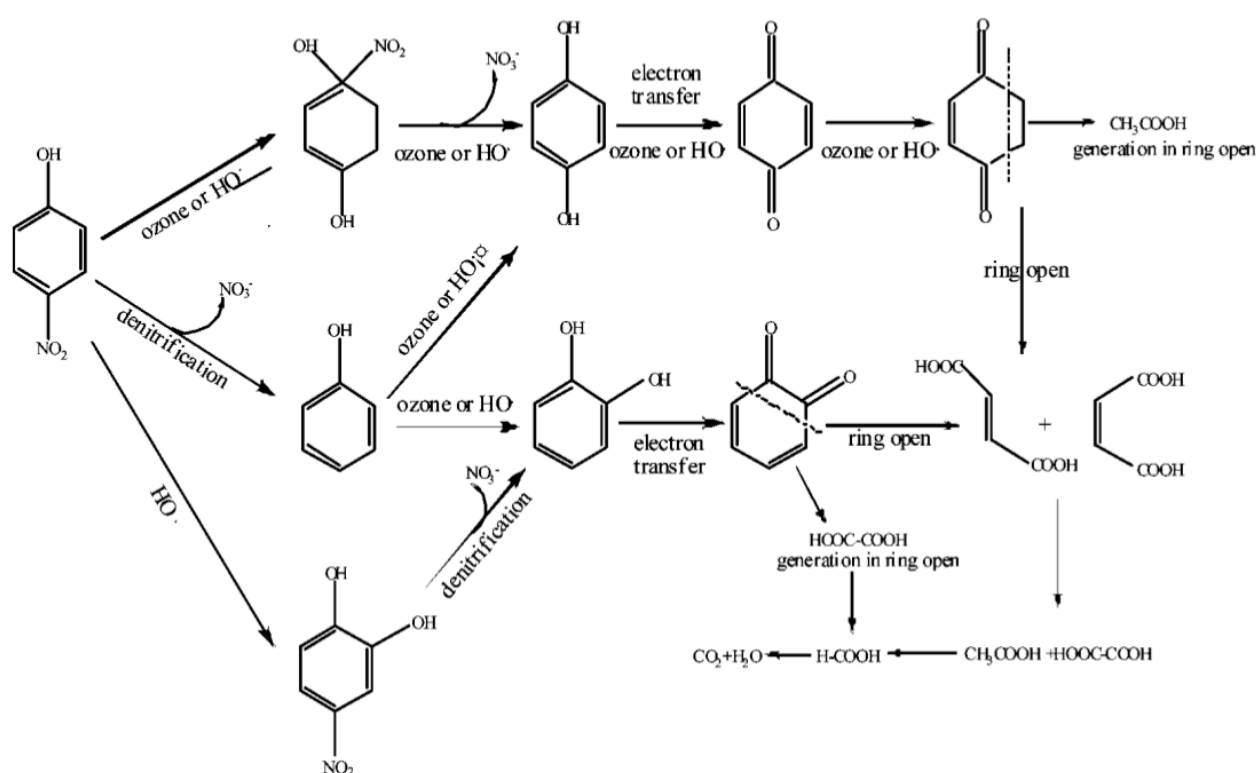
Figure 7 – Proposed reaction pathway for 4-nitrophenol degradation by means of ozone-based advanced oxidation.

Ozone-based AOPs involve the formation of ˙OH radicals at a high rate. Indeed, ozone decomposition in aqueous environment already produces ˙OH radicals[51]. However, the rate of ˙OH formation is rather slow and prevents a substantial contribution of hydroxyl radicals to organic chemicals degradation, although reaction conditions definitely can influence ozone decomposition mechanisms and kinetics[52,53].

Catalytic ozonation is an AOP which relies on catalysts, which can be either heterogeneous or homogeneous, in order to enhance hydroxyl radical formation[54]. Typically, homogeneous catalytic ozonation is described by many as a cycle where a transition metal ion changes its oxidation state[48,55]. Although those mechanisms are now clarified, homogeneous catalysts always present

the problem of recovery, which is avoided if the catalyst is heterogeneous. Heterogeneous catalytic ozonation, on the other hand, is based on more complex mechanisms that lack a true insightful understanding. Albeit, their reaction paths in terms of multiple-phase mass transfer mechanisms are explained in detail by Beltrán[56].

Metal oxides have been investigated particularly as catalysts for ozone decomposition in water[54,57–59]. In a previous work, J. Lin and coworkers reported a systematic study of metal oxides and transition metals to find the combination that would show the highest activity[60]. Silver supported on TiO_2 was found to be among the most active metals, just after the very costly platinum and palladium. The oxidation state of the metal, in that work, was not object of investigation. In any case it was reported[61] that redox catalysts (which comprised silver) are effective for ozone decomposition as they can interact with oxygen relatively easily allowing them to form reactive complexes. In that particular case, the silver-based catalyst was in the state of Ag_2O.

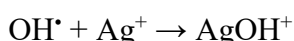As ozone is a strong oxidant, even if silver was in metallic state it would be immediately oxidized. Other studies[62,63] reveal that oxidation states of silver can interact with ozone, albeit through a variety of mechanisms, and produce a range of reactive chemicals such as superoxides and hydroxyl radicals:

$$O + Ag^0 \rightarrow O_3^{-\bullet} + Ag^+$$
$$O_3 + O_3^- \rightarrow O_2^{-\bullet} + 2\,O_2$$
$$O_3 + O_2^- + H_2O \rightarrow 2\,O_2 + OH^\bullet + OH^-$$
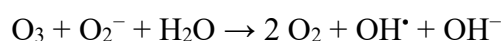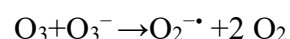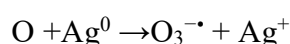
Chain termination reaction:

$$OH^\bullet + Ag^+ \rightarrow AgOH^+$$

1.4.3. Glucose oxidation

Glucose is a common monosaccharide in nature and can be obtained by hydrolysis of cellulose and starch. Cellulose and starch are found in vegetal sources, such as corn, wheat or sugar cane that are rich in carbohydrates, and from ligno-cellulosic biomasses, that supply cellulose, hemi-cellulose and lignin. These vegetal sources fall under the category of biomass, which can be used as renewable feedstock for the production of chemicals and fuels. The breakdown of cellulose and starch can give glucose, while hemi-cellulose and lignin can give a variety of C5-C6 sugars and phenolic compounds. Glucose is an extremely versatile molecule. By means of chemical and bio-technological transformations, a plethora of valuable chemicals can be obtained from glucose, as depicted in figure 8. Glucose transformation poses several challenges. In chemical transformations, selectivity to the desired product is a major issue that calls for a new generation of catalysts that can discriminate with a high level of precision between functional groups and positions on the carbon chain of the molecule,

hence tailored chemo- and regio-selectivity. Bio-technological transformations are usually expensive and difficult to scale up. Nevertheless, some processes were developed over the last years: gluconic acid, an oxidized product of glucose, is obtained by submerged fermentation with *Aspergillus niger* in a production that reached $6 *10^4$ tons per year[64] due to its use as chelating agent and raw material for pharmaceutical and food industry.
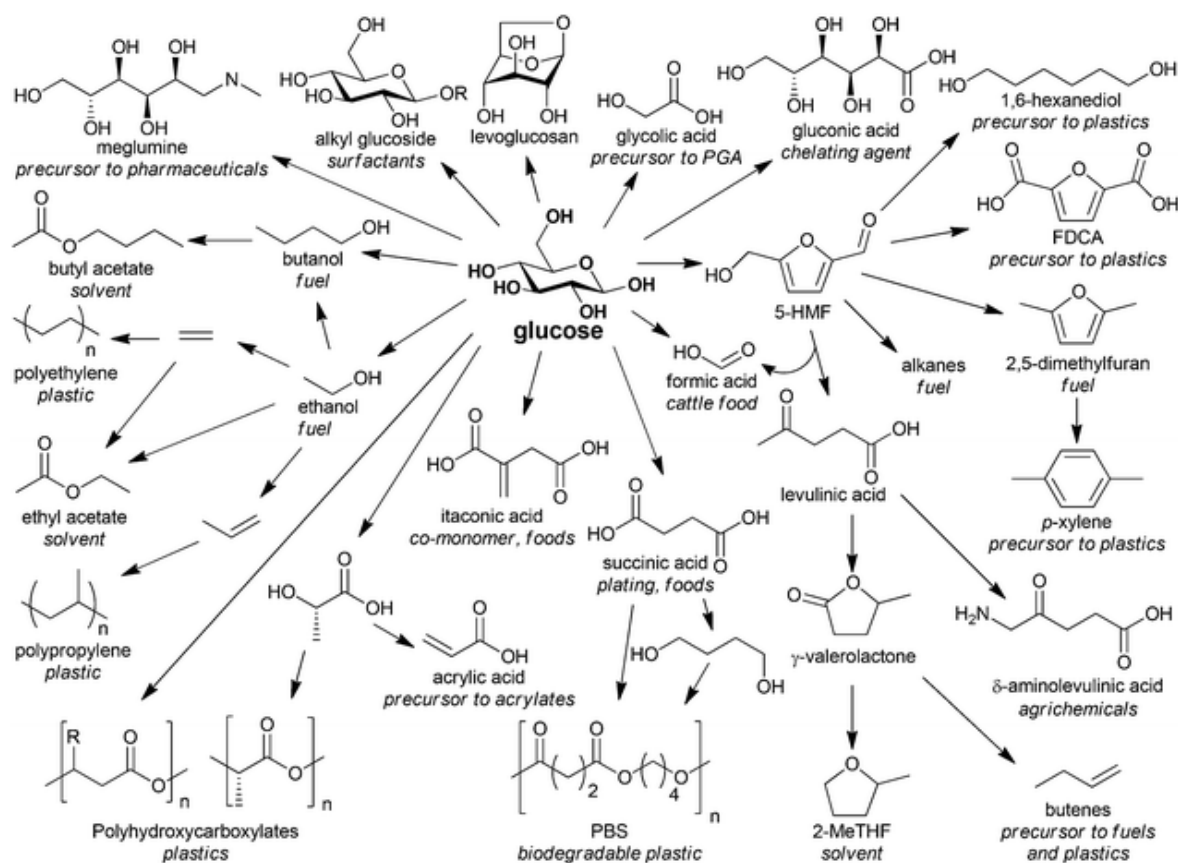
Figure 8 – Derivatives of glucose and their applications

Glucaric acid is an oxidized sugar with two carboxylic functional groups situated at the two ends of the carbon chain (figure 9). It figured in the report "Top Value Added Chemicals from Biomass" issued by the U.S. Department of Energy in 2004, where a number of molecules deriving mainly from renewables were listed together with their potential in a bio-based chemical industry[65].

Glucaric acid was included due to its possible use in the preparation of new nylons and hyperbranched polyesters, in addition to a number of lactones that can serve as solvents and glucaric acid direct use as a cation chelating agent in the detergent industry. The challenges posed in the report were to eliminate nitric acid in the production of glucaric acid (figure 10), which still represents to this date the most used method.
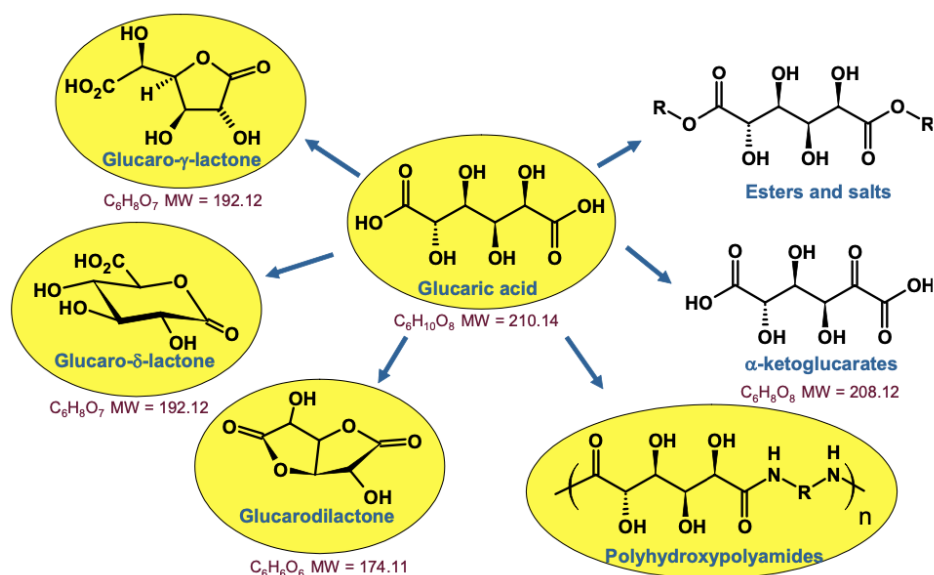
Figure 9 - Chemical structure of glucaric acid and its derivatives

The relative simplicity of this route, where nitric acid serves both at solvent and oxidising agent, coupled with a yield of 40-45%, make up for the significant amount of inorganic waste salts (excess nitric acid is neutralised by KOH addition) and toxic by-products (nitric acid partially decomposes to NO_x and N_2O) generated. However, owed to the major issues that nitic acid poses towards the sustainability and environmental impact of the process, alternative methods are seeked.

Figure 10 – nitric acid oxidation to glucaric acid

Alternative pathways to glucaric acid were developed: by metabolic engineering to create new fermentation routes[66], by the use of organic catalysts and chemical oxidants[67] or by electrocatalysis[68].

Modification of *Escherichia coli* with three genes from *Saccharomyces cerevisiae*, *Pseudomonas syringae* and mice led to obtaining glucaric acid in a concentration of 1g/L. Glucose to glucuronic acid, which is then converted to the target molecule when uronate dehydrogenase is included from the bacteria.

The use of 4-acetamido-TEMPO as a catalyst in combination to sodium or potassium bromide as co-catalyst and in presence of an oxidant, namely sodium or potassium hypochlorite, constitutes a second alternative approach. At pH values between 11,4 and 11,6 and low temperature (below 5˚C) this method allows a yield above 85% of glucaric acid salts (sodium or potassium) with good selectivity although some important drawbacks keep this process far from the desired sustainability goals. In

particular, the purification of glucarate salts to obtain glucaric acid generates large amounts of waste; the oxidant used represent another problem as they are expensive and contain chlorine atoms that end up in waste.

Electrocatalysis is a recent approach to glucose oxidation for the production of gluconic acid and glucaric acid. An excellent selectivity of 84% to glucaric acid and a selectivity of 15% to gluconic acids are obtained at glucose conversion of 99% in mild experimental conditions: 30°C, neutral pH and a current of 6 mA/cm^2. The anode is made up of MnO_2 nanoparticles supported on porous titanium oxide, while a stainless steel mesh constitutes the cathode. Despite the good results in terms of glucaric acid yield and absence of exotic oxidants and strong acid/bases, scaling this technology to the industrial level is very expensive and not competitive enough to enter the market yet.

Supported metal nanoparticle catalysts for glucose oxidation

Heterogeneous catalysis by supported gold nanoparticles is a route that has been applied to glucose oxidation to glucaric acid only recently. Au nanoparticle catalysts were first studied for glucose oxidation to gluconic acid as a substitute for Pt and Pd supported nanoparticles, which showed deactivation and leaching[69]. Oxidation of organic molecules by gold nanoparticles was already known, thanks to the work by Prati and Martra on alcohol oxidation by Au NPs supported on AC[17]. Further work by Prati and co-workers uncovered the possibility to oxidize glucose to gluconic acid[70]. It was found that a selectivity >99% to gluconic acid is achieved in basic conditions (pH = 7 to 9,5) at mild temperatures (50°C), without leaching of the active phase. It was later proved that basin environment is fundamental to favor glucose adsorption on the catalyst surface[71] in a study on Au nanoparticles supported on activated carbon. The pH value was increased from 7,0 to 9,5 at constant temperature (50°C) and it was observed that the initial reaction rate of gluconic acid formation increased from 1,00 mmol L^{-1}min^{-1} at pH 7,0 to 3,15 mmol L^{-1}min^{-1} at pH 9,5.

The mechanism of glucose oxidation to gluconic acid was investigated, clarifying the importance of the basic environment for this reaction. In detail, glucose forms an anionic species that binds to the Au nanoparticle, forming an electron-rich gold species. Molecular oxygen is activated by nucleophilic attack from the electron-rich glucose-Au nanoparticle complex[72]. On the dioxogold intermediate, a two-electron transfer occurs from the adsorbed glucose anion to the activated molecular oxygen, where the Au^+-O_2^- or Au^{2+}-O_2^{2-} couples can be considered as a bridge for the electrons. At the end of the reaction, the as-formed gluconate anion and hydrogen peroxide desorb from the gold nanoparticle, as can be seen from figure 11. To clarify the role of hydrogen peroxide in the reaction mixture, Saliger et al investigated glucose oxidation with Au nanoparticle catalyst and H_2O_2 as oxidizing agent in alkaline conditions[73].
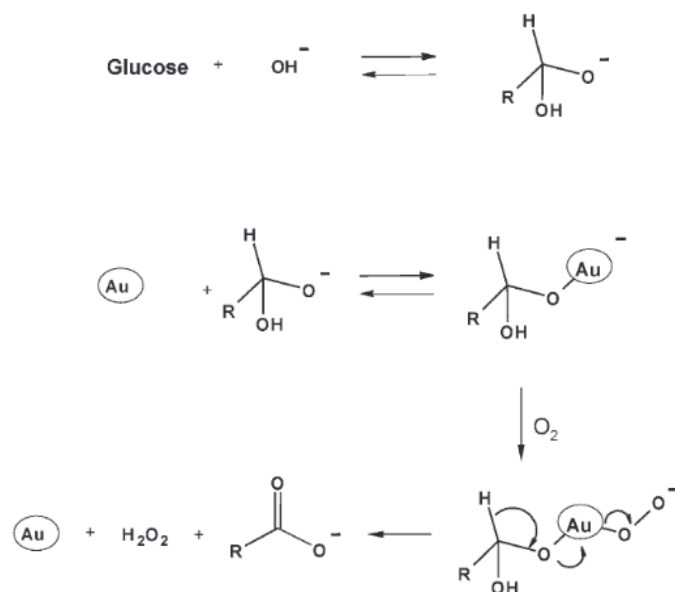
Figure 11 – Proposed mechanism of glucose oxidation to gluconic acid by Au nanoparticles in alkaline reaction medium.

In their findings, glucose oxidation by O_2 and by H_2O_2 have similar activation energies (48 kJ/mol for H_2O_2 and 47 kJ/mol for O_2) and comprise the same rate-determining step in the 30-60˚C temperature range. Hence it was assumed that the effective oxidizing agent is the O_2 formed by decomposition of hydrogen peroxide.

Glucose oxidation to glucaric acid catalyzed by gold nanoparticles

Gluconic acid, produced from glucose by oxidation, can be subsequently oxidized to glucaric acid. This reaction is slow and difficult, and only few studies were reported on this subject. Catalysts used for the aerobic oxidation of glucose are primarily made up of platinum or gold in their active phase. Commercial Pt/C was reported[74] to achieve an optimized glucaric acid yield of 74% at neutral pH, mild temperatures (80˚C) and O_2 pressure (13,2 bar), although to a low glucose:Pt molar ratio of 54:1. Pt and PtAu nanoparticles supported on various metal oxides (TiO_2, ZrO_2, SiO_2) were included in a patent from Rennovia for the oxidation of glucose to glucaric acid, with yields up to 70% after a reaction time of 5 hours, at neutral pH, moderate temperatures and O_2 pressure (90-112˚C, 27 bar O_2). Pt-Au alloy nanoparticles on ZrO_2 were also studied by Derrien et al[75]. In this case, a glucaric acid yield of 50% was achieved with nanoparticles' average crystallite size of 6 nm, in a base-free reaction environment and using air as oxidant. High pressure, just under 40 bar, was required together with a moderate reaction temperature (100˚C) and glucose:metal molar ratio of 80:1.

Au nanoparticles supported on activated carbon were object of study of Solmi and coworkers[76].They thoroughly studied reaction conditions, such as glucose concentration, base: glucose molar ratio, temperature, pressure, glucose:metal molar ratio. Monometallic Au and bimetallic AuBi

nanoaprticles were tested for the reaction and the bimetallic alloy was found to be the most active. Reaction conditions were optimized for AuBi/AC catalyst: a glucose:metal molar ratio of 500:1, much higher than for the Pt-based catalysts, allowed glucaric acid yield of 31% at 60˚C, 10 bar O_2 and glucose:NaOH molar ratio of 1:3. With full conversion of glucose, a yield of 18% gluconic acid and 40% byproducts was reported. After identification of the by-products, a full reaction scheme was proposed ac can be seen in figure 12.
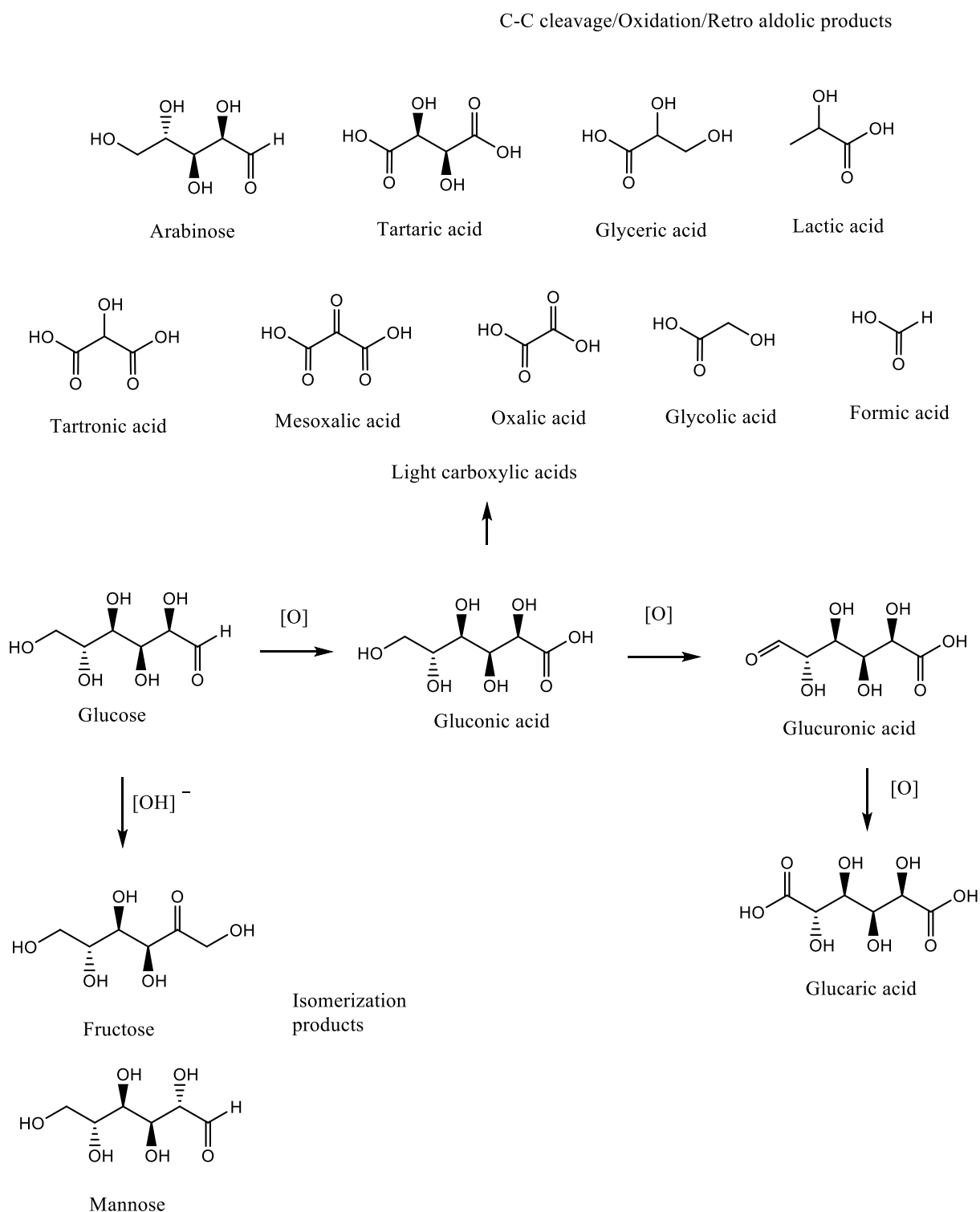

Figure 12 – Proposed reaction pathway from glucose to glucaric acid and by-products by Au supported nanoparticles.

2. Experimental section

This chapter is divided in four sections:

- Materials and procedures used in Bologna University at the Department of Industrial Chemistry "Toso Montanari";
- Materials and procedures used in Swansea University, College of Engineering;
- A description of the characterization techniques and the specifications that apply to each;
- A description of the analytical techniques and the procedures used for data analysis.

2.1. Nanostructured catalysts from sol immobilisation method

In this section, the methodology for the preparation of nanostructured catalysts by sol immobilisation is described, followed by the analytical techniques that were used to characterise the materials prepared. The analytical techniques are:

- UV-Vis spectroscopy;

-X-Ray diffraction (XRD)

-Transmission electron microscopy (TEM)

-Dynamic Light Scattering (DLS)

Regarding the catalytic testing, the methods and equipment used to carry out the test reactions are described, together with the analytical methods that were used to determine product concentration and the calibration procedures. In regard to nitrophenol reduction, this section contains the two reaction experimental setups that were studied for the experimental determination of catalytic activity of the materials. The analytical technique is UV-vis spectroscopy for the determination of nitrophenol concentration. Prior to the experiments, a calibration of the instrument was executed to determine the response factor of the substrate. Glucose oxidation was studied with a previously optimised methodology. The analytical determination of the reaction products was operated with HPLC. The response curves were also determined in a calibration process.

2.1.1. Reagents

A list of the reagents used for HPLC calibration, catalyst preparation, glucose oxidation and nitrophenol reduction are listed in table 2 with their molecular weights and purity.

Compound	Formula	Molecular weight (g/mol)	Purity
Glucose	$C_6H_{12}O_6$	180,16	>99%
Gluconic acid	$C_6H_{12}O_7$	196,16	97%
Glucaric acid	$C_6H_{10}O_8$	210,14	98%
Oxalic acid	$C_2H_2O_4$	90,03	>99%
Tartaric acid	$C_4H_6O_6$	150,09	>99%
Tartronic acid	$C_3H_4O_5$	120,06	>97%
Lactic acid	$C_3H_6O_3$	90,08	85%
Formic acid	CH_2O_2	46,02	>95%
Glyceric acid	$C_3H_6O_4$	106,08	>97%
Glycolic acid	$C_2H_4O_3$	76,05	99%
Arabinose	$C_5H_{10}O_5$	150,13	>98%
Fructose	$C_6H_{12}O_6$	180,16	≥99%
Mannose	$C_6H_{12}O_6$	180,16	99%
2-keto-D-gluconic acid (2KDG)	$C_6H_{10}O_7$	194	99%
5-keto-D-gluconic acid (5KDG)	$C_6H_{10}O_7$	194	98%
Mesoxalic acid	$C_3H_2O_5$	118	98%
Tetrachloroauric acid trihydrate	$HAuCl_4*3H_2O$	393,83	>99%
Polyvinylpyrrolidone	$(C_6H_9NO)_n$	29.000	Information not provided
Polyethilene glycol	$C_{2n}H_{4n+2}O_{n+1}$	8.000	Information not provided
Polyvinyl alcohol	$(C_2H_4O)_n$	13.000-23.000	87-89% hydrolyzed
Sodium borohydride	$NaBH_4$	37,83	≥98%
Sodium hydroxide	$NaOH$	39,99	>98%
4-nitrophenol	$C_6H_5NO_3$	139,11	≥ 99%
Activated carbon NORIT SX1G	Carbon	/	Information not provided
High Area TiO₂	TiO_2	79,87	Information not provided

Table 2 – Reagents used for catalyst preparation, oxidation reaction of glucose, calibration curves for HPLC and nitrophenol reduction.

2.1.2. Preparation methods

A colloidal Au solution was prepared by dissolving 20,9 mg of solid $HAuCl_4 \cdot 3H_2O$ in 390 mL of distilled water, to which is added a volume of 1% w/w polymer aqueous solution to obtain the desired Au:polymer weight ratio. After 3 min, a freshly prepared aqueous solution of $NaBH_4$ (0,1 M, Au:NaBH₄ = 1:5 mol/mol) was added to the solution under vigorous magnetic stirring. A ruby red Au(0) sol was immediately formed and it was confirmed by the UV/vis spectrum of the Au colloidal solution. After 30 minutes, the Au colloids (acidified at pH 2 by using sulfuric acid) were immobilized by adding the support under vigorous stirring. The amount of support was calculated in order to obtain a metal loading of 1% (on the basis of quantitative loading of the metal onto the support). The

catalysts were filtered on a Buchner funnel with two filter papers and washed several times with distilled water to remove ionic species, such as Na$^+$, Cl$^-$, and mother liquors until a neutral pH was reached. If the paper filter mesh was not small enough to allow filtration, the catalysts were centrifuged for 15 minutes at 4500 rpm, washed with aliquots of 25 ml and centrifuged again with the same settings until the washing filtered solution was neutral. After drying overnight at room temperature, the solids were dried at 80 °C in an oven for 4 h in static air conditions.
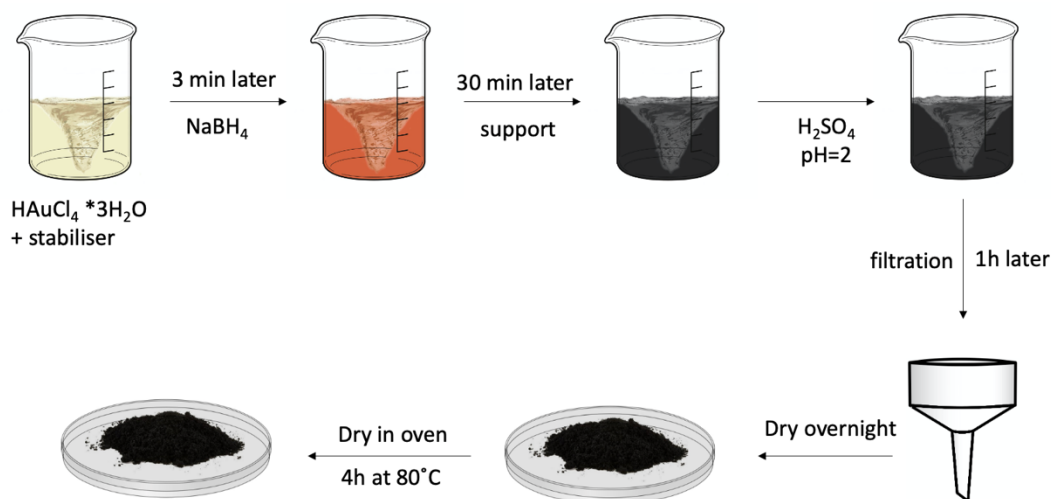
Figure 13 – Scheme for preparation of preformed Au nanoparticles supported on AC or TiO$_2$.

2.1.3. Nitrophenol reduction reaction

Reaction solution

Aa aqueous 4-nitrophenol concentrated solution (0,01M) was prepared using the following experimental protocol: 0,1391 g of 4-nitrophenol dissolved in deionised water in a 100 mL volumetric flask in 24 hours. This solution was used to prepare the fresh 4-NP reactions solutions: 500 µL of the initial 4-NP concentrated aqueous solution was withdrawn with a micropipette and diluted to a concentration of $2,0 \times 10^{-4}$M in a 25mL volumetric flask. The desired amount of catalyst (varying depending on the experimental protocol) was weighted on an analytical scale. For the preparation of a fresh aqueous solution of NaBH4, a25 mL volumetric flask was used, 8,5 mg of NaBH$_4$ were dissolved in deionised water to obtain a solution $9,0 \times 10^{-3}$M, in a 4-NP:NaBH$_4$ molar ratio of 1:45. A reference solution for the UV-Vis measurements was prepared by dissolving 4,3mg of NaBH4 in a 25 mL volumetric flask.

The two solutions and the catalyst were mixed in different orders depending on the experimental setup adopted as described below.

1st setup: Round-bottom flask setup

The nitrophenol reduction reaction was performed in a 250 mL round-bottom flask equipped with a magnetic stirrer set at 900 rpm, at room temperature (20°C). The optical absorbance of the reaction was recorded by the UV-Vis spectrometer as a function of reaction time to monitor the disappearance of 4-NP concentration. The measurements were made withdrawing 3,5 mL of the reaction solution, filtered with a PTFE 0,22 μm syringe filter to remove the catalyst into a quartz cuvette with an optical path of 1 cm. When recording the UV-vis spectra, the reference sample was used as prepared in a second quartz cuvette, using the double beam mode.

The 4-NP $2,0x10^{-4}$M solution and the $NaBH_4$ $9,0x10^{-3}$M solution were mixed in the round bottom flask adding the solutions in the following order: firstly, the nitrophenol solution, to which the reducing agent is added only when ready to start the reaction. Once mixed with sodium borohydride, 4-NP has a bright yellow coloration. The catalyst was added last, starting a timer to keep track of the reaction time with the addition of catalyst.
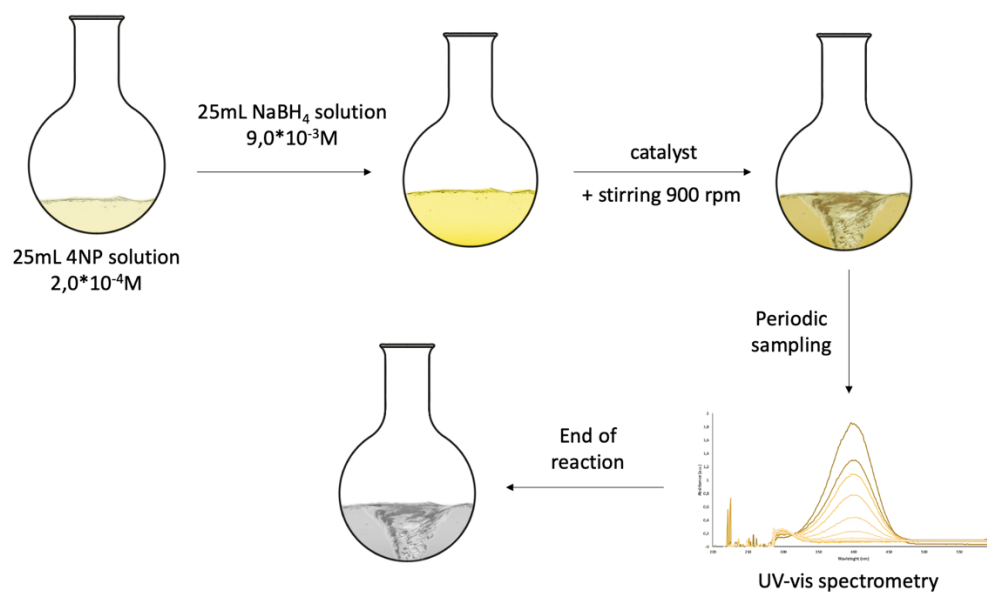
Figure 14 – Scheme of round-bottom flask reaction setup

2nd setup: Cuvette setup

For this experimental setup, a glass beaker of 50 mL capacity was used to mix the reactants. The following experimental protocol was used: the catalyst was added firstly inside the beaker, then 25 ml of $2,0x10^{-4}$ 4-NP solution was carefully added to avoid catalyst particles to get floating on the surface of the liquid, which would imply that part of the material is not in homogeneous contact with the reactants. Immediately after 25 mL of fresh $NaBH_4$ solution ($9,0x10^{-3}$ M) were added, and this was the time it was considered as the initiation of the reaction. After gently mixing by hand, a 3,5 mL aliquot was drawn from the beaker and poured in a glass cuvette, subsequently inserted in the UV-

vis spectrometer's stage. After exactly 2 minutes and 30 seconds the measurement method was started. The optical absorbance of the reaction was set to be automatically measured every 2,5 minutes for 25 cycles by the Perkin Elmer UV-VIS-NIR Lambda 19 to measure 4-nitrophenol concentration disappearance as a function of reaction time. The instrument was used in double beam mode. For every measurement, the reference sample was used as prepared in the second cuvette.
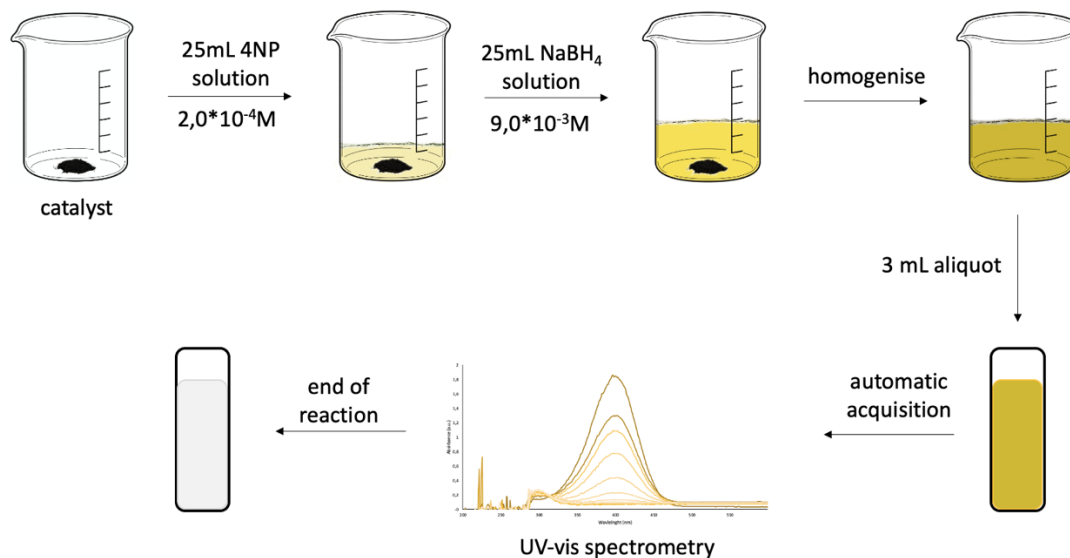
Figure 15 – Scheme of cuvette reaction setup.

2.1.4. Reusability test for nitrophenol reduction

Reusability tests were carried out using the "cuvette setup" procedure. The total amount of the end-reaction mixture was collected in Falcon centrifuge tubes. The mixture was centrifuged at 4500 rpm for 15 minutes in order to separate the catalyst from the end-reaction solution. The supernatant was collected and set aside, while the catalyst was recovered with 25 mL of a fresh 4-nitrophenol solution $2,0x10^{-4}$M. The catalyst-containing 4-nitrophenol solution was poured in a beaker, to which is subsequently added 25 mL of a NaBH$_4$ solution $9,0x10^{-3}$M to repeat the nitrophenol reduction reaction, which was carried out following the "cuvette setup" procedure. After the first reaction with fresh catalyst, the reaction was repeated 5 times.

2.1.5. Glucose oxidation reaction

Reaction solution

The reaction solution is prepared by adding 0,5259 g of NaOH in 15 mL of deionised water, to which 0,7895 g of glucose are subsequently added. The as-obtained solution is 5% wt in glucose (29M) and NaOH is in a molar proportion of 3:1 with respect to glucose. 0,0863 g of 1%wt Au catalyst were added, to have an Au:glucose molar ratio of 1:1000. The reagents and catalyst were added in the reactor's vessel together with a magnetic agitator. The reactor was tightly closed and pressurised with

10 bar of gaseous oxygen, after being purged firstly with O_2 three times. The reaction was carried out at a temperature of 60°C by placing the reactor in a heating mantle and controlled by a thermocouple, under stirring at 1000 rpm to guarantee diffusion and homogeneity of the reagents. The reaction time was started as the temperature reached the set-point temperature of 60°C. To quench the reaction, the reactor was placed in an ice bath for 10 minutes.

Sample treatment and analysis

The end-reaction mixture was collected and centrifuged at 4500 rpm for 15 minutes to separate the liquid from the catalyst. The final volume was measured, and a sample was taken for subsequent analysis by HPLC and storage. The catalyst was left dry overnight at ambient conditions.

Reactor

The reactor used to carry out the glucose oxidation reaction is a stainless-steel autoclave batch reactor with a capacity of 50 ml. On the top cover, the load line and discharge line are both controlled by an interception valve; a pressure gauge and a hollow steel capillary for the introduction of the thermocouple (not in direct contact with the solution inside the reactor) allow for pressure indication and temperature control respectively.
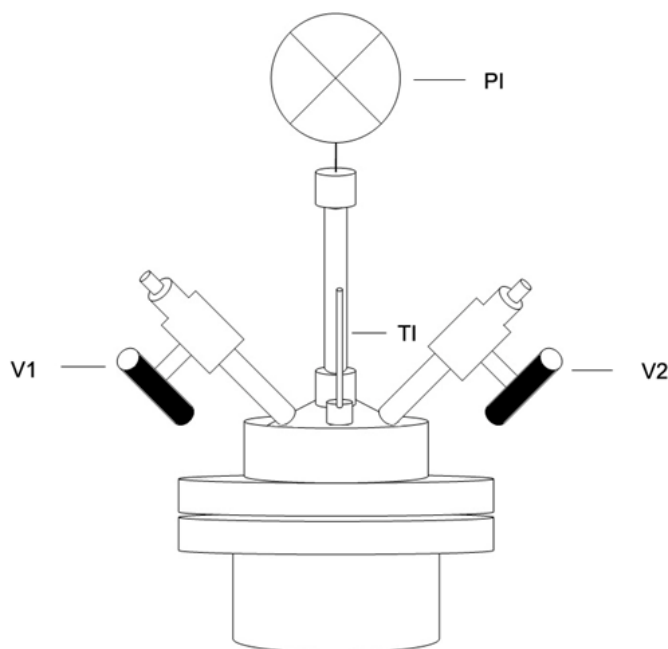

Figure 16 – Schematic diagram of the batch reactor used in the oxidation of glucose

Where PI: Pressure gauge WIKA 315SS (0-25 bar); V1: Valve for the load line; V2: Valve of discharge line; TI: Capillar tube for insertion of thermocouple.

2.1.6. Stability of Au colloidal solutions

A colloidal Au solution was prepared by dissolving 20,9 mg of solid $HAuCl_4 \cdot 3H_2O$ in 390 mL of distilled water, to which 644μL of 1% w/w polymer aqueous solution to obtain an Au:polymer weight ratio of 0,65. The polymers investigated were PVA, PVP and PEG. After 3 min, a freshly prepared aqueous solution of $NaBH_4$ (0,1 M, Au:$NaBH_4$ = 1:5 mol/mol) was added to the solution under vigorous magnetic stirring. The stability of a colloidal solution was investigated by DLS analysis, executed at defined time periods from the addition of $NaBH_4$.

2.2. Nanostructured catalysts from cluster beam deposition

This section comprises the preparation methods for the gas-phase synthesis of nanostructured catalysts, the analytical techniques used to characterize the materials and to determine the reaction kinetics, and the methods that were followed to execute the nitrophenol reduction and ozonation reactions.

To characterize the materials, the following techniques were used:

- X-ray photoelectron spectroscopy (XPS)

- Transmission electron microscopy (TEM)

- ICP-AES

- BET

Nitrophenol concentration was determined using the same technique for both reactions, which is UV-Vis spectrometry.

2.2.1. Reagents

The reagents used for catalyst preparation, nitrophenol ozonation and nitrophenol reduction are listed in table 3 with their molecular weight and purity.

Compound	Formula	Molecular weight (g/mol)	Purity
Sodium borohydride	$NaBH_4$	37,83	98%
4-nitrophenol	$C_6H_5NO_3$	139,11	≥ 99%
TiO_2 P25	TiO2	79,87	Information not provided
Bulk gold	Au	196,97	99,99%
Bulk silver	Ag	107,87	99,99%

Table 3 – Reagents for catalyst preparation, nitrophenol reduction and nitrophenol ozonation

2.2.2. Preparation methods

The materials studied in Swansea University were prepared with the MACS cluster beam deposition technique. The process was introduced in the previous paragraph 1.2.2. and further detailed information can be found in literature[25,77].

The matrix was prepared on an oxygen-free Cu support mounted on a cold finger cooled at about 20 K by a close-loop helium cryocooler (Sumitomo Heavy Industries, RDK-500E). Metal atoms were vaporised from a thermal effusion cell (Createc: HTC) while introducing Ar gas in the chamber. A deposition cup made out of stainless steel, containing support in powder form (2 g, TiO_2, P25 from Sigma-Aldrich), was moved in a position close to the matrix to collect the clusters. After that, the Ar+ ion beam source (Kaufman & Robinson, KDC 40) sputtered the matrix to initiate the nucleation and growth cascading process through ion-matrix impacts. The nanoclusters sputtered out of the matrix were eventually harvested onto the support, which was mixed with a metallic comb throughout the deposition to maximise the exposition to the cluster beam.
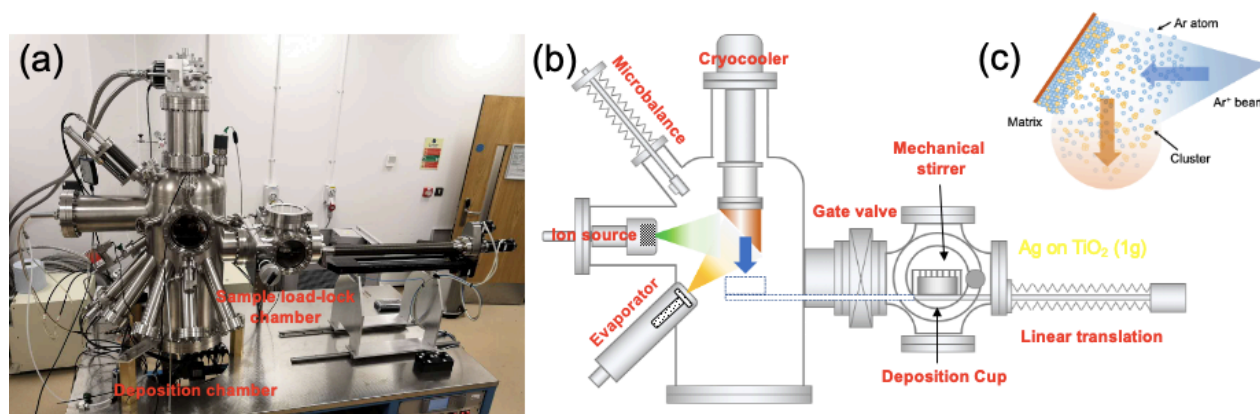
Figure 17 – a) picture and b) schematic diagram of MACS system; c) schematic representation of cluster formation by ion sputtering of the Ar matrix containing Au atoms.

2.2.3. Nitrophenol reduction

The nitrophenol reduction was performed in aqueous solution at room temperature with $NaBH_4$ acting as the reductant. 4-Nitrophenol (1,67 mg, Sigma-Aldrich) and $NaBH_4$ (18,92 mg, Sigma-Aldrich) were added in deionized water (200 mL) sequentially, which results in a 4-nitrophenol concentration of $1,0 \times 10^{-4}$ M and $NaBH_4$ concentration of $2,5 \times 10^{-3}$ M. After shaking the solution for 2 min, the colour became yellow, which indicated 4-nitrophenol conversion to 4-nitrophenolate. For each test, 30 mg catalyst were added to 50 mL of this solution and continuously magnetically stirred (500 rpm). The optical absorbance of the reaction solution was recorded by a UV–VIS spectrophotometer at intervals of 5 min to monitor the kinetics of the reaction as a function of time and disappearance of 4-NP concentration. For each measurement, 4 mL of the analyte solution was filtered by a syringe filter to remove the catalyst before the analysis was made.

TiO$_2$ powder itself and filter were tested and confirmed to be catalytically inert for the nitrophenol reduction reaction.

2.2.4. Nitrophenol ozonation

Ozonation was carried out at room temperature (20˚C) in a semi-batch glass reactor containing 200 mL of 4-nitrophenol aqueous solution (0,1µM) and 50 mg of catalyst under magnetic stirring at 500 rpm. O$_3$ was generated from an ozone generator (BMT 803, BMT Messtechnik, Germany) fed by oxygen or dry air and the gas concentration was measured by an ozone analyser (BMT 963, BMT Messtechnik, Germany). The gaseous feed was bubbled in the reactor at a flow rate of 500 mL/min. Ozone concentration was adjusted in a range from 3 g/m^3 NPT to 10 g/m^3 NPT (NTP: normal gas temperature and pressure; 0˚C and 1 atm) by varying the power of the ozone generator. The catalytic reaction was initiated by introducing ozone into the reactor using a sintered glass diffuser.

A pH meter (Orion Star A211 series) was used to monitor pH over the course of the reaction, to allow pH control with diluted NaOH and HCl. Sample solutions of approximately 3 mL were periodically withdrawn from the reactor, followed by air bubbling to quench the ozone reaction and filtration with a 0,22µm nylon syringe filter before being transferred into a quartz cuvette. The pH of the sample was adjusted, when needed, prior to UV-vis spectrum recording. The filter was tested and confirmed to possess inertness for reaction catalysis and nitrophenol adsorption.

2.2.5. Adsorption test

Adsorption tests were made using 10 ml test tubes containing an aqueous solution of 4-nitrophenol 0,1µM and the material to test in a different concentration in each test tube. The samples were kept in the dark while continuously stirring at 25˚C. The adsorption was measured comparing the absorbance at a wavelength of 400 nm of the mother solution and of the solution of each test tube after 20 hours. The pH was adjusted with a few drops of NaOH 0,1M before recording the UV-vis spectrum.

2.2.6. PZC

Point of zero charge was measured using a method that exploits the difference in pH induced by the solid from the initial solution pH, in a solution of controlled ionic strength.

Five vials were prepared with a volume of 25mL of a freshly prepared NaCl 0,1M in each one. Diluted solutions of HCl (0,1M) and NaOH (0,1M) were used to adjust pH at a desired value, checking the pH value with a digital pH meter (Orion Star A211 series) under magnetic stirring. Each vial had a different pH, covering a range from 2 to 10. When the pH was stabilised, 0,01 g of solid were added

to each vial. The vials were left stirring in the dark at 25°C for 24h. The pH of each vial was then measured again to record the difference with the initial pH.

2.2.7. Reusability test

The recovery process consisted in centrifuging the reaction mixture at $4,4*10^3$ rpm for 10 minutes, then washing the catalyst with 30 ml and of deionised water centrifuging again to remove any adsorbed species from the previous reaction. A volume of 200 ml of 4-nitrophenol 0,01µM solution was prepared, and a small volume of it was used to recover the catalyst from the centrifuge vial, reuniting the catalyst-containing solution to the rest directly inside the reactor. The ozonation reaction proceeded as described earlier.

2.3. Characterisation techniques

2.3.1. UV-vis spectroscopy

UV-vis spectroscopy is a routine technique used in analytical chemistry for the identification and quantification of transition metals, highly conjugated organic molecules and biological macromolecules in solution or in solid samples. It can be either intended for absorption and reflectance spectroscopy of the full visible spectral region and part of the adjacent ultraviolet. The interaction between the molecules or atoms is given by electronic transitions that occur in this range of the electromagnetic spectrum. Another phenomenon that makes it possible to exploit UV-vis spectroscopy is surface plasmon resonance (SPR). SPR is described as the resonant oscillation of conduction electrons stimulated by incident radiation. In nanoparticles, there is a direct relationship between size and resonance wavelength, the latter falling in the visible spectrum for Au and Ag. This relationship is particularly convenient for an early characterisation of colloidal nanoparticles without the use of costly instrumentation.

Aqueous solutions are typically analysed in absorption mode. The instrument measures the intensity of light passing through the sample (I) and compares it to the intensity of light before passing through the sample (I0). Transmittance is the ration of these two intensities. Absorbance is related to transmittance by a logarithmic equation:

$$A = -\log (T/100)$$

Where A=absorbance and T=transmittance.

Generally, a spectrophotometer is composed of the following basic parts: a light source, a monochromator, a holder for the samples and a detector. Common radiation sources are a Tungsten filament for the visible range (350 - 2500 nm) and a deuterium lamp, which is continuous over the

ultraviolet range (190 - 400 nm). A monochromator is the needed to separate the different wavelengths of light. Either a prism or a diffracting grate can be used for such a task as they both rely on the principle that the optical interaction (diffraction or refraction) depends on the wavelength, resulting in the separation of a beam of multi chromatic light into its components. The radiation can reach the sample in two different set up: single beam or double beam. In a double beam instrument, the light is split into two beams. One beam is used as the reference and the other passes through the sample. The reference beam intensity is taken as 0 absorbance and the ratio of the two beam intensities is displayed.

The spectrometer used at the Department of Industrial Chemistry "Toso Montanari" to observe the plasmon resonance peak related to the metallic gold nanoparticles was a Perkin Elmer UV-VIS-NIR Lambda 19 recording the optical absorbance from 750 nm to 190 nm wavelength.

2.3.2. Dynamic Light Scattering (DLS)

Dynamic light scattering (DLS) is an analytical technique that allows the determination of the size distribution profile of small particles in solution. The instrument measures the temporal fluctuation of scattered intensity trace, which is analysed by an autocorrelator that obtains eventually the nanoparticle size distribution.

Scattering is a type of interaction among light and matter that causes the deviation of the linear trajectory of a photon. The samples analysed is made out of small particles in a solution able to move around by Brownian motion or random walk. The particles move with a speed that is directly related to their size: particles that have a faster motion will have smaller dimensions. The intensity trace of the scattered light has a fluctuation frequency dependent on the speed of particles motion, hence on nanoparticles size.

Ina DLS instrument, a laser light beam passes through a polarizer and hits the sample. The photons are scattered in all directions and is detected by a photomultiplier (a device that converts incident photons into electric signal) placed at a specific angle in respect to the laser beam. The signal is analysed by an autocorrelator that extracts information from the time-correlated data such as nanoparticles size and size distribution.

The DLS analysis at the Department of Industrial Chemistry "Toso Montanari" were carried out using a Malvern Zetasizer Nano ZS.

2.3.3. X-Ray Diffraction (XRD)

X-ray diffraction (XRD) is a largely used technique that allows to obtain information regarding the unit cell structure, crystallite size and chemical identity of a crystalline solid. This analytical method relies on the interference (constructive and destructive) of diffracted X-rays from crystallographic planes. The model generally adopted to interpret the phenomenon is the one that led Bragg to formulate his well-known law. A crystallographic plane can be seen as a semi-transparent mirror, meaning that part of the incident light will be reflected and part will pass through to the next plane. Here reflection is to be intended as backscattering of X-rays by the atoms belonging to the crystallographic plane of a photon with the same wavelength that the one absorbed but at a specular angle (hence the mirror analogy).

X-rays scattered from adjacent planes interfere constructively when a geometrical condition in fulfilled, which is contained in Bragg's law:

$$2d \sin\theta = n\lambda$$

Where d = distance between planes, θ = angle between the plane and the X-ray, λ = wavelength of the X-ray, n > 0.

The result is a diffractogram where the resulting diffraction peak intensity is plotted against the θ angle, which is generally expressed as 2θ for instrumental reasons. While θ is useful to identify the unit cell dimensions, peak intensities can be treated by a Fourier transform method to identify the arrangement of atoms in the unit cell. The diffractogram can provide further structural information on the material: the width of the diffraction peaks is related to the size strain. If the peaks are wide, the crystallite size is small in comparison to a crystallite estimated from a narrow peak. Thanks to Scherrer equation it is possible to link the full width at half maximum to the crystallite size:

$$FWHM(2\theta) = K \lambda / (L \cos\theta)$$

Where FWHM = Full Width Half Maximum, λ = wavelength, L = crystallite size, K = Scherrer constant.

This means that peak width (FWHM) varies inversely with crystallite size. As the crystallite size gets smaller, the peak gets broader. The constant of proportionality, K (Scherrer constant) depends on how the width is determined, the shape of the crystal, and the size distribution. By extension, nanoparticles can be seen as isolated crystallites. Through this analytical technique it was possible to estimate the average dimensions of the gold NPs deposited on the support.

XRD analysis were performed with a Bragg-Brentano X'pertPro Panalytical diffractometer using a copper anode (K$_\alpha$ radiation at $\lambda = 1.5418$ Å) as source of X-radiation with 0.08° step size and acquisition time of 1300 s per step in 36 - 41° 2θ range. The average gold crystallite size of Au/AC catalysts was calculated from the broadening of the (111) Au plane at 38.2° applying Scherrer's equation.

2.3.4. Transmission Electron Microscopy (TEM)

Transmission electron microscopy (TEM) is a microscopy technique in which a beam of electron si transmitted through a specimen to form an image. It is used to obtain a significantly higher resolution compared to optical microscopy, owing to the smaller de Broglie wavelength of electrons. Transmission electron microscopes enables to capture details that are not detectable in visible light such as single columns of atoms. The specimens are usually either in the form of an ultra-thin section (less than 100 nm thick) or a suspension deposited on a grid. Standard TEM grid sizes are 3.05 mm diameter, with a thickness and mesh size ranging from a few to 100 μm. A TEM's fundamental parts are an electron gun, a detector, a vacuum system, the specimen stage, a series of electromagnetic lenses, and electrostatic plates. The latter two allow physical manipulation of the electron beam, which confer a great flexibility of operation to this analytical instrument. The TEM images (hystograms) will serve for the calculation of average particle diameter (size), standard deviation and particle size distribution by frequency (%). For every distribution over 300 particles where used from the total number of measured particles (>400 particles) per sample.

TEM analysis at the Department of Industrial Chemistry "Toso Montanari" were performed with TEM/STEM FEI TECNAI F20 microscope at 200 keV. Samples were suspended in ethanol and treated by ultrasound for 15 min. A drop of the suspension was deposited on "quantifoil-carbon film" supported by a grid of Cu. The preparation was dried at 120°C.

The morphology imaging of both the Au and Ag cluster catalysts was performed in Swansea University by a Thermo Fisher Talos Scanning/Transmission Electron Microscope (STEM) equipped with a high-angle annual dark-field (HAADF) detector operating with inner angle of 55 mrad at 200 kV. The incident electron beam convergence angle was 21 mrad. The STEM samples were prepared by dispersing the catalyst powders decorated with Au or Ag clusters in deionized water, sonicating for several minutes and drop-casting onto a copper grid coated with an amorphous carbon film.

2.3.5. X-ray photoelectron spectroscopy (XPS)

X-ray photoemission spectroscopy is a non-destructive analysis that allows the characterization of a material by quantitative analysis of surface elemental composition and chemical state. XPS is based

on the photoelectric effect: the sample surface is irradiated with X-rays and emits electrons. The detector measures the kinetic energy and the number of electrons emitted, for this reason the instrument works in high vacuum (HV, 10^{-8} millibar) or ultra-high vacuum (UHV, 10^{-9} millibar). As the incident X-ray energy is known (coming from the source) and the kinetic energy is measured, it is possible to obtain the binding energy of the emitted electron:

$$E_{binding} = E_{XRay} - (E_K + \Phi)$$

Where $E_{binding}$ is an electron's binding energy, E_{XRay} is the energy of the X-ray photons, E_K is an electron's detected kinetic energy, Φ is the work function depending on the spectrometer and on the material.

Elemental quantitative identification is possible because each element produces a distinctive set of XPS peaks at defined binding energy values, owed to an element's typical electronic configuration. The number of electrons at a given characteristic peak is related to the amount of the corresponding element within the surface of the sample. Hence an XPS spectrum is a plot of the number of detected electrons versus the binding energy (expressed in eV) of such electrons.

Chemical state is determined by the local bonding environment of a species: first of all its formal oxidation state, but also its interaction with the nearest neighbor atom. The result is a reproducible shift in the actual binding energy of the characteristic peaks, equivalent to NMR's chemical shifts, which provides the chemical state information.

The surface chemistry of the samples was studied by X-ray photoelectron spectroscopy (XPS) after air exposure. The XPS experiments were performed at room temperature and at a base pressure of 1.2×10^{-9} mbar using a Kratos Axis Supra equipped with a monochromatized Al Kα X-ray source (1486.6 eV) operated at 15 mA. The photoelectron core-level spectra were acquired using a hemispherical analyzer at a pass-energy of 160 eV for the wide scan, while the high-resolution spectra at a passing energy of 40 eV. All the spectra were aligned to the C-C carbon peak at 284.8 eV. The deconvolution of the spectra was done by CasaXPS software.

2.3.6. ICP-AES

Inductively coupled plasma atomic emission spectroscopy is an analytical technique used for element detection and quantification. It is a destructive technique where the atoms in the sample are excited by means of inductively coupled plasma. The excited atoms produce a characteristic spectrum that is used to identify the element; the intensity of the spectrum gives information on the quantity. Atomic emission spectroscopy is based on the photons emitted by excited atoms, when the electrons pushed

to higher energy orbitals (e.g. by heating) transition to lower energy levels releasing a photon. The frequency of the photons is a function of energy of the transition. The available transitions for each element are characteristic as they depend on their electronic structure.

During a typical analysis, a solution containing the analytes is pumped and nebulized directly in the plasma flame. The plasma flame is made of argon atoms ionised by interaction with an intense electromagnetic field generated by a radio frequency generating coil. The inelastic collisions between the Ar^+ ions and the neutral Ar atoms generates a temperature of 7000K and constitutes the plasma flame. The interaction of the analytes with the plasma flame brings the atoms to an excited state that gives the phenomenon of atomic emission upon transition to lower energy states, as described earlier. The resulting beam of light is separated into its components by an optical spectroscope and sent to detectors that measure the intensity received. The quantitative interpretation of the intensities is possible by measuring the intensities of known concentration samples to build a calibration line. The concentration of the analyte is obtained by interpolation on the calibration lines.

The metal loading of the cluster catalysts was characterized by ICP-AES following digestion in a mixed solution of hydrofluoric acid and nitric acid. The instrument was an Agilent 5110 ICP_OES.

2.3.7. BET surface area measurements

The Brunauer-Emmet-Teller (BET) measurement is often used for the determination of the surface area, pore volume and pore size of materials. It is based on the Brunauer-Emmet-Teller theory on physical adsorption of gas molecules on the surface of a solid. It applies to multilayer adsorption of an inert gas, which do not chemically react with the surface, at its condensation temperature. Molecular nitrogen (N_2) is commonly used for surface area measurements at a constant temperature of 77K. The resulting curves are called "adsorption isotherms" and are obtained by measuring the volume of adsorbed N_2 at a given N_2 pressure, which is increased gradually from vacuum to atmospheric pressure. The desorption isotherm is obtained by decreasing the pressure back to vacuum.The total surface area is expressed as:

$$S_{tot} = (V_{ads} / V_{N2, STP}) * N_A * \sigma_{N2}$$

Where S_{tot} is the total surface area, V_{ads} is the volume of the adsorbed N_2 forming a monolayer, $V_{N2, STP}$ is nitrogen molar volume in standard temperature and pressure conditions (22414 mL/mol), N_A is Avogdro's number ($6,023 *10^{32}$ molecules/mol), and σ_{N2} represents the cross section area of the

adsorbing molecule. The adsorbed volume is then normalised by the mass of the sample to obtain the specific surface area.

The Brunauer-Emmett-Teller (BET) surface area and pore radius were measured at 77 K using N_2 adsorption/desorption isotherms (Nova200e, Quantachrome Instruments, USA). Samples were degassed at 125°C for 12 h before nitrogen adsorption measurements. QuantachromeTM NovaWin package was used for data acquisition and analysis.

2.4. Analytics
2.4.1. UV-Vis spectroscopy
The instrument was described in a previous paragraph. UV-vis spectroscopy is a facile characterisation technique for metal nanoparticles but can also be used to perform quantitative determination of the concentration of highly conjugated organic molecules, given its molar extinction coefficient. Lambert-Beer law states that the absorbance of a solution is directly proportional to the concentration of the chemical species in solution and the length of the optical path:

$$A = \varepsilon * l * C$$

Where A is the absorbance, ε is the molar extinction coefficient (expressed in $M^{-1}cm^{-1}$), l is the optical path length and depends on the cuvette (normally 1 cm), and C is the concentration of the species in the solution. The molar extinction coefficient can be obtained by calibration. 4-nitrophenol in basic environment and in solution with $NaBH_4$ has a UV-vis peak at $\lambda_{max} = 400$ nm as the molecule deprotonates in the for of nitrophenolate.

The instrument available at Department of Industrial Chemistry "Toso Montanari" was a Perkin Elmer UV-VIS-NIR Lambda 19 used for nitrophenol concentration measurements using a wavelength range going from 600 to 200 nm.
The instrument used at Swansea University, College of Engineering, was an Agilent Technologies Cary Series UV-vis spectrometer recording the optical absorbance in a wavelength range from 200 nm to 600 nm.

Calibration of UV-Vis spectrometer
Molar extinction coefficient of 4-nitrophenol was obtained by calibration. Five solutions at different 4-NP concentrations ($1,5*10^{-4}$M, $1,0*10^{-4}$M, $5,0*10^{-5}$M, $2,5*10^{-5}$M, $1,0*10^{-5}$M) and $4,5*10^{-3}$M in $NaBH_4$ were prepared and analysed. The absorbance at 400nm of each solution was plotted against

concentration, the slope of the line was taken as molar extinction coefficient. The calibration was repeated three times and the average ε was obtained.

2.4.2. HPLC method

HPLC or high-performance liquid chromatography is a form of column chromatography based on a mobile phase (also called eluent), constituted of solvent in which a sample mixture or analyte are transported, a stationary phase contained in the column that interacts with the molecules in the solvent, and one or more detectors. Through HPLC it is possible to separate, identify and quantify organic compounds down to trace concentrations such as parts per trillion, making it an extremely versatile and useful analytical technique. The separation is made possible thanks to the different interaction of the various compounds with the two phases, which results in more or less retention. Retention time is the principal identification factor, as such a calibration of the retention factor or a standard are normally required especially if quantitative analysis is aimed.

During a typical analysis, a small volume of sample mixture is injected in the stream of the mobile phase and pumped through the stationary phase, where the various components of the mixture separate. The separation is caused by the amount of retardation or retention caused by the interaction of the substance with the stationary phase. Common eluents include any miscible combination of water and organic solvents or acids/bases. The retention time is measured when an analyte is detected. The detectors are placed after the column section. UV spectroscopy is a common type of detector (e.g. DAD, diode array detector) as many organic molecules absorb light in the UV range, i.e. alkenes, aromatics, and compounds having multiple bonds with heteroatoms such as O, N or S. The advantage is the linear correlation between the absorbance and the concentration of the compound passing through the detector. For those compounds that do not absorb light in the UV range, sugars for example, other detectors need to be employed. One example is the refractive index detector (RID), which is based on the difference of refractive index between the column downstream eluent and a reference stream of pure eluent. RID is more versatile than UV detector as virtually any compound could be detected, as long as it induces a difference in refractive index in the mobile phase.

The reaction mixture quantitative analyses were carried out using an Agilent 1260 Infinity Quaternary HPLC system. Analyses were performed using 0,0025 M sulfuric acid in ultra-pure water as eluent with a flow of 0,5 ml/min. The injection system consisted of a six-way valve with an injection volume of 20 μl. Two Rezex ROA-H+ (8%) 300x7,8 mm ion exclusion columns connected in serie were used for the separation of products. A diode array detector (DAD) set to 202 nm was used to detect organic

acids and a refractive index detector (RID) was used to detect monosaccharides. The column compartment was thermostated at 80°C while the RID was kept at a constant temperature of 40°C.

HPLC calibration

Calibration curves were done by the analysis of concentrate and diluted solutions (1:2, 1:10 and 1:20) of glucose and main reaction products (glucaric acid, gluconic acid, glycolic acid, tartronic acid, tartaric acid, oxalic acid, lactic acid, 2-keto-D-gluconic acid, 5-keto-D-gluconic acid, fructose, mannose, arabinose, formic acid, glyceric acid and mesoxalic acid) in HPLC instrument under the conditions presented previously. The response factor was obtained for each substance as the slope of the calibration curve.

Quantitative analysis of reaction mixture

The estimation of the moles of reaction products was carried out by dividing a peak's area on the chromatogram by the response factor obtained in the calibration:

$$n_i = (A_i/m_i) * (V/1000)$$

Where n_i is the number of moles of compound i, A_i is the area of the peak corresponding to the compound i, m_i is the response factor of the compound i, and V is the final volume of the reaction mixture.

Some analytes had overlapping peaks owed to similar retention times: gluconic acid (GO) and glucose (GLU), glyceric acid and arabinose. In the first case, RID detects quantitatively both GLU and GO, while DAD only GO. Hence, glucose peak area was calculated by subtracting gluconic acid peak area from RID chromatogram, converted to DAD chromatogram:

$$A_{GLU} = A_{RID\ GLU+GO} - (A_{DAD\ GO} * m_{RID\ GO} / m_{DAD\ GO})$$

Where $A_{DAD\ GO}$ is gluconic acid peak area in DAD chromatogram, $A_{RID\ GLU+GO}$ is the glucose and gluconic acid total peak area obtained from RID chromatogram, $m_{RID\ GO}$ is the response factor relative to gluconic acid in RID, $m_{DAD\ GO}$ is the response factor relative to gluconic acid in DAD. The obtained area was then used in the general formula for the estimation of the moles of any compound using glucose's response factor.

In the case of glyceric acid and arabinose, there was no proportion between the theoretical sum of single areas and the overlapping peaks' area in the chromatogram. Instead, as these two compounds had a similar response in RID, an average response factor was obtained:

$$m_{arabinose+glyceric\ acid} = (m_{arabinose} + m_{glyceric\ acid})/2$$

Where $m_{arabinose+glyceric\ acid}$ is the average response factor, $m_{arabinose}$ is the response factor relative to arabinose, $m_{glyceric\ acid}$ is the response factor relative to glyceric acid. The overlapping peaks' total area in RID chromatogram was used together with the average response factor in the general quantification formula to obtain a cumulative result of arabinose and glyceric acid moles.

Conversion is defined as the consumed reactant over the initial amount of reactant. Glucose conversion was consequently calculated as:

$$X_{GLU}\% = (n_{GLU,t=0} - n_{GLU,t=f})*100\ /\ n_{GLU,t=0}$$

Where $X_{GLU}\%$ is glucose conversion, $n_{GLU,t=0}$ is the initial number of glucose moles, $n_{GLU,t=f}$ is the final amount of glucose moles.

Yield is defined as the amount of product formed over the initial amount of reactant. For a given product (i), the yield was normalized with respect to the number of C atoms in the product molecule over the number of C atoms in glucose molecule.

$$Y_i\% = (n_i * C_f\ /\ n_{GLU,t=0}) * 100$$

$$C_f = C\ atoms\ in\ product\ molecule/\ C\ atoms\ in\ glucose\ molecule$$

Where $Y_i\%$ is the yield of product (i), n_i is the amount of moles of the product (i), $n_{GLU,t=0}$ is the amount of initial moles of glucose, C_f is the normalization factor for carbon atoms.

Selectivity is defined as the amount of product (i) over the total amount of reactant converted and was calculated by dividing the yield of product (i) by glucose conversion:

$$S_i\% = Y_i*100\ /\ X_{GLU}$$

Where $S_i\%$ is the selectivity of product (i), Y_i is the yield of product (i), X_{GLU} is glucose conversion.

3. Nanoparticles from cluster beam deposition

3.1. Synthesis and characterisation of materials

Ag and Au were supported on TiO_2 powder in the form of nanoparticle/nanocluster through cluster beam deposition. The samples were characterised using XPS, TEM, ICP-AES and BET to understand the morphology (particle size, oxidation state of metal) and surface metal and support composition.

3.1.1. TEM analysis

Two cluster catalysts were prepared by deposition of Ag and Au onto TiO_2 (P25, Sigma-Aldrich) powder supports. Nanoparticle diameter distributions, average nanoparticle size and the typical HAADF-STEM images of the two samples are shown in figure 18. The appearance, in both cases, showed results in well-dispersed metal clusters over the surface of supports without any noticeable agglomeration. In HAADF images, increasing Z number of the atoms results in a brighter image. Hence, the observed Au clusters are much brighter than the Ag clusters ($Z_{Au} = 79$, $Z_{Ag}=47$). Nanoparticle diameter distribution is similar for both samples, as they show similar average nanoparticle sizes (5,9 nm for Ag and 5,3 nm for Au), although the nanoparticle size distribution is slightly broader for Ag. The produced nanoparticles resulted larger than expected, as the MACS can potentially produce nanoclusters of subnanometric size, below 1 nm.
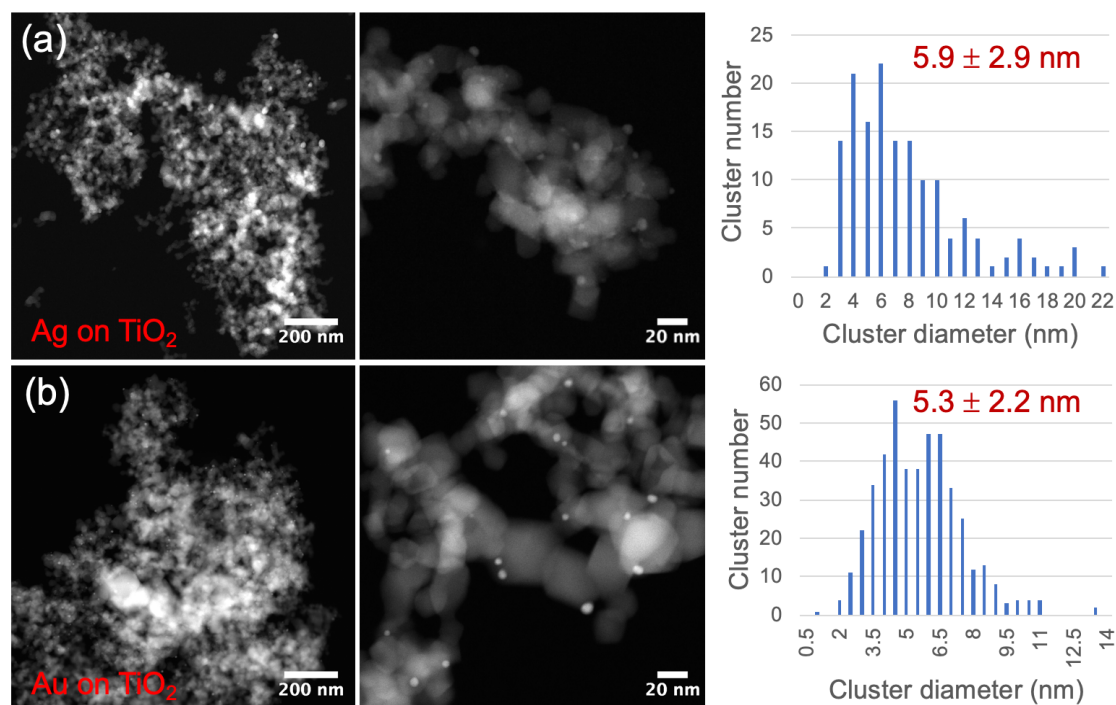

Figure 18 - Typical HAADF-STEM images with two magnifications and the corresponding cluster diameter distribution of the produced cluster catalysts. (a) Ag on TiO_2; (b) Au on TiO_2.

3.1.2. XPS

X-ray photoemission spectroscopy was used to determine the oxidation states of the species on the materials surface after air exposure. For the Au and Ag the 4f region for Au and 3d region for Ag, which are the typical regions for analysing the presence and the oxidation state of Au and Ag, were used.
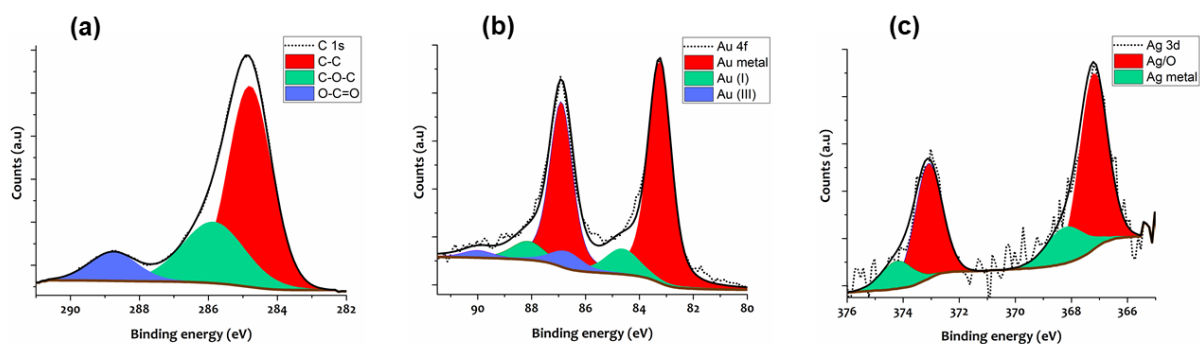

Figure 19 - X-ray photoelectron spectroscopy of the Au/TiO$_2$ and Ag/TiO$_2$ as-deposited samples after air exposure. C 1s (a), Au 4f (b) and Ag 3d (c) high-resolution spectra showing the deconvolution of each regions.

C 1s characteristic peak at a binding energy of 285 eV (figure 19(a)) was used for the calibration of the spectrum. The Au 4f region (figure 19(b)) shows well separated spin-orbit components (= 3.7 eV) with a main peak located at 83.2 eV compared to 84 eV often reported in the literature[78], indicating a negative shift in binding energy of 0,8 eV and it shows the presence of Au in metallic state (Au(0)). This shift in binding energy can be related to the cluster-support interaction, that influences the rounding degree of the Au clusters[79] and could determine a process of electron transfer from the TiO$_2$ to the Au cluster. Moreover, the reduction in the coordination number of Au atoms should be considered too. The other doublets peaks in the Au 4f spectra shown in figure 19(b) at 84.6 eV and 86.7 eV are commonly observed in Au clusters and attributed to Au^{1+} and Au^{3+} states, respectively. As the most intense peak in this region corresponds to Au(0), it is possible to conclude that the gold supported on TiO$_2$ is mainly in the metallic state, with minor contribution of Au$^{1+,3+}$ species.

The Ag 3d region is shown in figure 19(c), consisting in two main doublet peaks. The smaller peak at 368,2 eV, in good agreement to literature[80], corresponds to silver in the metallic state (Ag(0)). At lower binding energy (1 eV of difference) is found a more intense peak. This particular separation of Ag 3d peaks is known to coincide with AgO[81]. Clearly, part of the silver that was deposited in the form of clusters in vacuum conditions oxidized after air exposure, which is typical the case of small nanoclusters, especially Ag, Pd and Pt that show high affinity ot oxidation in the presence of air.

Interaction at the interface of silver clusters with titania could have played a role in the oxidation, as reported for other systems such as Ru or Pd clusters on oxide supports[82].
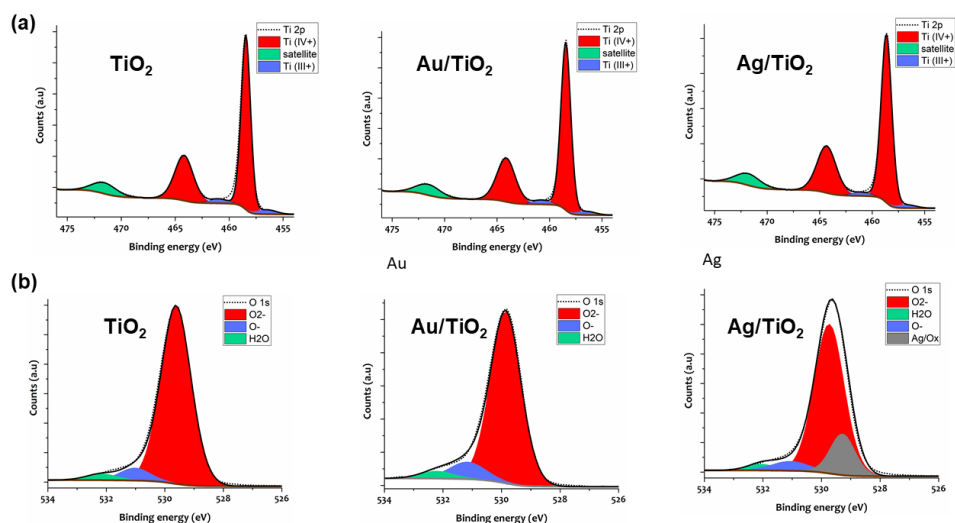

Figure 20 – X-ray photoelectron spectroscopy of the TiO_2, Au/TiO_2 and Ag/TiO_2 as-deposited samples after air exposure. Curved-fitted as-measured (a) Ti 2p and (b) O 1s for the three different samples. All spectra are charged reference with the C-C carbon to correct the binding energy in all cases.

Figure 20 shows the high-resolution spectra regions of Ti 2p and O 1s for Au/TiO_2, Ag/TiO_2 and TiO_2. For each sample, the deconvolution of Ti 2p spectrum reveals the predominance of Ti^{4+} species while a small contribution of Ti^{3+} species can be observed too[83]. In regard to O 1s spectra, the main contributions are attributed to O2- and O- species, separated by an energy gap of 1,4 eV in agreement with literature[83]. In the Ag/TiO_2 catalyst, an additional peak can be observed which corresponds to silver oxide (AgO).

O:Ti ratio was calculated for each sample to understand the influence of the clusters on the physico-chemical state of the TiO_2 support. The atomic ratio between O^{2-} and Ti^{4+} is equal to 1.5, 1.5 and 1.85 for the TiO_2, Au/TiO_2 and Ag/TiO_2 samples respectively. The higher O:Ti of Ag/TiO_2 demonstrates a significant reduction of the support compared to Au/TiO_2 and TiO_2 reference. This confirms that oxidation of silver does not happen only by air exposure, but also at the interface with the support. The increased oxygen vacancies on the Ag/TiO_2 surface could have great influence on the catalytic activity of the Ag/TiO_2 catalyst.

Elemental composition of Au/TiO_2 sample allowed to determine its compositions in terms of percentage of atoms for each element. Three positions of the sample were taken into account for the analysis (table 4). Au atoms are present on the material's surface at (0,33±0,08) %.

	Ti (At%)	O (At%)	Au (At%)
Position 1	58,8	40,8	0,28
Position 2	60,0	39,7	0,27
Position 3	60,5	39,0	0,44
Average	59,7±0,7	39,8±0,7	0,33±0,08

Table 4 – Elemental analysis of Au/TiO$_2$ surface composition by XPS.

3.1.3. ICP-AES for determination of metal loading

With the MACS system, the number of nanoclusters produced is proportional to the current of the ion gun and to the time of ion sputtering, but unlike chemical nanoparticle synthesis it is not yet possible to assume a quantitative deposition of the nanoclusters onto the support. Hence, the determination of the actual loading by ICP-AES analysis or equivalent techniques is a crucial step in the characterisation of the materials. The expected range for Au/TiO$_2$ and Ag/TiO$_2$ was between 1 wt.% and 0,1wt.%. Ag/TiO$_2$ metal loading resulted of 0,15 wt%. Only the analysis of Ag/TiO$_2$ appear in this work because the analysis were carried out by an external laboratory and the results for Au/TiO$_2$ did not arrive on time for the submission of the thesis.

3.1.4. BET surface area

The BET surface area and pore radius of the prepared materials and of the blank support TiO$_2$ were measured and the results are reported in table 5. Catalytic performance is often influenced by surface area.

Sample	Surface area (m^2/g)	Pore radius (A)
Ag on TiO$_2$	23,9	15,6
Au on TiO$_2$	24,2	22,0
Blank TiO$_2$	28,0	22,6

Table 5 – Summary of BET surface area results.
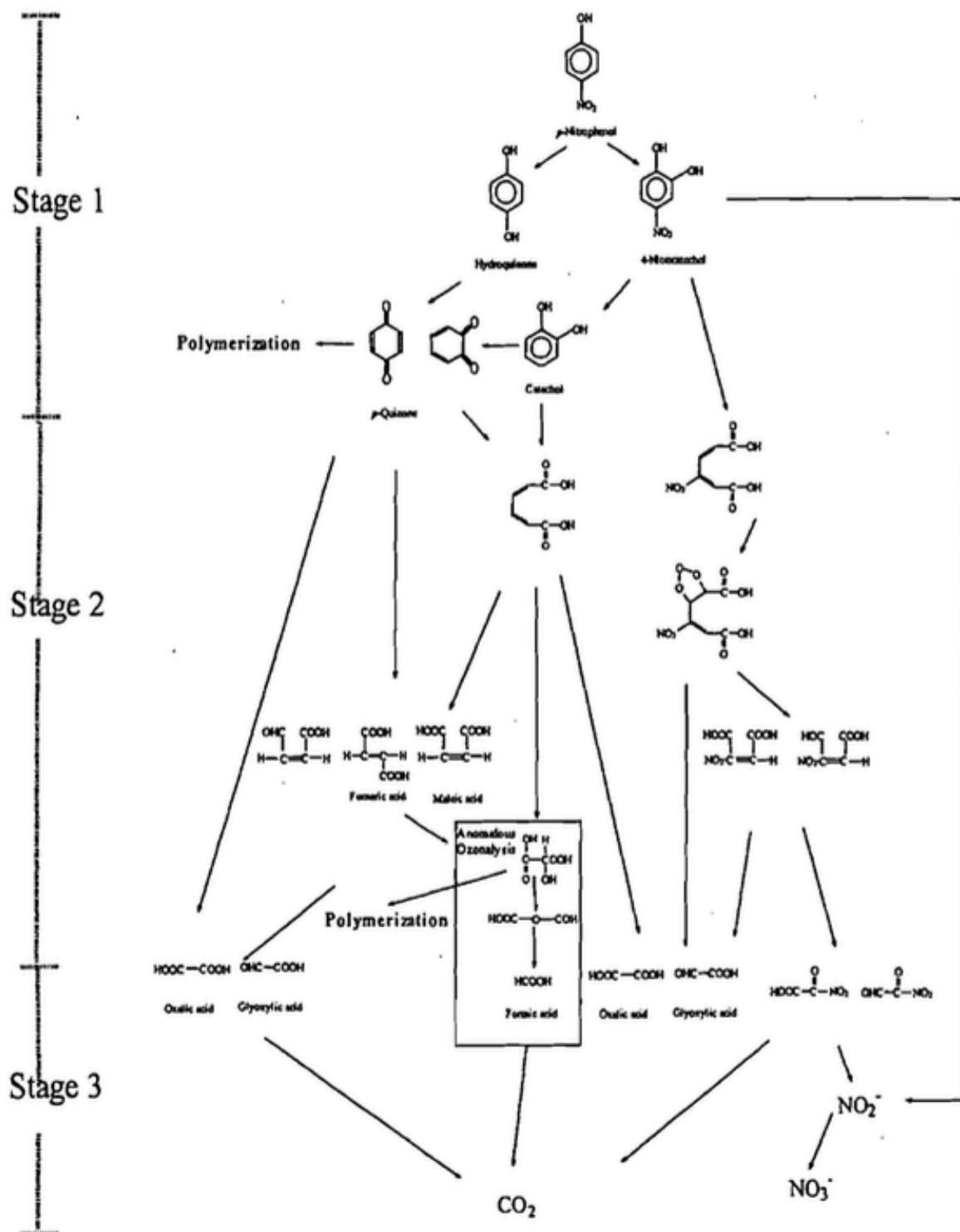
3.2. Nitrophenol catalytic ozonation

Figure 21 – Detailed scheme of 4-NP degradation branched mechanism by reaction with O_3 in water.

The reaction scheme was introduced in the introduction chapter in figure 7. A more detailed scheme can be found in figure 21: 4-NP molecule can undergo electrophilic attack by ozone or hydroxyl radicals; after a number of quinone intermediates, the C6 ring breaks down into a series of C4, C2 and C1 compounds such as maleic acid, oxalic acid, acetic acid, formic acid and eventually CO_2.

Oxalic acid does not react with the electrophilic O_3, and simple ozonation of nitrophenol (and other phenolic compounds) leads to a build-up in oxalic acid concentration[84]. For this reason, advanced oxidation processes are required not only to accelerate 4-NP degradation, but also to fully mineralise the organic molecules that appear as the reaction evolves[52].

The nanomaterials prepared with the MACS in Swansea University, Ag/TiO_2 and Au/TiO_2, were tested for catalytic ozonation of 4-nitrophenol. Since the materials required some time to be produced, Ag/TiO_2 was the first to be available for testing. Most of the tests are executed on this material; Au/TiO_2 was ready only in a second moment and its catalytic activity was tested for comparison purposes. The main purpose of this section is to prove the catalytic activity of Ag/TiO_2 and Au/TiO_2 prepared with "MACS 3", as they were the first materials to be produced by this instrument. Further studies are required to obtain an accurate description of the catalytic mechanism.

In this section are reported: Ag/TiO_2 test for adsorption of 4-nitrophenol; comparison of reaction rates of Ag/TiO_2 and Au/TiO_2, compared with the reaction rates of $TiO2$ powder and direct O_3 reaction; an exploration of pH and O_3 concentration in gas flow to investigate their effect on catalytic activity of $Ag/TiO2$; Ag/TiO_2 catalyst reusability was eventually tested over 5 cycles.

3.2.1. Adsorption test

$TiO2$ and Ag/TiO_2 were tested for nitrophenol adsorption, as it is known that physical adsorption onto the support can mask catalytic activity. J. Nawrocki pointed out in a discussion paper[85], an important consideration when studying catalytic activity of a material in heterogeneous catalytic ozonation is adsorption of organic molecules onto the material taken into examination. Measuring the absorbance of nitrophenol at 400 nm in the UV-Vis spectrum recorded after 20h of stirring at 50 rpm in presence of the catalysts does not show any difference with the absorbance of the blank solution. From the measurements, $TiO2$ and Ag/TiO_2 did not adsorb 4-nitrophenol. The removal of 4-NP during adsorption at different catalyst concentrations is negligible, indicating that 4-NP concentration consumption in the catalytic tests is caused only by reaction.

3.2.2. Catalytic activity of materials

The materials prepared, Ag/TiO_2 and Au/TiO_2, were tested for the catalytic activity of the ozonation reaction with 4-NP comparing their activity to ozonation with O_3 only and with TiO_2 powder. In each experiment 4-nitrophenol concentration, gas flow, ozone concentration, stirring and pH were kept constant: $0,1\mu M$, 500 mL/min, 10 g/m^3 NTP, 500 rpm and pH 9 respectively. 4-NP concentration was limited by the saturation of the UV-vis signal, since 4-NP has a really high molar exctintion coefficient, about 18000 L mol^{-1} cm^{-1} at λ_{max}=400 nm. Nitrophenol direct ozonation has already been reported to be influenced by pH in an extensive study on this reaction by Beltrán and coworkers[6].
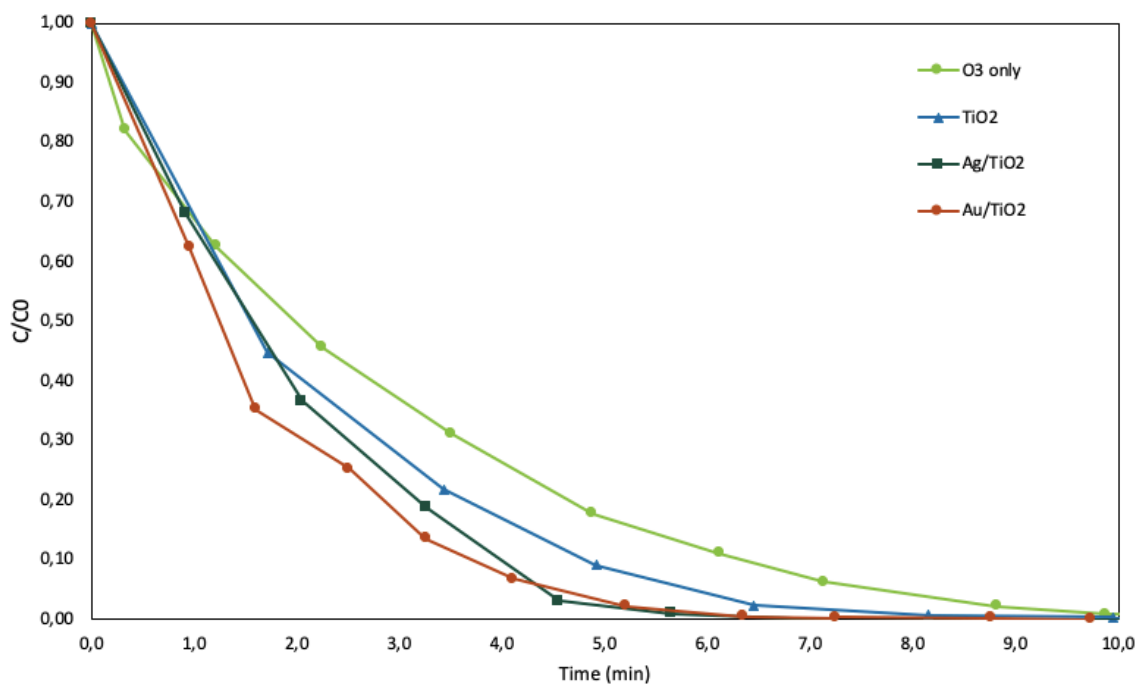
Figure 22 - Normalized 4-NP absorbance as a function of time for direct ozonation reaction (O_3 only) and for ozonation catalysed by TiO_2, Ag/TiO_2, or Au/TiO_2. Experimental conditions: [4-NP] = 0,1μM, gas flow=0,500 mL/min, [O_3] in gas flow = 10 g/m3, pH=9, [catalyst]=250 mg/L.

It was reported that 4-NP degradation rate increased from pH 2,0 to pH 8,5 after which the rate stabilized. In this study another important parameter is ozone partial pressure, or concentration, in the gas feed. The ozone degradation rate increased as did O_3 partial pressure. They concluded that 4-NP ozonation is mainly controlled by mass transfer and high ozone partial pressures in the gas feed are required to favor O_3 diffusion into the water solution. For these reasons, the pH value was set to 9 and [O_3] in the gas feed was set to the highest value reached by the ozone generator, 10 g/m³.

For each reaction, 50 mg of catalyst were added to a glass reactor containing 200 mL of 4-nitrophenol solution. Optical absorbance of the solution was recorded over time to monitor the progress of the reaction. To analyse 4-nitrophenol concentration, the absorbance at 400 nm was taken into account as it corresponds to its peak at a basic pH. The normalized concentration of nitrophenol, C/C_0, versus time[50] is shown in figure 22.

Nitrophenol concentration decreases rapidly with time and reaches full consumption for all the reactions tested in a period of 10 minutes. The reaction catalyzed by Au/TiO_2 shows a very steep curve especially in the first two minutes, eventually reaching a conversion >99% in 6 minutes. Comparatively, 4-NP removal with Ag/TiO_2 achieved a removal of >99% in slightly more than 5 minutes; the same reaction with TiO_2 powder took 8 minutes while the direct ozonation reached complete conversion at 10 minutes. Thus, this analysis allows to conclude that supported metal clusters effectively accelerate the ozonation reaction with 4-NP.
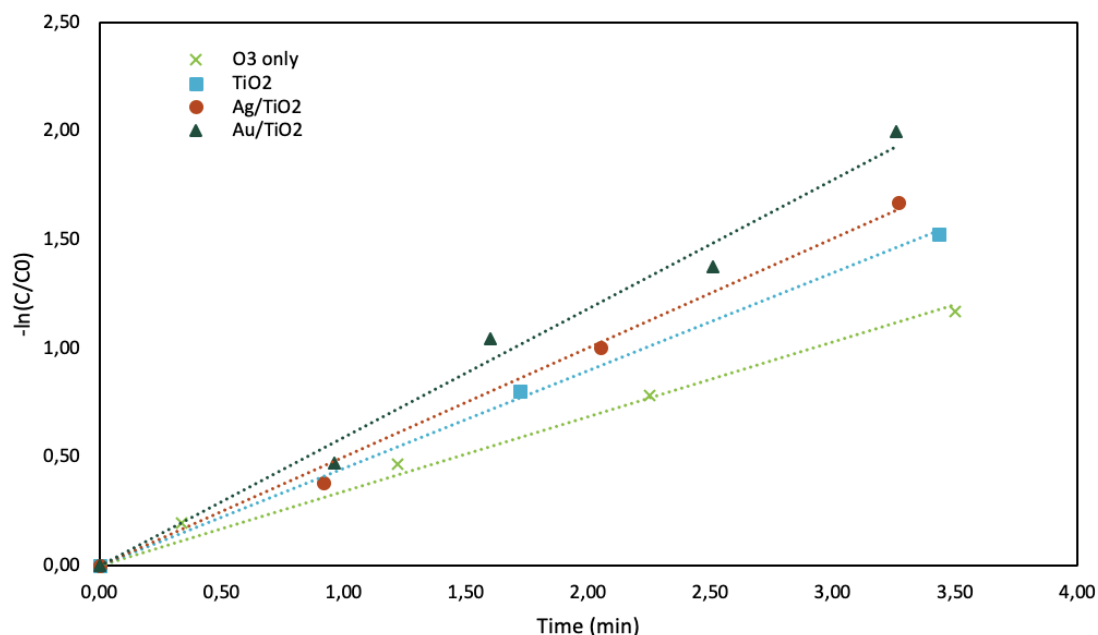
Figure 23 - The pseudo first-order reaction plots for the direct ozonation (O3 only), TiO$_2$, Ag/TiO$_2$, or Au/TiO$_2$ catalysed reactions. Experimental conditions: [4-NP]=0,1µM, gas flow =500 mL/min,[O3] in gas flow =10 g/m3, pH=9, [catalyst]=0,25 g/L.

4-nitrophenol ozonation reaction follows a highly branched mechanism (figure 21), as O$_3$ is a quite unselective reactant. For this reason, only the initial measurements have been considered for the calculations of the experimental kinetic constants. In fact, as the reaction progresses over time the secondary products (quinones, maleic acid, oxalic acid, acetic acid and formic acid) might consistently give secondary reactions with ozone, interfering with the main reaction. The experimental data were suitably described by a pseudo-first-order kinetic constant (k_{exp}) within the first 4 minutes. A comparison of the reaction rates was allowed by the values of k_{exp} obtained.

Sample	K_{app} (min^{-1})
O$_3$ only	0,32
TiO$_2$	0,44
Ag/TiO$_2$	0,52
Au /TiO$_2$	0,60

Table 6 – Apparent reaction rates for the ozonation of 4-nitrophenol for the direct or catalysed reaction. Experimental conditions: experimental conditions: [4-NP]=0,1µM, gas flow =500 mL/min,[O3] in gas flow =10 g/m^3, pH=9, [catalyst]=0,25 g/L

The pseudo-first-order rate constant of Au/TiO$_2$ (0,60 min^{-1}) was almost two times higher than direct ozonation (0,32 min^{-1}) (figure 23). Just below the gold based-catalyst is Ag/TiO$_2$, with a k_{app} of 0,52

min^{-1}. Silver and gold nanoparticles also show an enhanced catalytic activity in respect to TiO$_2$ powder, which k$_{app}$ reaches only 0,44 min^{-1}.

3.2.3. pH test

To evaluate the influence of pH on 4-NP removal during catalytic ozonation, the reaction was carried out at three different values of pH: 3, 5 and 9 (figure 24). It can be seen that the degradation of 4-NP is clearly inhibited at acidic pH and it is enhanced at basic pH, suggesting that hydroxyl radical play a fundamental role in 4-NP degradation in accordance to the literature [50] and that the main activity of the catalyst might be the production of radicals by O$_3$ decomposition rather than a direct reaction with organic molecules.
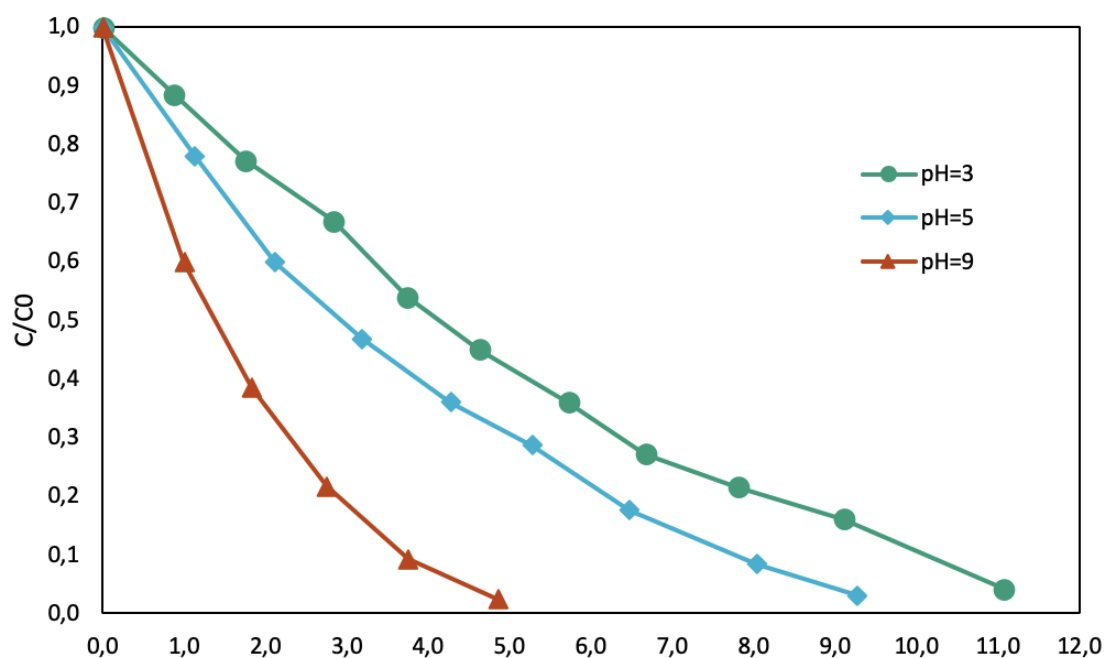

Figure 24 - Normalised 4-NP concentration as a function of time during ozonation with Ag/TiO$_2$ at different pH values. Experimental conditions: [4-NP] = 0,1μM, gas flow=0,500 mL/min, [O$_3$] in gas flow = 10 g/m^3, [catalyst]=250 mg/L.

The reaction reached a degradation of >95% after 5 minutes when the pH is ~9. When the pH is decreased to 5, the reaction takes almost double the time reaching a 4-NP consumption above 95% at 9 minutes; time which becomes 11 minutes when the pH is further lowered to 3. It is possible to observe that pH has a stronger effect when the reaction is catalysed. 4-nitrophenol has a pKa of 7,15. At acidic pH, it is found mainly in the protonated, charge-neutral form; whereas at a pH=9 it is in the negatively charged form. In figure 25 the dissociation of nitrophenol into nitrophenolate is plotted to give a visual representation of the composition of a nitrophenol solution at a given pH.

Sample	pH	k_{app} (min^{-1})
O$_3$	3	0,181
TiO$_2$	3	0,152
Ag/TiO$_2$	3	0,194
O$_3$	5	0,194
TiO$_2$	5	0,192
Ag/TiO$_2$	5	0,260
O$_3$	9	0,339
TiO$_2$	9	0,444
Ag/TiO$_2$	9	0,520

Table 7 – Apparent reaction rates for ozonation of 4-nitrophenol by direct reaction with O$_3$, catalysed by TiO2 and by Ag/TiO$_2$ at pH 3, 5 and 9. Experimental conditions: [4-NP] = 0,1μM, gas flow=0,500 mL/min, [O$_3$] in gas flow = 10 g/m^3, [catalyst]=250 mg/L.
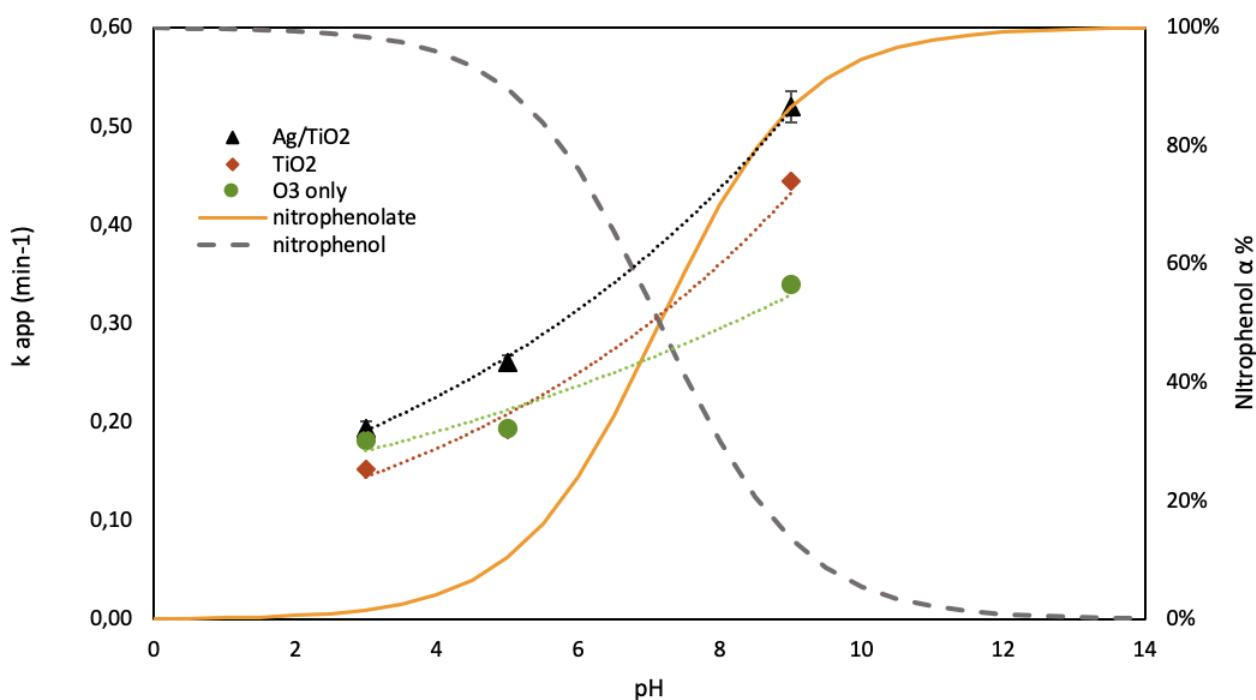

Figure 25 – Effect of pH on the experimental kinetic constant for direct ozonation, TiO$_2$ and AgTiO$_2$ catalysed reactions.

3.2.4. O$_3$ concentration

Due to the multiphase composition of the reaction system, changes in the ozone concentration in the gas are expected to affect the reaction rate. The system is a triphasic reactor, also known as slurry: one reactant, ozone is in gas phase; the other reactant, 4-nitrphenol, is in aqueous phase; the catalyst being heterogeneous constitutes a third phase. Ozone concentration in the gas flow affects the concentration of O$_3$ in water and the latter the concentration of the same species on the surface of the

catalyst. Hence, the effect of ozone concentration on the reaction rate was investigated in a range of 3 g/m^3 to 10 g/m^3 and the results are shown in figure 26. Ag/TiO$_2$ was tested for enhanced catalytic activity, using as a reference the reaction with TiO$_2$ and simple ozonation.

Sample	[O$_3$] in gas feed (g/m^3)	k_{app} (min^{-1})
O$_3$	3	0,14
TiO$_2$	3	0,16
Ag/TiO$_2$	3	0,16
O$_3$	6	0,34
TiO$_2$	6	0,40
Ag/TiO$_2$	6	0,33
O$_3$	10	0,34
TiO$_2$	10	0,44
Ag/TiO$_2$	10	0,53

Table 8 - Apparent reaction rates for ozonation of 4-nitrophenol by direct reaction with O$_3$, catalysed by TiO$_2$ and by Ag/TiO$_2$ at [O$_3$] in gas flow = 3, 6 and 10 g/m^3. Experimental conditions: [4-NP] = 0,1µM, gas flow=0,500 mL/min, pH = 9, [catalyst]=250 mg/L.

 At the lowest O$_3$ concentration tested, the three reactions show a very similar rate. This can be explained by mass transfer phenomena. When O$_3$ concentration in gas phase is too low, the mass transfer resistance is located at the gas liquid interface. Hence, the rate-determining step is the transfer of O$_3$ from the gas phase to the liquid phase. Increasing the ozone concentration to 6,0 g/m^3 brings the three reactions to a faster rate, having a stronger influence on TiO$_2$ than on the other two reactions. In fact, Ag/TiO$_2$ catalysed reaction shows the same rate as the O$_3$-only. Likely, ozone mass transfer to the liquid phase doesn't represent the rate determining step, but another resistance might be at the interface between bulk liquid phase and the Ag/TiO$_2$ surface that results in masking catalytic activity. The fact that TiO$_2$ instead shows an enhanced activity also implies that the surface area of the solid with Ag clusters has a decreased surface area. At the highest concentration tested, O$_3$-only reaction has the same rate as the with the previous O$_3$ concentration: the maximum rate for nitrophenol direct ozonation was reached at [O$_3$] = 6 g/m^3, with ozone saturation of the liquid phase and resulting in a pseudo-first order reaction for nitrophenol. TiO2 experimental constant slightly rises compared to the intermediate ozone concentration, but not quite as much as much. Nevertheless, at [O$_3$] =10 g/m^3, the highest reaction rate is given by Ag/TiO$_2$. In particular, the rates for this reaction show a linear proportionality with ozone concentration in gas flow. If the latter was to be further increased at the same reaction conditions, the apparent kinetic constant shout increase too.
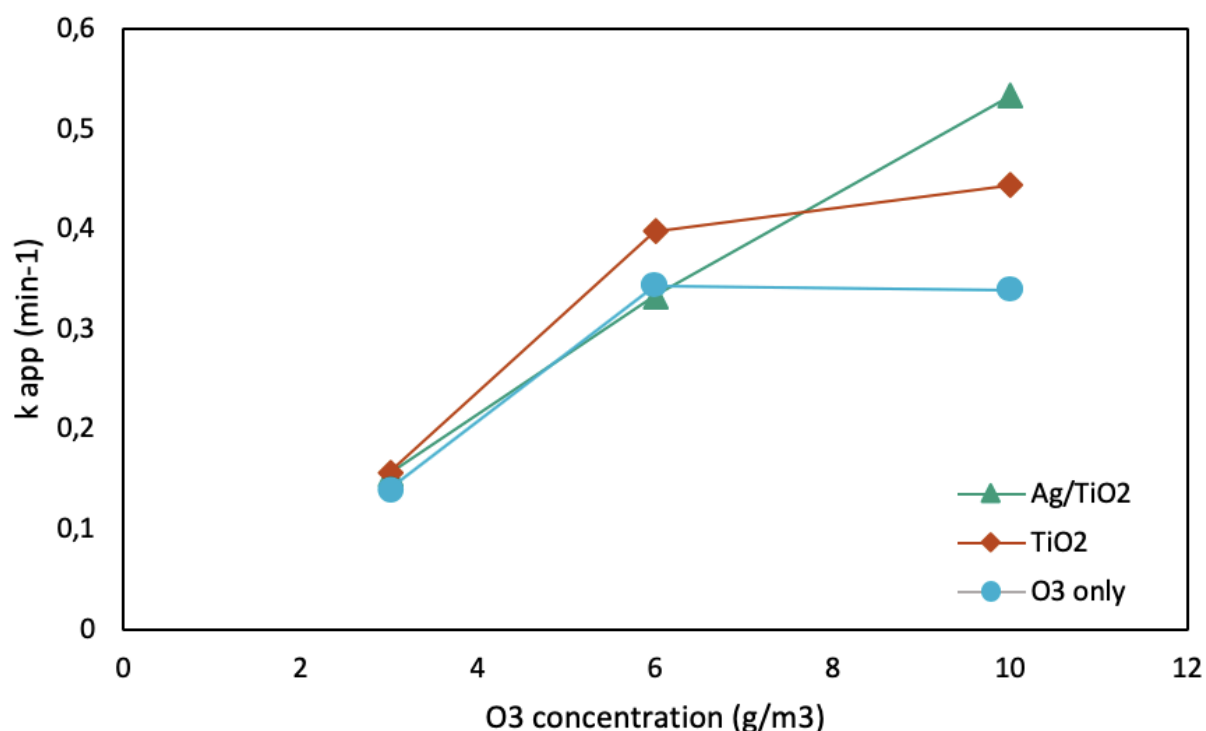
Figure 26 – Experimental kinetic constants for direct ozonation, TiO_2 and Ag/TiO_2 catalysed reactions at different O_3 concentrations in the gaseous mixture. Experimental conditions: [4-NP]=0,1μM, gas flow=0,500 mL/min, pH= 9, [catalyst]=250 mg/L.

3.2.5. PZC

This experiment was performed to determine the surface charge variation of the solid with pH. Figure 27 represents the results obtained with the method explained in the experimental section applied to Ag/TiO_2. At low initial pH values, the difference with the final values is only slightly positive, very close to zero. Then as the initial pH values increase, the difference becomes negative. The isoelectric point of the material was identified when the experimental curve crosses the x-axis, marking the passage from positive surface charge to negative surface charge. For Ag/TiO_2, this point was determined at a pH value of 4,3.
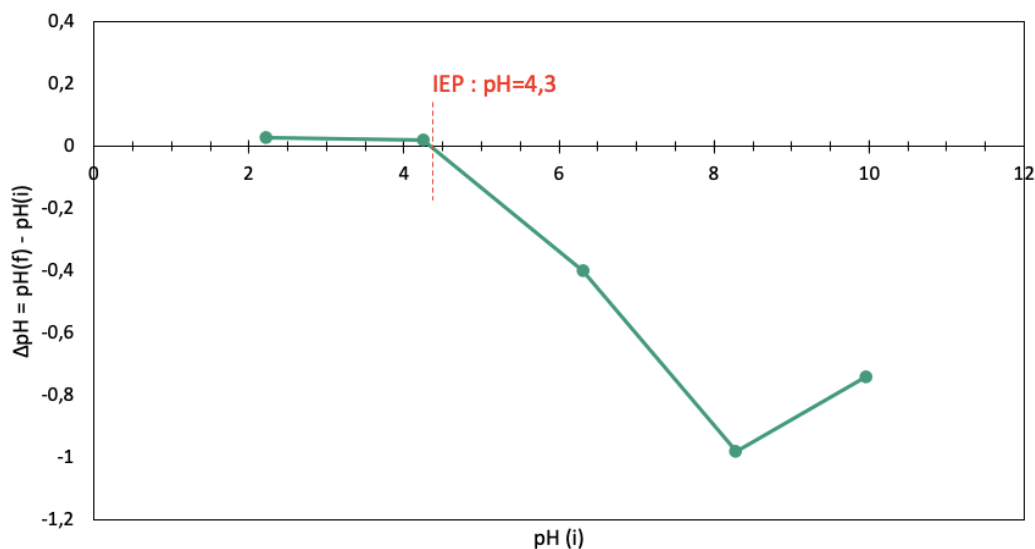
Figure 27 – Experimental curve for PZC determination. IEP (isoelectric point) is found at a pH=4,3.

3.2.6. Reusability

Reusability of heterogeneous catalysts is an important aspect of heterogenenous catalysis, since long-term stability is crucial for developing sustianble chemical processes. It is one of the main features and advantages when compared to homogeneous catalysts, considering its use in industry. In this study, the effect of catalyst reuse was investigated, and the results are shown in figure 28. The catalyst investigated was Ag/TiO$_2$. It was reused five times in succession and 4-nitrophenol conversion was calculated after 2 minutes of reaction time for each cycle. 4-nitrophenol reached above 60% conversion each time, the catalyst showing excellent stability. Between the 3rd and the 4th cycles the conversion increased of ~6%, albeit this is to consider within experimental error. No deactivation of the catalyst seemed to occur.
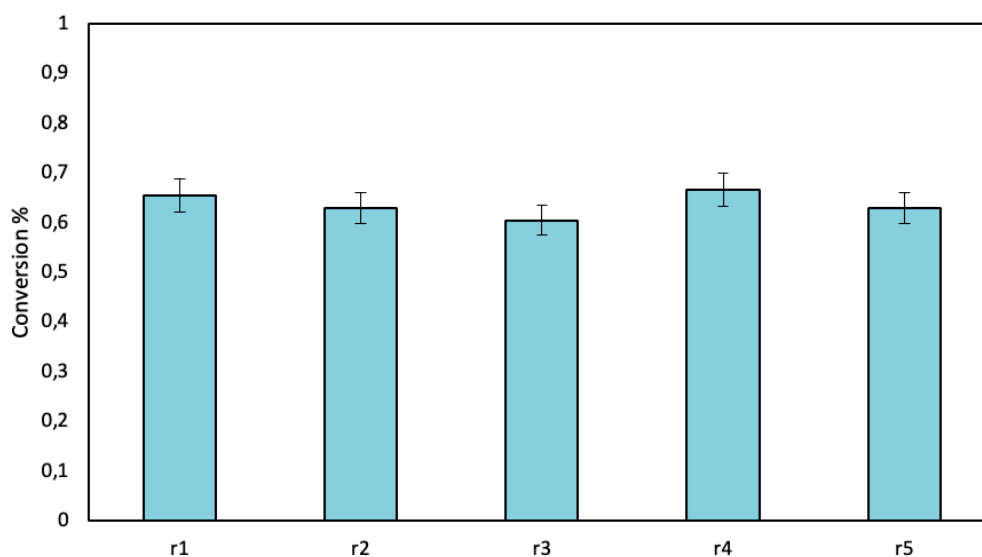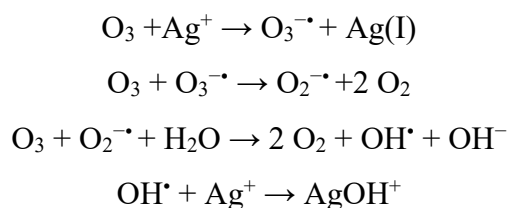

Figure 28 -Reuse test of Ag/TiO$_2$: 4-NP conversion after 2 minutes. Experimental conditions: [4-NP]=0,1µM, gas flow =0,500 mL/min, [O$_3$] in gas flow =10 g/m$_3$, pH=9, [catalyst]=250 mg/L.

In a study on ozone interaction with colloidal silver nanoparticles by Morozov et al[62]. they claim that silver reacts with ozone by oxidising itself to Ag(I), starting a chain reaction that involves three ozone molecules and produces various radical species:

$$O_3 + Ag^+ \rightarrow O_3^{-\bullet} + Ag(I)$$
$$O_3 + O_3^{-\bullet} \rightarrow O_2^{-\bullet} + 2\ O_2$$
$$O_3 + O_2^{-\bullet} + H_2O \rightarrow 2\ O_2 + OH^\bullet + OH^-$$
$$OH^\bullet + Ag^+ \rightarrow AgOH^+$$

They also reported an increase of the size of the Ag nanoparticles over time when O_3 was bubbling, which was attributed to a destabilisation of the colloid due to severe oxidation. However, the timescale of the phenomenon and of the reaction in this study are different, silver oxidation being slower. It is likely to think that silver nanoparticles are oxidising through the mechanism proposed but the reaction time is short enough to not to reach the total consumption of silver nanoparticles even after 5 cycles. Furthermore, the interaction between Ag nanoparticles and the support, TiO_2, might have a stabilising effect that prevents agglomeration of the nanoparticles.

3.2.7. Discussion

The results are in agreement with the results found by other groups[87,88]. It is important to consider that pH also affects ozone decomposition mechanism. As clarified by Ershov and Morozov[89], the decomposition of ozone into reactive radicals is catalysed by OH^-. To explain the effect of pH on catalysed reactions, surface charge of the catalysts must be taken into account through PZC. When the pH is higher than the PZC, the surface of the catalyst is overall negatively charged, as O^- groups are the main surface species. On the other hand, when the pH is lower than the PZC, the surface is positively charged (Ti-OH$_2^+$ sites mainly). Surface charge determines which species can be adsorbed: a negatively charged surface will attract positive ions and vice versa. It is then unlikely to think to nitrophenolate adsorbing onto the negatively charged catalyst surface at pH=9. On the other hand, O_3 can adsorb on the catalyst thanks to its polarizability as studied by Dhandapani et al.[90] where they focused on catalytic ozone decomposition in gas phase. It is generally accepted[56] that a similar mechanism is taking place in aqueous environment as well. Adsorption of O3 explains the induction time observed only with catalysed reactions: during the first moments after the onset of ozone bubbling, the kinetics of 4-NP degradation are slower than envisaged for a first-order reaction. As O_3 reaches an equilibrium with the catalyst, the reaction accelerates and shows a typical pseudo-first order pathway (figure 23). Note that for rate constant calculations, induction time is not contemplated,

and the reaction is considered to start at the time of the first measurement. This expedient was taken to guarantee a steady state in ozone behaviour.

3.3. Nitrophenol reduction

3.3.1. Catalytic activity

The synthesised supported nanoparticle catalysts were tested for the reaction of 4-nitorphenol reduction by NaBH4 in water. 30 mg of catalyst (Ag/TiO$_2$ and Au/TiO$_2$) were introduced in a volume of 70 mL of 4-NP 0,1µM aqueous solution and NaBH$_4$ in molar ratio of 50:1 in respect to 4-NP. The optical absorbance of the solution was monitored by recording UV-vis spectra over time to monitor the conversion of 4-NP. The decrease of the UV-vis peak at λ_{max} = 400 nm, corresponding to nitrophenol in NaBH$_4$ or alkaline solution, is shown in figure 29, using Au/TiO$_2$ as catalyst. 4-aminophenol, the only product of the reaction, has a weak UV-vis peak at λ_{max} = 300 nm. It is possible to observe that the absorbance at 300 nm is slightly increasing over time as the reaction progresses. From the absorbance at λ = 400 it is possible to derive 4-NP concentration thanks to Lambert-Beer law (A = ε * l *C; where A is the absorbance, ε is the molar extinction coefficient (expressed in M^{-1}cm^{-1}), l is the optical path length and depends on the cuvette (normally 1 cm), and C is the concentration of the species in the solution. The calibrated molar extinction coefficient for the UV-vis spectrometer used was ε = 18900 M^{-1}cm^{-1}. For Ag/TiO$_2$ similar results were obtained.
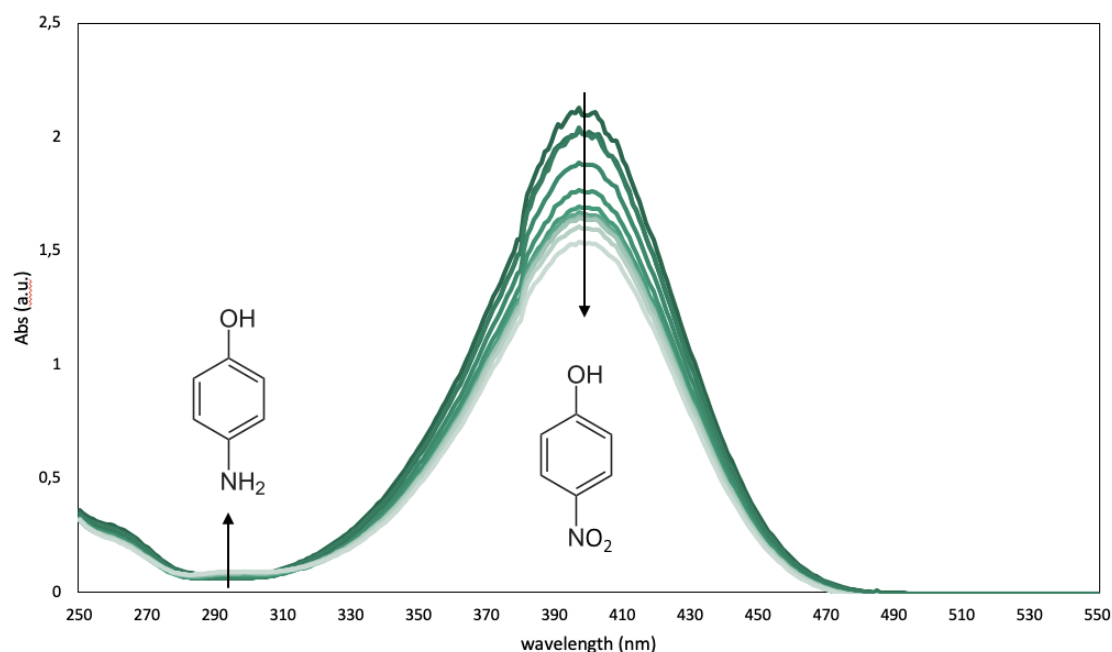

Figure 29 – Superimposed UV-vis spectra recorded at intervals of 5 minutes, of the reaction solution for the reduction of 4-nitrophenol by NaBH4 and supported Au nanoparticles as catalyst.
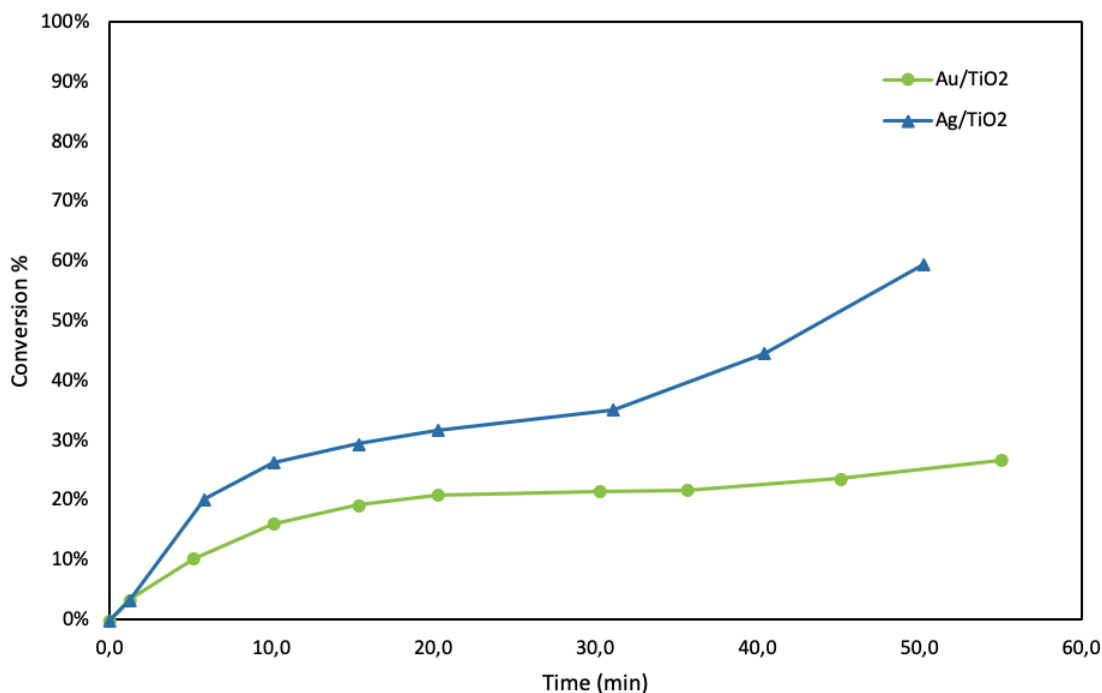
Figure 30 – 4-NP conversion over time for the 4-NP reduction reaction catalysed by Au/TiO$_2$ and Ag/TiO$_2$. Reaction conditions: initial [4-NP]= 0,1μM, NaBH4:4-NP = 50:1, [catalyst] = 0,43 g/L. MoreNaBH$_4$ was added after 30 minutes for both catalysts.
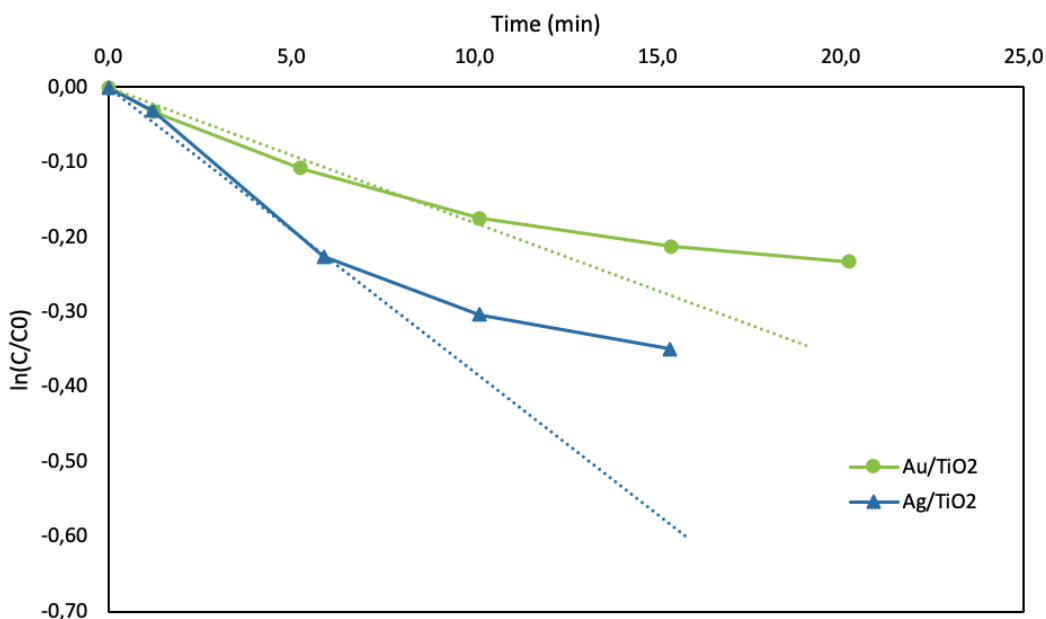

Figure 31 – Logarithmic plots of normalized 4-nitrophenol concentration over time. The slope represents the apparent reaction rate at initial time for Au/TiO$_2$ and Ag/TiO$_2$. C$_0$ and C represent 4-nitrophenol conversion at initial time and progressive over time.

After 20 minutes, the Ag catalyst achieved a conversion of 32%, whereas Au catalyst reached a conversion of 21% (figure 30). Since after 30 minutes the reaction had reached a plateau in 4-nitrophenol conversion, more reducing agent was added to the solution. Ag catalyst started to convert 4-nitrophenol again, reaching a conversion of 60% after a total reaction time of 50 minutes. Au

catalyst had a slow resumption of 4-nitrophenol conversion but still reached a final conversion of 27% after a total of 55 minutes. NaBH$_4$ consumption is very fast during the first 20 minutes of the reaction despite the initial excess of 50 equivalents to 4-NP.

When sodium borohydride is in rage excess in respect to 4-NP, it can be assumed that the reaction follows pseudo-first order kinetics[34,35] and the apparent reaction rate (k$_{app}$) can be obtained by extrapolation of the slope at initial time (figure 31). In fact, NaBH$_4$ consumption is fast, and the reaction kinetics leave the pseudo-first order after 5 minutes in the case of Ag and 10 minutes for Au. C$_0$ and C$_t$ represent the nitrophenol concentration at time 0 and t, respectively. The resulting apparent kinetic constants are $1,8*10^{-2}$ min^{-1} for Au/TiO$_2$ and $3,8*10^{-2}$ min-^{1} for Ag/TiO$_2$. In order to compare the apparent kinetic constants of the two samples, they should be normalized over the total moles of metal that constitute the active phase for each catalyst.

4. Catalysts from sol-immobilisation (colloidal method)

4.1. Synthesis and characterisation of catalysts

The catalysts were synthesised as described in chapter 2. In figure 32 the three stages of the synthesis are shown simultaneously. The diluted solution of gold precursor is a transparent, light yellowish solution; gold nanoparticles typically give red-coloured colloids when the nanoparticles are small and $NaBH_4$ is added as reducing agent; the addition of activated carbon as the chosen support for immobilising the preformed metal nanoparticles, makes the solution become totally black.
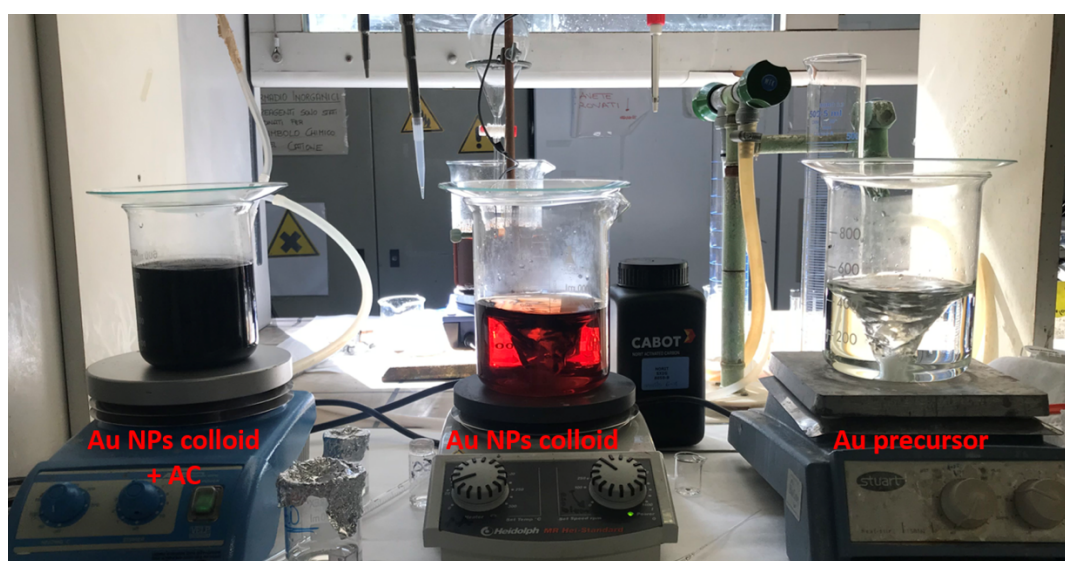

Figure 32 - A picture showing the three stages of catalyst synthesis. From left to right: Au NPs colloid to which has just been added the support, AC; colloidal solution of Au NPs showing the typical red colour; gold precursor.

Catalyst	Support	Polymeric stabilizing agent	Polymer:Au weight ratio	Separation method
Au/AC-PEG0,3	Activated Carbon	PEG	0,3:1	Filtration
Au/AC-PEG0,65	Activated Carbon	PEG	0,6:1	Filtration
Au/AC-PEG1,2	Activated Carbon	PEG	1,2:1	Filtration
Au/AC-PEG2,4	Activated Carbon	PEG	2,4:1	Filtration
Au/AC-PVP0,3	Activated Carbon	PVP	0,3:1	Filtration
Au/AC-PVP0,65	Activated Carbon	PVP	0,6:1	Filtration
Au/AC-PVP1,2	Activated Carbon	PVP	1,2:1	Filtration
Au/AC-PVP2,4	Activated Carbon	PVP	2,4:1	Filtration
Au/TiO$_2$-PVA-0,65	High Area TiO$_2$	PVA	0,65:1	Centrifuge

Table 9 - list of catalysts prepared with the methodology reported in section 2.1.1

In previous work on PVA-stabilised preformed Au nanoparticles it was found that varying the polymer:Au weight ratio in the colloidal solution affects the resulting nanoparticle size. Smaller nanoparticles were obtained at higher PVA concentrations, as the SPR peak shifted towards lower wavelengths in the UV-vis spectrum, as PVA concentration increased. The effect was confirmed by analysing the dimensions of the nanoparticles after immobilisation on AC both by means of XRD and TEM analysis of the samples. As a continuation, we want to investigate the concentration effect on nanoparticle size using two other different polymers, PVP and PEG.
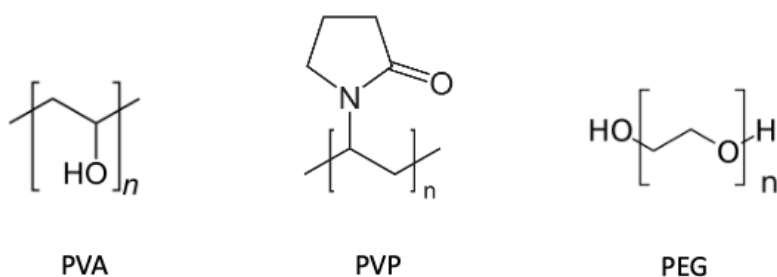

Figure 33 – chemical structure of the polymers PVA, PVP and PEG.

The three polymers have a very different chemical structure, as can be seen in figure 33, which causes them to stabilize and interact with Au nanoparticles in different ways. Regarding PVA (polyvinyl alcohol) it is generally accepted that the interaction with gold nanoparticles happens mainly by the -OH groups and is not particularly strong, i.e. no covalent bonds are formed. PVA is also known to allow synthesis of colloidal nanoparticles of small (2-3 nm) dimensions[91]. PEG (polyethylene glycol also known as PEO, polyethylene oxide) weakly interacts with Au nanoparticles and its main function is to give a steric stabilisation[92]. On the opposite, PVP (polyvinyl pyrrolidone) known to be an electron donor and through its C=O group and N goup on the pyrrolidone residue it can interact with Au nanoparticles[93]. Its preferential binding to Au (111) facet was also exploited to control morphological growth of Au NPs[94].

4.1.1. UV-Vis spectroscopy

The formation and stability of PEG and PVP metal (Au) colloidal solutions over time was investigated by UV-vis spectroscopic analysis. $AuCl_4^-$ anion in water has a peak absorbance at $\lambda_{max} = 222$ nm, while the typical SPR peak of small Au (0) colloidal nanoparticles is $\lambda_{max} = 490\text{-}520$ nm. Hence, it is possible to follow the precursor reduction by UV-vis spectroscopy[95].

A large number of studies confirmed that for Au colloidal nanoparticles a change in the peak position can be associated to a change in nanoparticle size. A shift at lower wavelengths is called a "blue shift" and can be interpreted as a decrease in nanoparticle size; conversely a "red shift" is seen when the particles become larger and the peak moves to higher wavelengths[96]. Many factors have an influence

on the peak's exact position, intensity and width: size, shape, concentration, aggregation, and dielectric properties of the surrounding (i.e. solvent and stabiliser type).
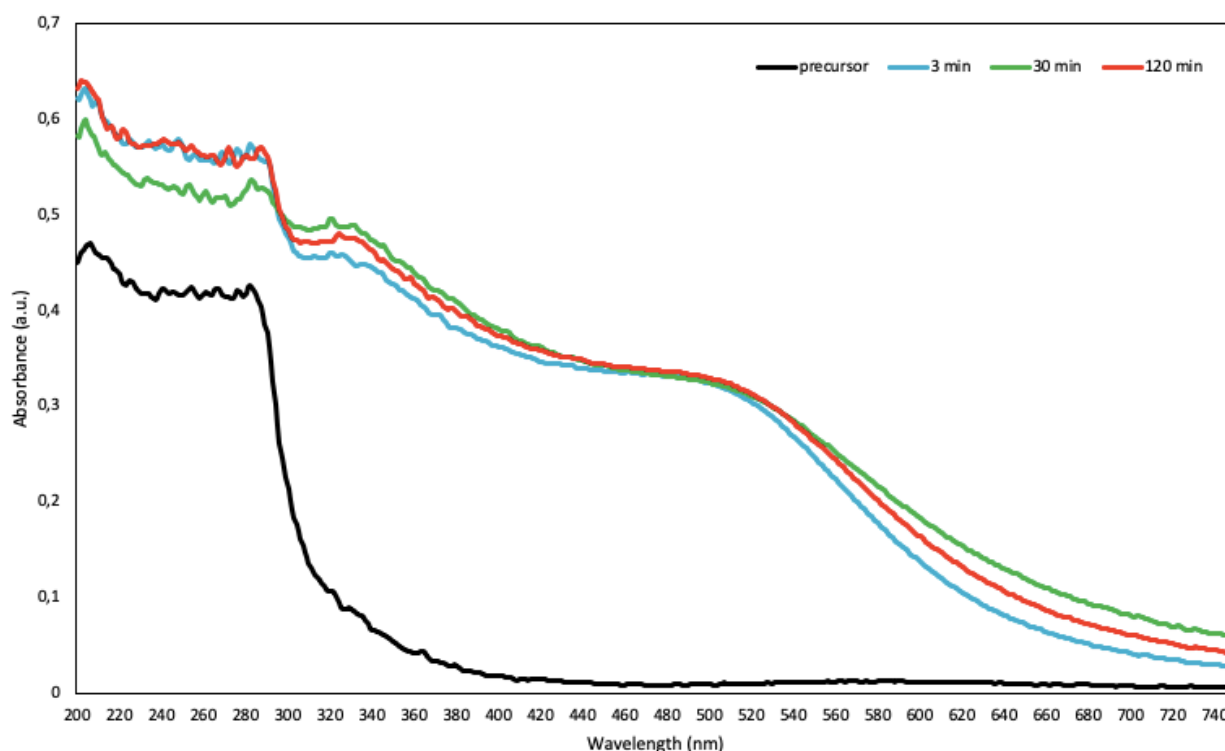

Figure 34 - UV-Vis spectra of gold precursor and colloidal gold nanoparticles at different times after addition of NaBH₄. The nanoparticles are stabilised by PVP at a weight ratio of 0,65 to gold.

Starting from the metal precursor, figure 34 shows that right after the addition of NaBH₄ (t=3min) the surface plasmon resonance (SPR) peak at about 500 nm, is clearly visible. It corresponds to the absorption of blue-green light, whose complementary colour is the red-orange that is typical of the colloids. After 30 minutes the peak shows a slight red shift which can be related to the ripening of the nanoparticles. A further spectrum recorded after 120 minutes and the UV-vis peak can be considered as unchanged. It can be concluded that the Au colloidal solution is stable over time and that there is no significant nanoparticle growth after 30 minutes. For this reason, 30 minutes is considered the optimal time to support the preformed colloidal nanoparticles.

Recording the UV-vis spectrum of the Au colloidal solution minutes prior to the addition of support is a way to control that the prepared nanoparticles are of dimensions below or around 10 nm and to check the stability and reduction of metal precursor. Figure 35 shows the spectra of the colloidal gold solutions at 25 minutes after addition of NaBH₄, with PVP or PEG at different PVP:Au or PEG:Au weight ratios. Among the various Au colloidal solutions, their corresponding gold SPR peak shows differences in position, shape and width from one another. It is a good indication of a differentiation in terms of nanoparticle size and/or morphology.
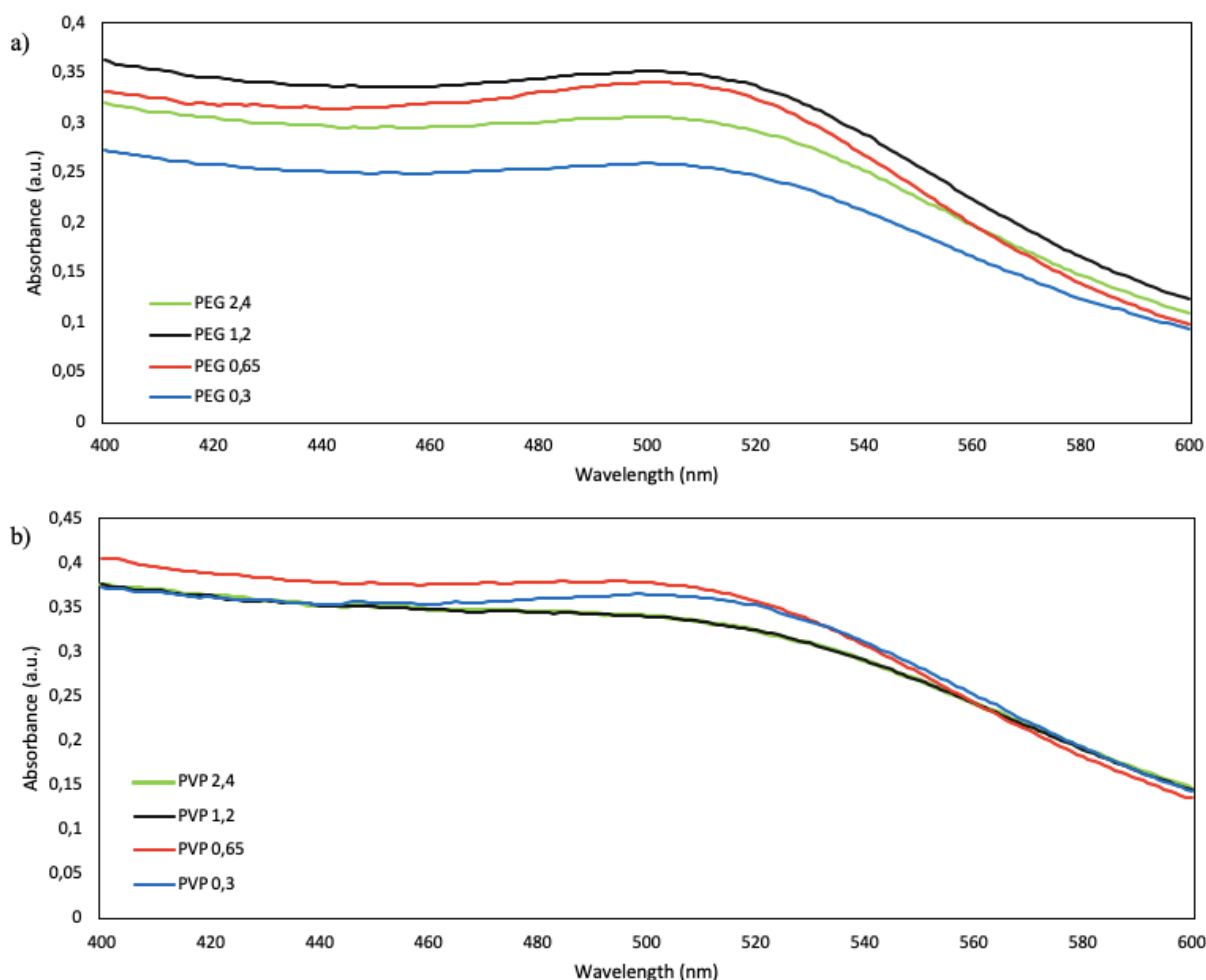
Figure 35 - a) UV-Vis spectra of gold colloids at 25 minutes after addition of NABH$_4$ at different ratios of PEG; b) UV-Vis spectra of gold colloids at 25 minutes after addition of NABH$_4$ at different ratios of PVP.

PEG-stabilized Au colloids show a defined UV-vis peak around 500 nm. PVP-sabilized Au colloids have generally broader UV-vis peaks, except for the spectrum corresponding to the sample PVP0,3. The UV-vis spectra of samples PVP1,2 and PVP2,4 are overlapping, suggesting that the preformed Au colloidal nanoparticles have similar dimensions. It can be further deduced that at an Au:PVP weight ratio of 1,2 the nanoparticle environment reached a maximum in PVP concentration and doubling the PVP to 2,4 does not produce any significant size effect on the preformed Au nanoparticle. Table 10 lists the peak wavelengths.

Table 10 reports the difference between the final UV-vis peak at 25 minutes and the initial UV-vis peak at 3 minutes for the two sets. A positive difference means a red shift while a negative difference a blue shift. For both sets, a blue shift of moderate entity happens for the four samples at 2,4 and 1,2 stabilizer to Au weight ratio. PEG0,65 shows a red shift of 8 nm, the largest shift measured; a minor shift occurs also for the sample PVP0,65. The two samples at the lowest stabilizer:gold weight ratio, PEG0,3 and PVP0,3, do not undergo a significant shift in their SPR peak.
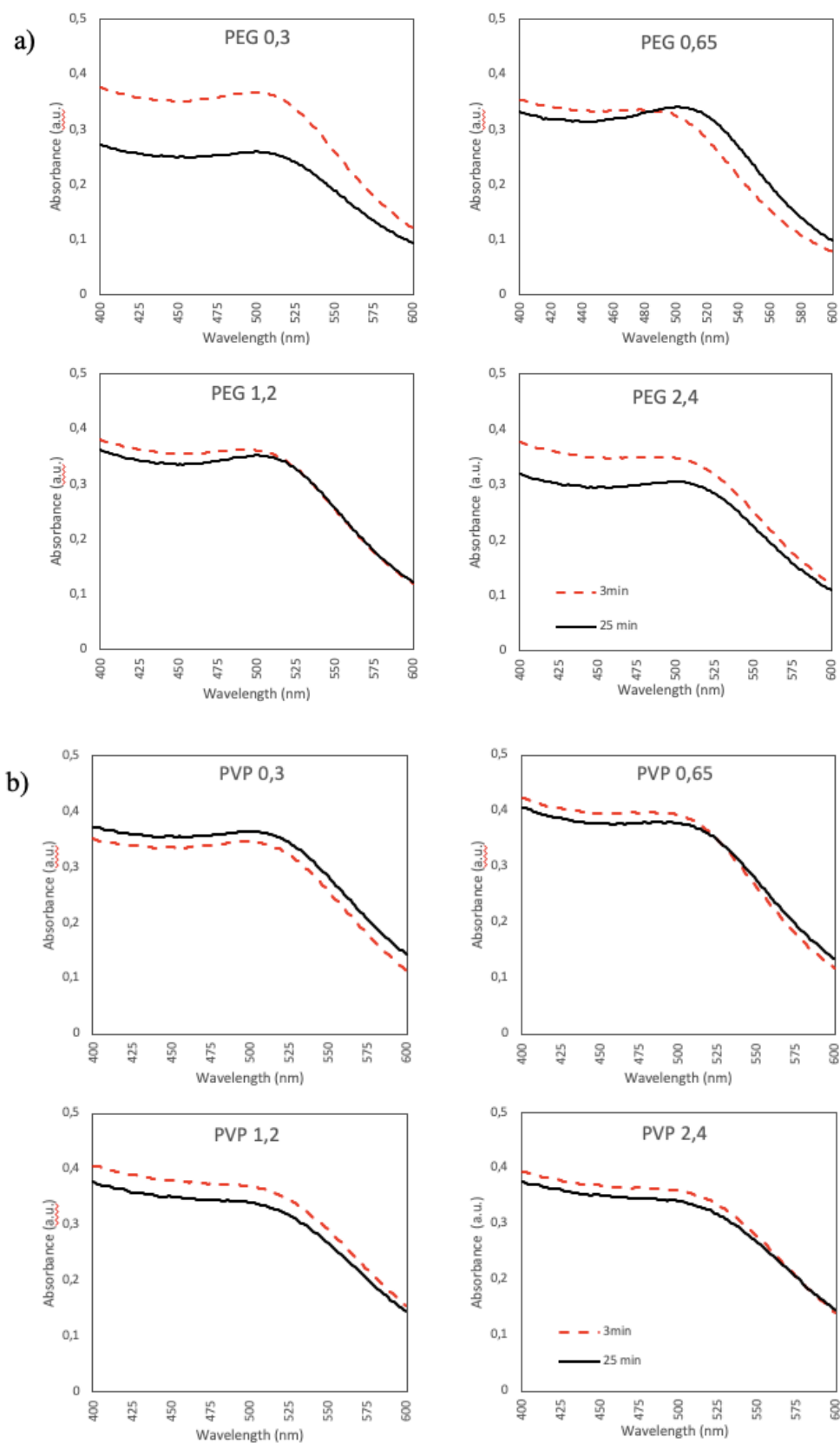
Figure 36 -UV-Vis spectra of gold nanoparticles stabilised with PEG (a) or PVP (b) in different Au:stabiliser ratios. Red dashed line: spectrum after 3 minutes from addition of reducing agent. Black line: spectrum after 25 minutes from addition of reducing agent.

Nanoparticle formation and growth was followed for all the series of samples. Figure 36 shows the UV-vis spectra of the two sets of Au colloids after 3 and 25 minutes from the addition of NaBH$_4$.

Regarding the PEG series, at a glance there is no major shift from 3 to 25 minutes for the samples PEG2,4, PEG1,2 and PEG0,3. Sample PEG2,4 has an initial UV-vis peak at 506 nm that shifts negatively to 501 nm after 25 minutes. Similarly, PEG1,2 UV-vis peak at t=3 minutes is located at 508 nm and shifts to 502 nm. Instead, PEG0,3 shows no shift at all: the peak position at t=3minutes and ant t=25 minutes remains at 503 nm. An exception is represented by the sample PEG0,65, where it is possible to see that the initial peak is found at a lower position compared to the other samples (at 495 nm) and in the spectrum recorded at 25 minutes there is a shift of 8 nm to higher wavelengths, to 503 nm. For the PVP series a similar trend is noticed, with the sample PVP 0,65 showing a red shift (from 496 to 500 nm) albeit to a lower extent that the PEG counterpart. The Au colloidal solution with a PVP:Au weight ratio of 0,3 shows a UV-vis peak at a lower wavelength than PEG0,3 sample, respectively at 498 and 503 nm, nevertheless also in this case the peak position is not shifted at t=25 minutes. Samples PVP1,2 and PVP2,4 start from 502 nm and 503 nm respectively at t=3 minutes; at t=25 minutes both samples have their SPR peak at 497 nm, with a negative shift of -5 nm for PVP 1,2 and -6 nm for PVP 2,4.

colloidal solutions with PVP			
PVP:Au ratio	λ_{max} **at 3 minutes (nm)**	λ_{max} **at 25 minutes (nm)**	$\Delta\lambda_{max}$ **(nm)**
0,3:1	498	498	0
0,65:1	496	500	4
1,2:1	502	497	-5
2,4:1	503	497	-6
colloidal solutions with PEG			
PEG:Au ratio	λ_{max} **at 3 minutes (nm)**	λ_{max} **at 25 minutes (nm)**	$\Delta\lambda_{max}$ **(nm)**
0,3:1	503	503	0
0,65:1	495	503	8
1,2:1	508	502	-6
2,4:1	506	501	-5

Table 10 - SPR peak values from UV-vis spectra are reported. For the same colloidal solution, the first spectrum was recorded after 3 minutes from the addition of NaBH₄, while the second one after 25 minutes. The shift was calculated from the difference between the peak at 25 minutes to which is subtracted the peak wavelength at 3 minutes.

The interpretation of Au SPR peaks is complicated because the signal obtained is weak and particularly broad. Nevertheless, these results indicate that the synthesised nanoparticles are in a similar particle size range since the values of the plasmon peak positions obtained from the UV-vis

analysis are in a similar range from 496-503 nm. Further characterisation by means of XRD and TEM is needed to conclude the exact effect on the gold nanoparticle size and particle size distribution.

4.1.2. DLS

The stability of three collidal Au nanoparticle solutions, stabilized by different polymers (PEG, PVP, and PVA) at the same polymer:Au weight ratio of 0,65, was investigated over a period of 5 days by periodically analyzing the Au nanoparticles size by DLS analysis. Each solution was analysed at five intervals of time from the addition of $NaBH_4$ to the gold precursor solution: 30 min, 1h 30 min, 24 h, 48 h, 5 days.

Colloidal solution	Au PEG 0,65	Au PVP 0,65	Au PVA 0,65
Time	$d_{average}$ (nm)	$d_{average}$ (nm)	$d_{average}$ (nm)
30 min	5,6	5,6	5,6
1h 30 min	6,5	5,6	4,8
24 h	6,5	6,5	4,2
48 h	6,5	6,5	4,2
5 days	6,5	3,1	4,2

Table 11– Au nanoparticle average diameter obtained by DLS analysis of Au colloidal solutions stabilized by PEG, PVP or PVA at stabilizer:Au weight ratio of 0,65 at different intervals of time from $NaBH_4$ addition to gold precursor solution.

After 30 minutes from the addition of $NaBH_4$, the three Au colloidal solutions show the same average nanoparticle size of 5,6 nm. The size of the PEG-stabilised Au colloidal nanoparticles is recorded to increase after 1h 30 min to 6,5 nm. Subsequently no further size changes are recorded for Au PEG 0,65: nanoparticle growth has concluded, and the Au colloidal solution is stable.

It is important to keep in mind that DLS analysis measures the hydrodynamic radius of the nanoparticles, which is influenced by the presence of stabilisers surrounding the metal nanoparticle or aggregates of nanoparticles, therefore the accuracy and overestimation of nanoparticle size is possible.

Au PVP 0,65 nanoparticle size increases 6,5 nm after 24h, then a sharp decrease to 3,1 nm is recorded after 5 days. This fall in nanoparticle size could be attributed to the separation of nanoparticle aggregates. PVA-stabilised Au nanoparticles show a decrease in size after 1h 30 (to 4,8 nm) and after 24h (to 4,2 nm), after which the size remains constant up to the 5 days analysis. This trend could be attributed to a gradual thinning of the PVA shell surrounding the Au nanoparticle. Further investigation by TEM imaging is needed to confirm these hypotheses.

4.1.3. XRD

XRD analysis was carried out on the samples after the immobilisation step and thermal treatment of the supported nanoparticles. Metallic gold has an FCC crystalline structure. The (111) Au plane being dense in atoms compared to other planes (figure 37) gives intense diffraction peaks, with the stronger diffraction peak at 38,2° 2θ value.

Activated carbon (figure 40) and High Area TiO$_2$ (figure 41) diffractograms were recorded to check for overlapping peaks at the 2θ of interest, which is 38,2° 2θ. It can be seen that AC doesn't present any diffraction peak in the area from 37° 2θ and 39° 2θ. This is not the case for TiO$_2$: a diffraction peak is evident in the area from 36° 2θ and 40° 2θ. Hence, in the case of TiO$_2$, Au diffraction peak at 38,2° 2θ overlaps with the support's diffraction peak. Another Au diffraction peak could be used in this case but as the metal loading is very low, no other peak is sufficiently intense for the purposes intended with this analysis.

Accordingly, XRD patterns of the AC-supported catalyst samples clearly showed a broad peak at 38,2° 2θ (figures 38 and 39). Measuring the width at half height allows to estimate the nanoparticle size through the Scherrer equation, as explained in paragraph 2.3.3. The results for the PEG set and the PVP set are contained in table 12.

Sample	Crystallite size (nm)
Au/AC-PVP2,4	8,1
Au/AC-PVP1,2	8,2
Au/AC-PVP0,65	6,4
Au/AC-PVP 0,3	6,7
Au/AC-PEG 2,4	8,0
Au/AC-PEG 1,2	6,2
Au/AC-PEG 0,65	6,4
Au/AC-PEG 0,3	10,3

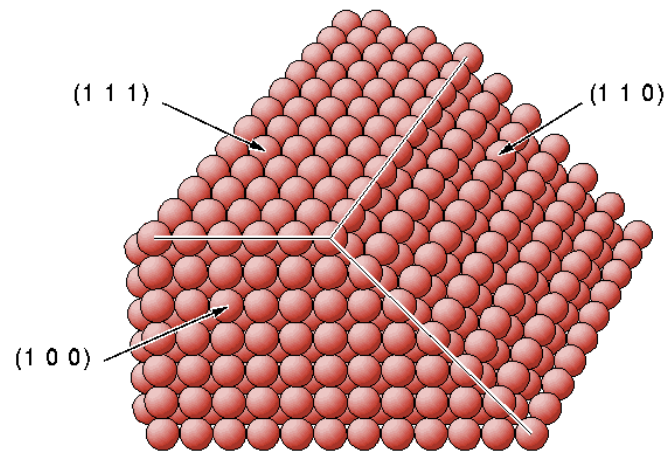Table 12 - Average nanoparticle size calculated with Scherrer equation.

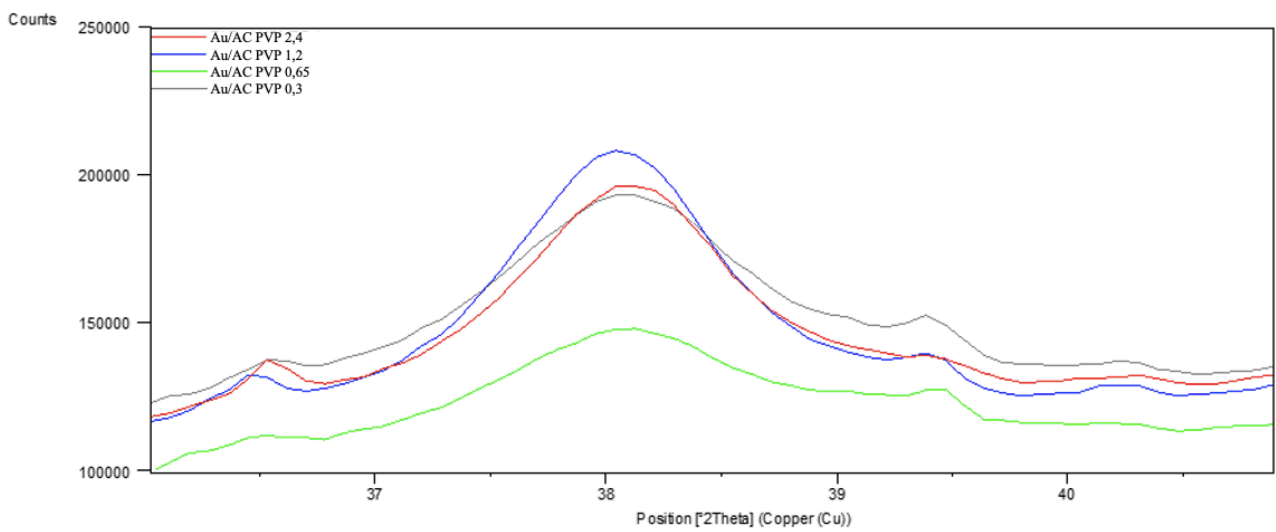Figure 37 – FCC lattice. The crystallographic planes (111), (110), and (100) are highlighted.

Figure 38 – Diffraction pattern of Au/AC PVP series. Red line: Au/AC PVP 2,4; blue line: Au/AC PVP 1,2; green line: Au/AC PVP 0,65; gray line: Au/AC PVP 0,3.
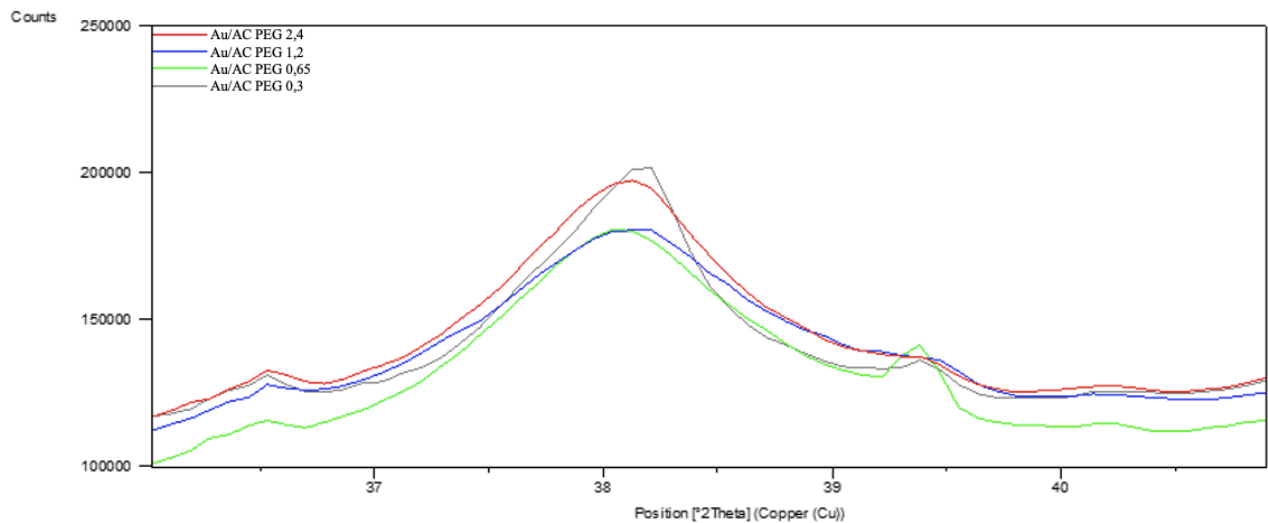

Figure 39 – Diffraction pattern of Au/AC PEG series. Red line: Au/AC PEG 2,4; blue line: Au/AC PEG 1,2; green line: Au/AC PEG 0,65; gray line: Au/AC PEG 0,3.
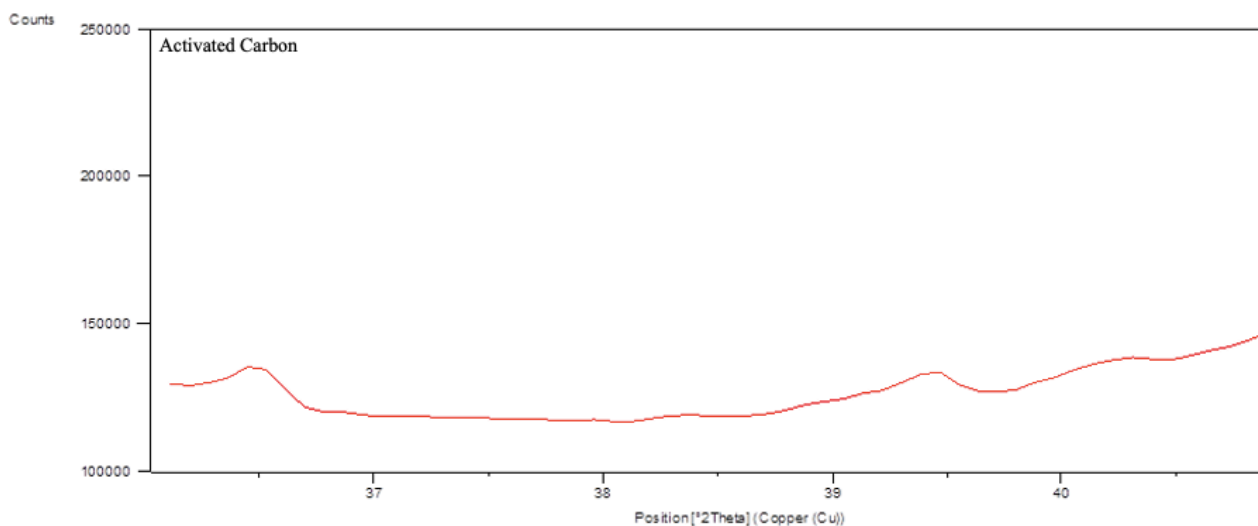
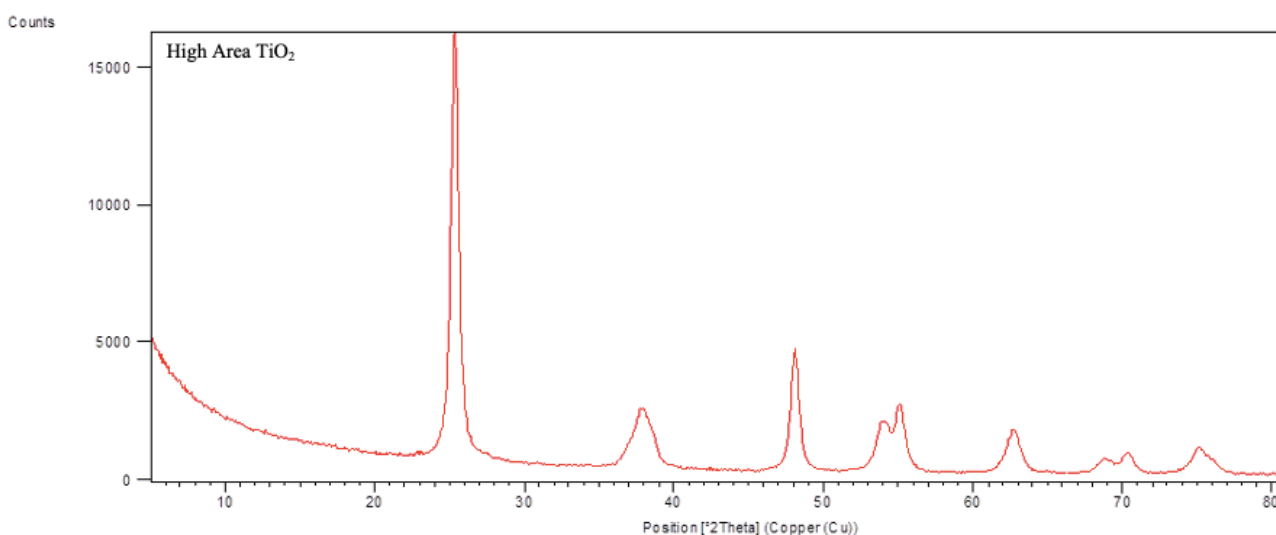Figure 40– Diffraction pattern of naked activated carbon.

Figure 41 – Diffraction pattern of commercial TiO_2 powder.

4.1.4. TEM

Au nanoparticles supported on TiO_2 (sample Au/TiO_2-PVA0,65) were characterized by TEM analysis. Over 400 nanoparticles were included in the analysis to get the nanoparticle size distribution (figure 42). The average Au nanoparticle size was (2,3±1,0) nm. TEM and HAADF-STEM images are shown in figure 43. In HAADF-STEM images the intensity contrast reflects the differences in atomic number (Z-contrast), so this feature allows a better distinction of the nanoparticle from the support, especially in cases such as this one where the nanoparticles are made out of an element with a high Z number (Au, Z=79) compared to the support, where we can find Ti (Z=22) and O (Z=8). The Au nanoparticles appear to be well dispersed on the support without noticeable agglomeration, although the sample is not exempt from formation of few larger nanoparticles.
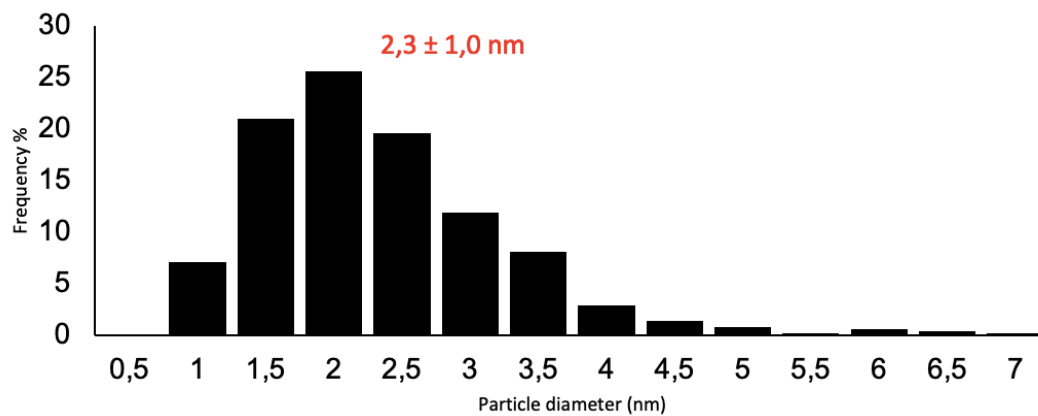
Figure 42 – Mean particle size and particle size distribution of Au/TiO$_2$-PVA0,65.
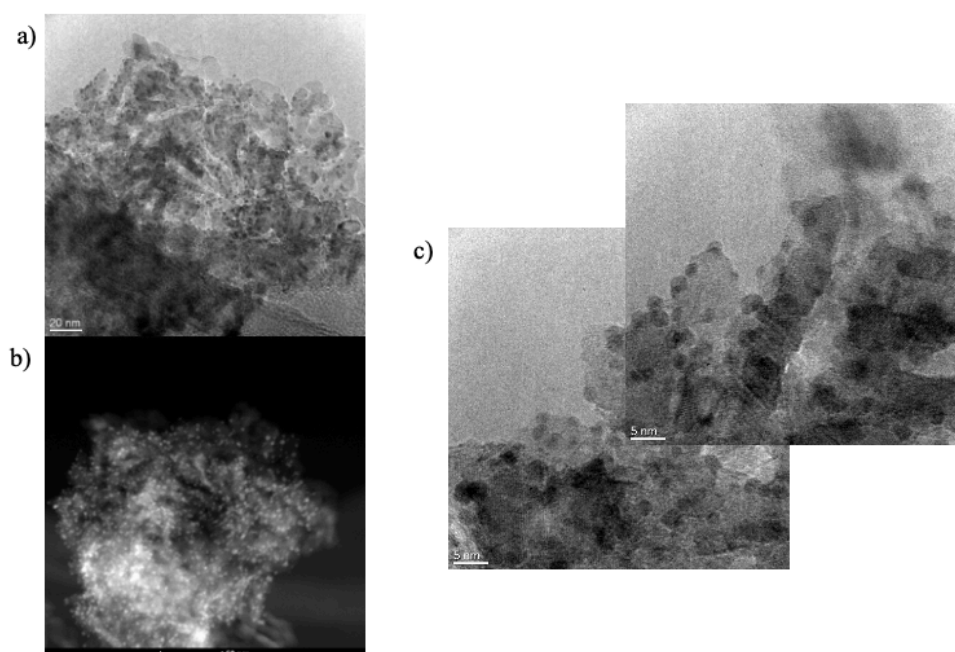

Figure 43 – Typical TEM (a) and HAADF-STEM (b) images of Au/TiO$_2$-PVA0,65, and a magnification (c) of the TEM image.

4.2. Glucose oxidation

4.2.1. Screening of catalysts

The catalysts synthesized as described in section 2.1.2. and listed in table 9 were tested for glucose oxidation to glucaric acid. The reaction conditions were optimised in a previous work [97] with the aim of maximizing glucaric acid yield and selectivity and are summarized in table 13.

Glucose:Au	1000:1
Glucose:NaOH	1:3
Glucose concentration	5% w
Water (solvent) volume	15 mL
Stirring rate	1000 rpm
Temperature	60˚C
O_2 pressure	10 bar
Reaction time	1h

Table 13 – Optimized reaction conditions used for catalyst screening

Both PEG and PVP Au/AC sets were tested and compared with previously obtained results of PVA Au/AC set and of Au/AC with no stabilizer. Catalyst performances in terms of conversion, yield and selectivity are listed in table 14.

Au/AC sample	Particle size (nm)	Glucose conversion %	Gluconic acid yield %	Glucaric acid yield %	Gluconic acid selectivity %	Glucaric acid selectivity %	Others yield %
PVP0,3	6,7	92,4	42,0	19,9	45,5	21,5	32,1
PVP0,65	6,4	88,3	34,8	20,5	39,4	23,3	33,0
PVP1,2	8,2	92,6	51,7	15,8	55,9	17,1	24,6
PVP 2,4	8,1	92,9	51,4	16,2	55,4	17,4	21,0
PEG0,3	10,3	86,6	77,2	4,2	89,1	4,8	6,0
PEG0,65	6,4	95,4	34,3	20,0	36,0	21,0	45,3
PEG1,2	6,2	89,7	80,5	1,6	89,8	1,8	10,8
PEG2,4	8,0	87,5	78,7	2,7	90,0	3,1	9,1
PVA0,3	3,6	90,2	36,4	21,9	24,3	29,3	40,4
PVA0,65	3,1	91,2	37,0	22,4	40,5	24,6	29,2
PVA1,2	2,6	91,1	38,7	19,8	42,5	21,7	27,1
PVA2,4	2,2	90,2	43,8	17,5	48,6	19,4	24,6
PVA0	6,4	91,5	37,9	22,1	24,2	27,7	41,4

Table 14 – Performance of PVP and PVP Au/AC sets. PVA Au/AC set and no-stabilizer Au/AC (Au/AC-PVA0) are also included for comparison purposes.

From the XRD characterization of the samples we know how the stabilizer:Au weight ratio affects the nanoparticle size and hence should also affect catalytic activity to a certain extent. For the two sets, at one hour of reaction, glucose conversion ranges from ~87% to ~95%.

For the PVP set, glucose conversion and gluconic acid yield increase as the PVP:Au weight ratio increases, while for glucaric acid the trend is opposite. For this set, particle size and PVP concentration appear to have an effect on glucaric acid yield: smaller nanoparticles and lower PVP ratio are both beneficial.
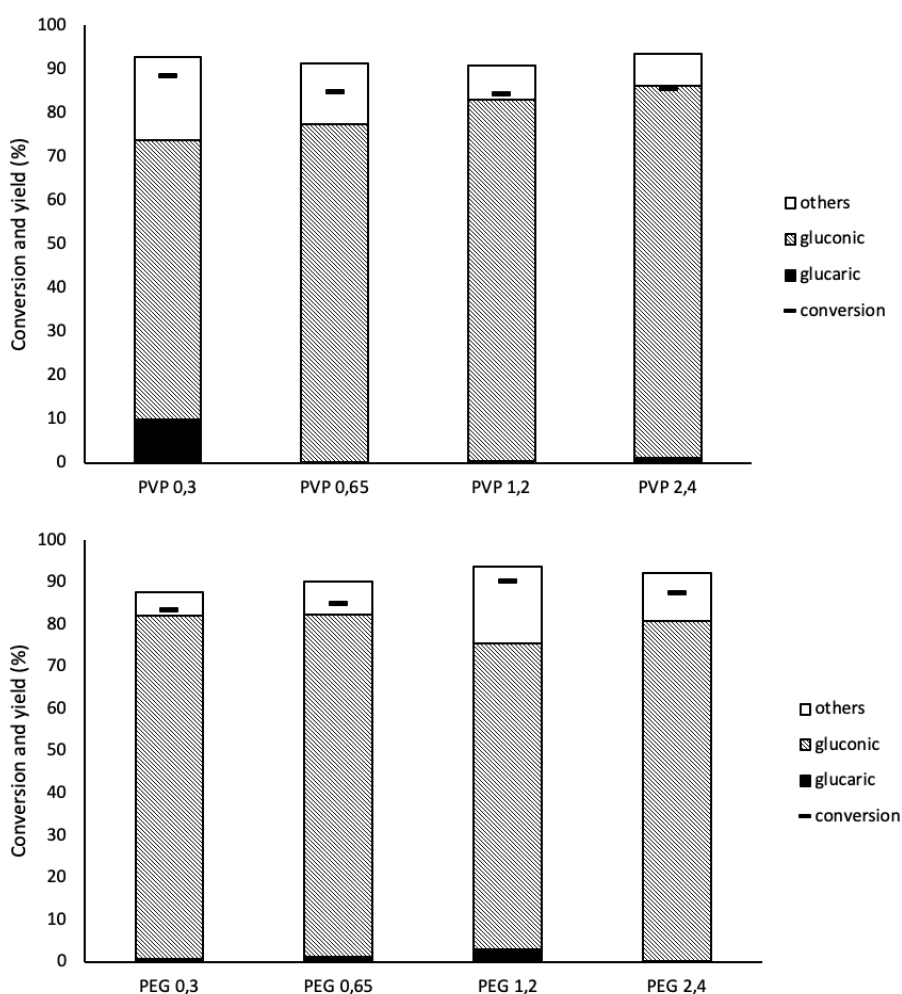

Figure 44 – a) PVP Au/AC set and b) PEG Au/AC set catalytic performances at a reaction time of 15 minutes.

Regarding the PEG series, a higher nanoparticle size results in a lower glucose conversion, but on a higher gluconic acid yield. Glucaric acid yield is extremely low except for Au/AC-PEG0,65, which exceeds the threshold of 4% reaching an exceptional 20%. Particle size seems less influent than PEG ratio for this set, as Au/AC-PEG0,65 and Au/AC-PEG 1,2 samples show similar dimensions. It seems that the presence of PEG is not facilitating the further transformation of gluconic acid to glucaric acid, implying that the interaction of PEG with the active sites of Au and metal-interface responsible for the transformation of gluconic acid to glucaric acid have been affected by blocking and covering the

desired sites. However, this is a hypothesis and at this moment we can not prove it, without further *in situ* and *ex situ* characterization.

In order to examine the initial rates, the catalysts were tested at a shorter reaction time of 15 minutes. At short reaction time, glucose conversion is >80% for all the samples. The major product is gluconic acid. As the PVP ratio increases the initial rate decreases clearly for the side products. Glucaric acid yield at 15 minutes is extremely low except for Au/AC-PVP 0,3. This confirms the important effect of PVP concentration. PVP can bind and adsorb on specific sites on the Au nanoparticle affecting the catalytic activity and formation of products. It seems that a higher weight ratio of PVP:Au diminishes the yield to glucaric acid.

PEG set is more difficult to analyse. Albeit a high glucose conversion, initial reaction rate for glucaric acid is very low for the whole set. With a comparison of glucaric acid yield at 15 minutes and at 1 hour reaction time, it seems that active sites are blocked and that the reaction cannot proceed to the second stage, which leads to formation of the target product. In the case of PEG, the stabilizer concentration has a higher influence on reactivity than nanoparticle size, confirming previous observations.

4.2.2. Effect of support

It is known from early work on Au nanoparticles that the support has an important effect on catalytic performance of supported Au nanoparticles[2]. In this work we compared the catalytic performance of activated carbon and TiO_2 as supports for preformed Au nanoparticles sythesised in the same conditions by using PVA as stabilizer at a polymer:Au weigth ratio of 0,65. The reaction experimental conditions used are one optimized in previous work by Soto et al. reported in the experimental section in paragraph 2.1.5.

Comparing the supports at the same reaction time, it is possible to observe a significant difference in glucaric acid and by-products yield. First of all, at 15 minutes reaction time isomers yield reaches 10,3% for Au/TiO_2 while isomers are not detected for Au/AC. At a reaction time of 1 hour, isomers yield is again higher for TiO_2-supported Au nanoparticles than for AC-supported Au nanoparticles (7,7% and 1,1% respectively). Glucaric acid yield at 15 minutes reaction time is extremely low for Au/TiO_2 (0,7%) while Au/AC achieved a 12,0 % yield. Similarly, after 1 h glucaric acid yield reached 12,7% with Au/TiO_2 and 22,4% with Au/AC.

Since the reaction leading to isomer formation competes with the adsorption of glucose on the active sites, a higher yield in isomers is owed to less available active sites for glucose oxidation on Au/TiO_2, confirmed by a lower yield in glucaric acid compared to the Au/AC counterpart.
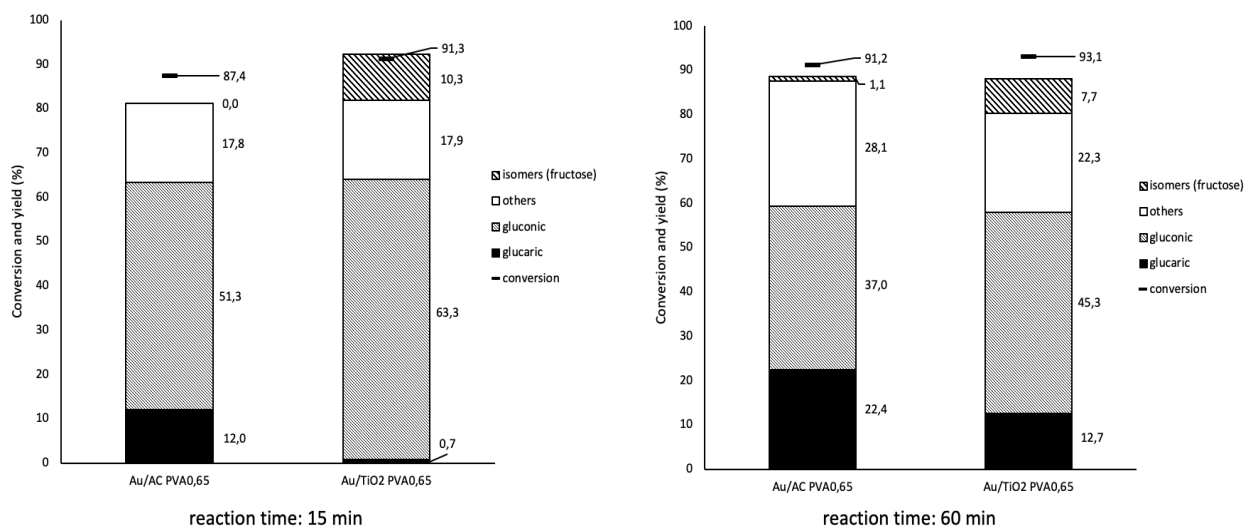
Figure 45– Glucose conversion and product yield at a reaction time of 15 and 60 minutes for catalysts Au/AC PVA0,65 and Au/TiO$_2$ PVA0,65. Reaction conditions: 60°C, 1000 rpm, 10 bar O$_2$, Glu:Au:NaOH molar ratio of 1000:1:3000

The higher catalytic activity of Au/AC could be attributed to a better distribution of the AC-supported Au nanoparticles, owed to the high surface area of activated carbon compared to titanium oxide (SA$_{AC}$ =1049 m^2/g; SA$_{TiO2}$ = 125 m^2/g). With a better dispersion of the nanoparticles, a higher number of active sites are available and hence a better catalytic activity is achieved[98].

Another effect that influence catalytic activity is the interaction between Au nanoparticles and the support, depending on the semiconducting or insulating properties of the support. In a study by McEntee and co-workers[99] it was proved that charge transfer in TiO$_2$ supported Au nanoparticles was strongly influenced by the chemical environment: molecules with donor (acceptor) electronic properties physisorbed on the support induce a partial negative (positive) charge on the supported Au nanoparticles. This kind of behavior was not observed in Au/SiO$_2$, where SiO$_2$ is an insulator, whereas TiO$_2$ is a semiconductor. Activated carbon is not known for its charge transfer properties with Au nanoparticles[21], so the different interaction of Au nanoparticles with AC and TiO$_2$ can have an influence on catalytic activity for glucose oxidation to glucaric acid.

Further studies as TEM imaging and XPS analysis are required to elucidate the presence of these effects on the materials studied.

4.2.3. Reproducibility

To verify the reproducibility of the results obtained, a reaction with the same experimental conditions was carried out three times in different days and using the same batch of catalyst. This allows to check if the operator's execution of the experimental tests gives consistent and comparable results over time. Glucose conversion has an average value of (84,8±0,4)% and gluconic acid yield (83,4±0,7)%.
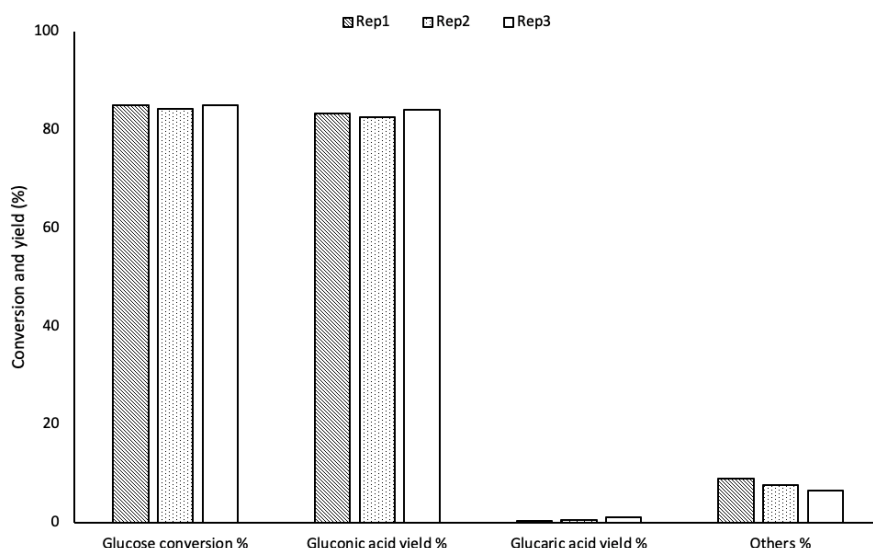
Figure 46 – Reproducibility test on catalyst Au/AC-PVP1,2 at reaction time of 15 minutes. Three repetitions were carried out.

4.3. Nitrophenol reduction

4.3.1. Effect of support: substrate adsorption

Since activated carbon has a very high surface area (SA_{BET} = 1049 m^2/g), we expected it to adsorb part of the nitrophenol in solution[100,101]. To understand the appropriate catalyst concentration and reaction conditions to be used for catalysts activity determination, we measured the optical spectrum of 4-nitrophenol 1,0x10^{-4} M with different amounts of catalyst and different experimental conditions and protocols. The methods used were exactly as described in the experimental section.

Test	AC (mg/L)	Method	Stirring	Adsorption
1	320	Round-bottom flask	Yes, ~1000 rpm	>90%
2	80	Round-bottom flask	Yes, ~1000 rpm	40%
3	80	Cuvette	No	25%

Table 15 - Conditions for the adsorption tests. [4-NP] = 1,0x10^{-4} M, [NaBH$_4$] = 4,5x10^{-3} M, V= 50 mL. Test 1 and 2 were carried out using round-bottom flask setup; for test 3, cuvette setup.

Generally, for this reaction the optimal substrate to metal molar ratio to explore the catalytic activity is in a range of 2 to 6[102]. To make sure we could notice a difference in catalytic activity caused by stabilisers we decided to start from the highest ratio, 6, since a higher substrate:metal molar ratio results in a lower reaction rate. Using the round-bottom flask setup, the resulting amount of carbon (320 mg/L) proved to be enough to remove alone up to 90% of the nitrophenol in solution (test 1,

70

table 15). Even reducing the amount of carbon to a quarter of the initial quantity (80 mg/L), physical adsorption of nitrophenol is still consistent (test 2, table 15). In test 3, the concentration of 80 mg/L without stirring proved to limit the physical adsorption to 25%.

Figure 47 depicts the nitrophenol adsorption by active carbon as a function of time, where:

$$(1) \qquad \text{4-NP adsorption} = (C_0 - C_t)/C_0$$

Where C_0 is the initial 4-NP concentration and C_t is 4-NP concentration at the time which the UV-vis spectrum was recorded.
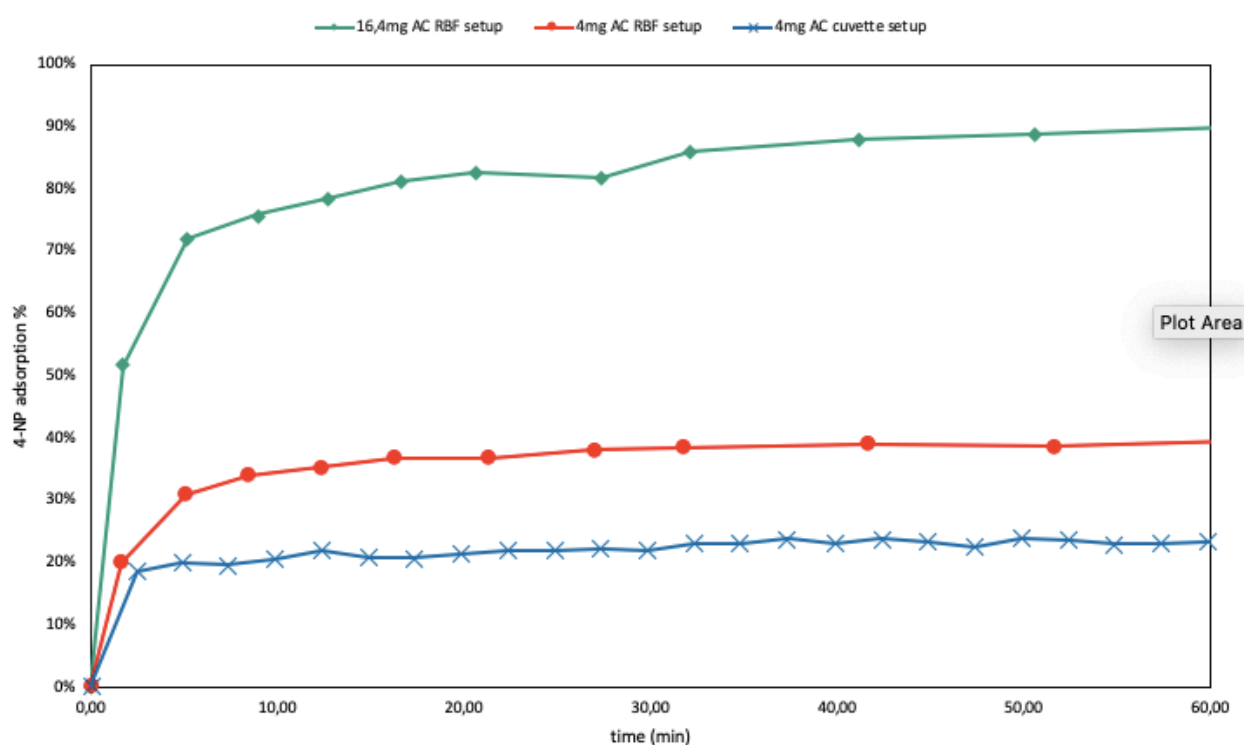

Figure 47 – Adsorption of nitrophenol by active carbon under conditions of test 1, test 2 and test 3. Adsorption is calculated from experimental measurements as $(C_0 - C_t)/C_0$ and expressed as a percentage.

4.3.2. Optimization of reaction setup

The adsorption tests in section 4.3.1. highlight the influence of set-up conditions. It had been pointed out in a previous paragraph on ozonation that in order to identify catalytic activity, removal of substrate by physical adsorption by the support must be taken into account. The three setups identified in table 15 were tested for the possibility to distinguish catalytic activity of the supported Au nanoparticles from the simple adsorption and to analyse the effect of preparation procedure on their activity.

The tests were executed using the series of catalysts prepared with PEG as the chosen stabiliser (AC-PEG set). The first reaction experimental setup that was tested corresponds to "test 1" in table 15. Each catalyst was used in a concentration of 320 mg/L in 50 mL of a water solution containing 4-

nitrophenol at a concentration of $1,0\times10^{-4}$ M and $NaBH_4$ at a concentration of $4,5\times10^{-3}$ M prepared as described in section 2.1.3. Reaction progression was monitored by UV-vis spectrometry using the absorbance at 400 nm (corresponding to 4-NP characteristic UV-vis peak) to determine 4-NP concentration at the time of the analysis. 4-nitrophenol conversion was obtained with the formula

$$(2) \qquad X\% = (C_0 - C_t)/C_0$$

Where C_0 is the initial 4-NP concentration and C_t is 4-NP concentration at the time which the UV-vis spectrum was recorded.

As-obtained X% was plotted as a function of time as shown in figure 48, where the resulting curves from the reaction with each sample form the set Au/AC PEG are shown for comparison. Changes in 4-NP concentration by activated carbon (AC) over time can be included because reaction conversion and 4-nitrophenol adsorption are calculated with an equivalent mathematical formula:

$$(3) \qquad \text{4-NP adsorption} = (C_0 - C_t)/C_0 = X\%$$

From figure 48 we can see that 4-nitrophenol disappears from the solution both for adsorption on the support and from catalytic activity. The curves obtained from the catalytic tests show a progression similar to plain AC for the initial part, although they don't strictly overlap: this can be interpreted in terms of an altered adsorption capacity of the catalysts compared to naked AC due to the presence of the pre-formed nanoparticles and the stabilising agent. The latter in particular could displace from the nanoparticle into the AC's pores decreasing the final surface area, suggested also by the fact that the sample with the highest PEG:Au weight ratio is the one that shows the most evident reduction in adsorption capacity. In order to confirm that, total surface area of the catalysts could be measured by BET analysis and compare it to AC.

The second part of the curves can be identified when the slope sharply increases, although for just one (Au/AC-PEG0,3, Au/AC-PEG0,65, Au/AC-PEG1,2) or two (Au/AC-PEG2,4) intervals of time. This change can be attributed to catalytic activity, but it has not been reported before so not much information is available on this. It is interesting to note that the slope increase shows up at different times for the various samples: after 10 minutes for Au/AC-PEG0,65, after 13 minutes for Au/AC-PEG2,4, after 16 minutes for Au/AC-PEG1,2, and finally after 20 minutes for Au/AC PEG-0,3. All the supported nanoparticle samples convert 4-nitrophenol to >97% , while AC reaches a plateau at after 80% 4-NP removal. This allows us to confirm that the Au/AC-PEG series shows catalytic activity towards 4-nitrophenol reduction, although this setup is not suitable for quantitative analysis for AC-based catalysts.
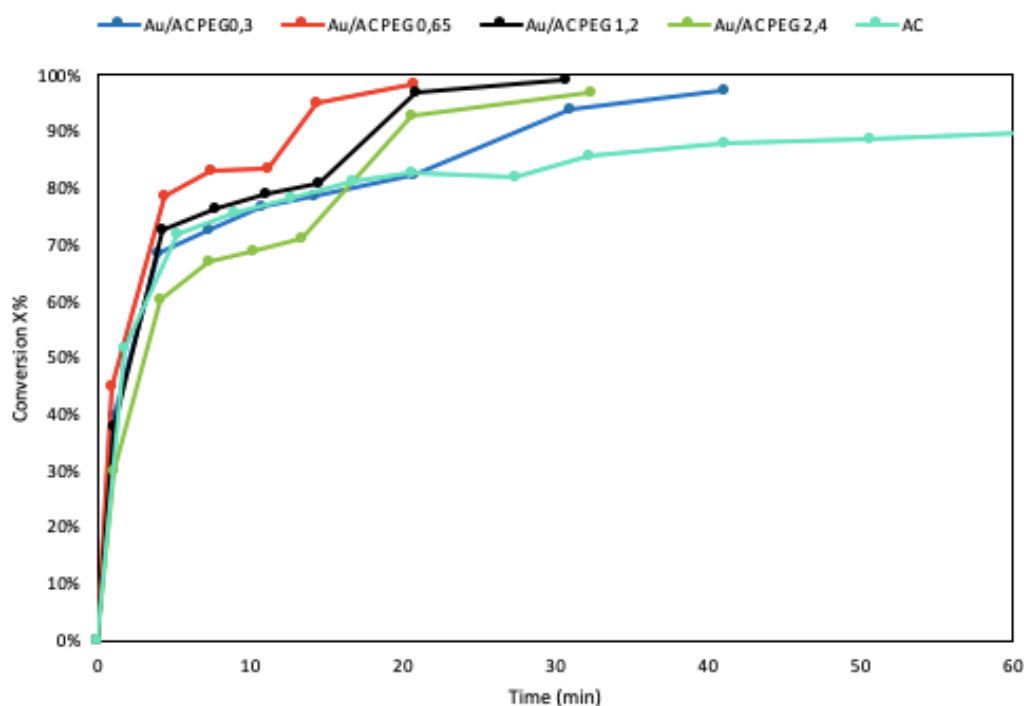
Figure 48 – 4-nitrophenol conversion from catalytic reduction with Au/AC PEG set carried out using the round-bottom flask setup. Reaction conditions: [4-NP] = $1{,}0\times10^{-4}$ M, [NaBH$_4$] = $4{,}5\times10^{-3}$ M, V= 50 mL, [catalyst] = 320 mg/L, stirring = ~1000 rpm.

The second reaction experimental setup tested for Au/AC-PEG set corresponds to "test 2" conditions in table 15. The experiments and data elaboration were carried out as above, though decreasing the catalyst concentration to 80 mg/L. The results are shown in figure 49.

In this case, all the catalysts show a decreased 4-nitrophenol adsorption compared to naked AC at initial times. Hence the effect of surface area decrease is even more evident than in figure 48.

Also, the maximum conversion measured is 66% by Au/AC-PEG0,65 after 60 minutes, but it is not unexpected as the catalyst concentration is ¼ respective to the previous setup. Catalytic activity in this case is clearly distinguishable for samples Au/AC-PEG0,65 and Au/AC-PEG1,2 only, and they both show the slope increase after 30 and 50 minutes respectively. This reaction setup is clearly to discard to test preformed Au nanoparticles supported on AC.

Lastly, the reaction experimental setup that corresponds to "test 3" in table 15 was tested with Au/AC-PEG set.

The reaction conditions used are those described in section 2.1.11 as "cuvette setup", following the method as described there: an aqueous solution with 4-nitrophenol $1{,}0\times10^{-4}$ M, NaBH$_4$ $4{,}5\times10^{-3}$ M, and catalyst at a concentration of 80 mg/L was prepared. Hence, 3,5 mL aliquot of this solution was used for UV-vis analysis. The results are shown in figure 50. -NP removal by AC adsorption is rather low, to begin with: it reaches a plateau at about 20% 4-NP removal after just 2,5 minutes. Catalytic activity of all Au/AC-PEG samples is neatly identifiable and doesn't seem to be negatively affected by AC adsorption of the substrate as was the case for previous tests. Eventually, this reaction

experimental setup seems to be the most appropriate for quantitative analysis of reaction kinetics for the particular reaction using highly adsorbed carbon materials.
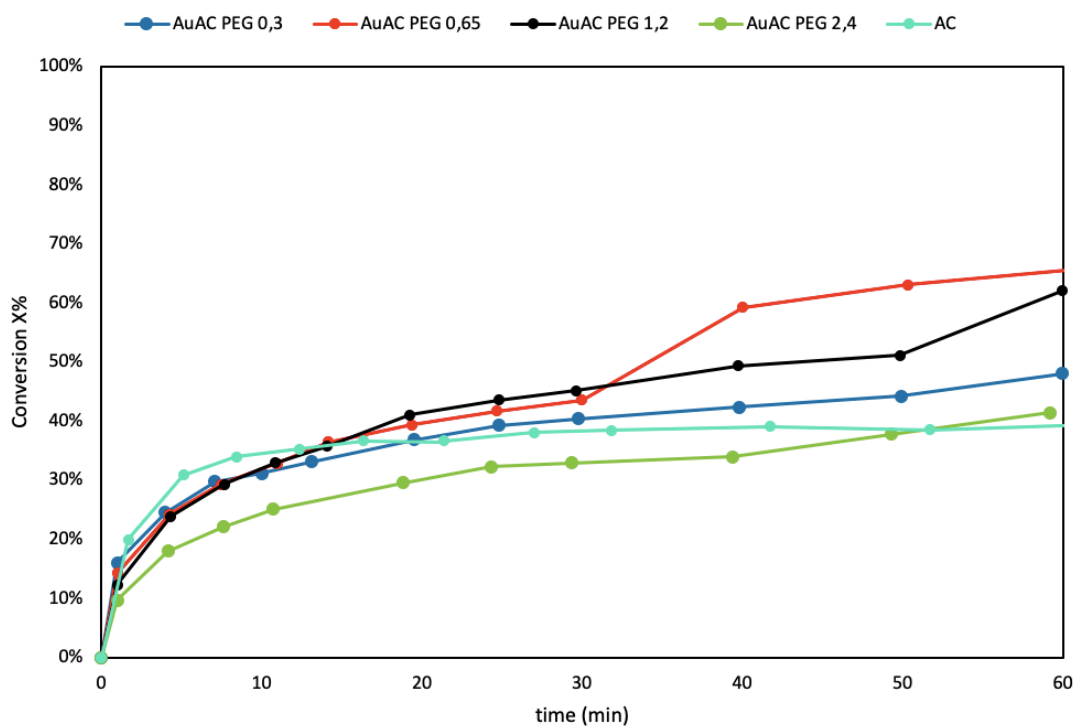

Figure 49 – 4-nitrophenol conversion from catalytic reduction with Au/AC-PEG set carried out using the round-bottom flask setup. Reaction conditions: [4-NP] = $1,0 \times 10^{-4}$ M, [NaBH$_4$] = $4,5 \times 10^{-3}$ M, V= 50 mL, [catalyst] = 80 mg/L, stirring = ~1000 rpm.
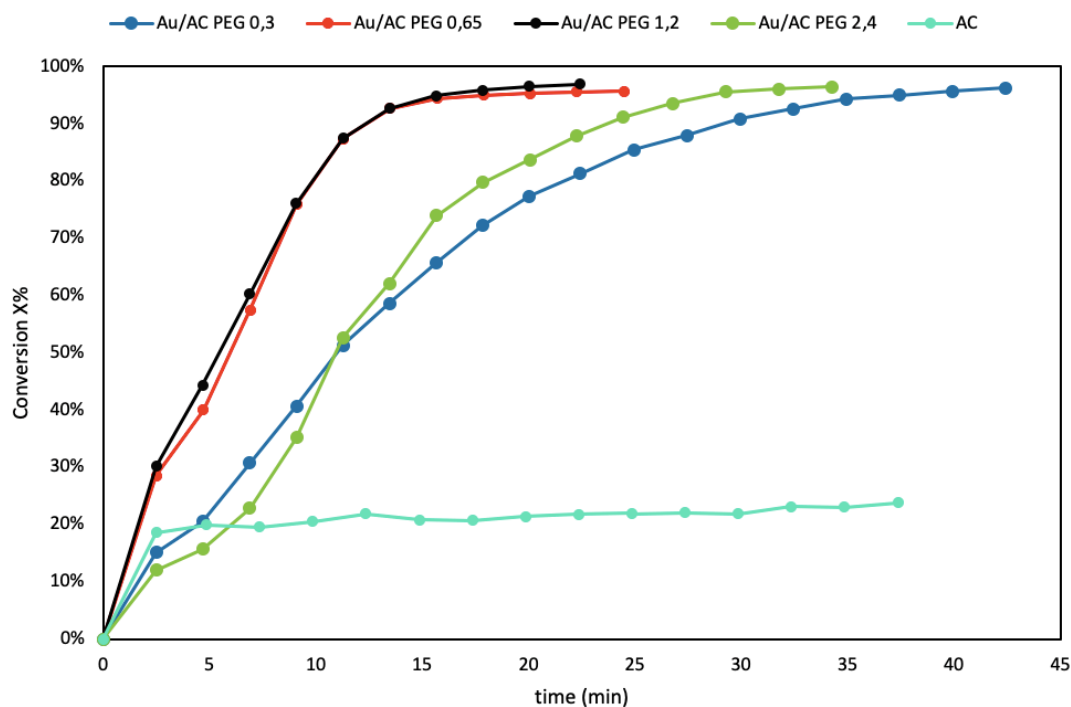

Figure 50 – 4-nitrophenol conversion from catalytic reduction with Au/AC-PEG set carried out using the cuvette setup. Reaction conditions: [4-NP] = $1,0 \times 10^{-4}$ M, [NaBH$_4$] = $4,5 \times 10^{-3}$ M, V= 50 mL, [catalyst] = 80 mg/L, no stirring.

4.3.3. Screening of catalysts

From the tests executed on activated carbon, appropriate set up to screen catalytic activity of the materials was found to be the cuvette setup because it allows to minimize physical adsorption by the support. The reaction was carried out following the same procedure for every sample, to allow comparison of the results. The exact procedure is detailed in the previous chapter, at paragraph 2.1.11. For a catalytic measurement, a number of UV-vis spectra were recorded until 4-nitrophenol peak reached an absorbance below 0,02, point which marks that above 95% of nitrophenol was converted, or up to termination of the method. The absorbance at 400 nm in each spectrum was used to calculate the corresponding 4-nitrophenol concentration with the help of Lambert-Beer law. The molar extinction coefficient was obtained thanks to the calibration and resulted to be $\varepsilon=18100$ Lmol^{-1}cm^{-1}. The spectrometer automatically registers the time of each measurement, to analyse the decrease in 4-nitrophenol concentration as a function of time. Two functions were used for this analysis: conversion and natural logarithm of 4-NP concentration at a given time over the starting concentration. Conversion is given by equation (2):

$$(2) \qquad X\% = (C_0 - C_t) \times 100 / C_0 = (1 - C_t / C_0) \times 100$$

Where X is the conversion and can be expressed as a percentage; C_t is nitrophenol concentration at a given time t; C_0 is nitrophenol initial concentration.

The natural logarithmic function of the concentration ratio comes from the assumption that in presence of large excess of $NaBH_4$, its concentration can be approximated as constant with time hence leaving only the nitrophenol concentration in a pseudo-first order reaction rate[35]:

$$(4) \quad - dC / dt = k_{app} C_{4\text{-NP}}$$

Where $C_{4\text{-NP}}$ is nitrophenol concentration; t represents time; k_{app} represents the apparent kinetic constant; k_{app} contains the sodium borohydride approximated-constant concentration and other parameters that are constant if the reaction conditions are fixed.

After integration of this differential equation using as extremes C_0 and C_t for the C variable and imposing the initial time as t = 0, we obtain:

$$(5) \qquad \ln(C_t / C_0) = -k_{app} t$$

This equation can be interpreted with t as the independent variable and $\ln(C_t / C_0)$ as the dependent variable, - k_{app} represents the slope of the straight line so identified. By plotting the points obtained experimentally in a graph that sees time on the abscissa axis and $\ln(C_t / C_0)$ on the ordinate axis. Interpolating the experimental points with a fitting straight line, the slope of the latter represents the term - k_{app} of the reaction.

In figure 50 the conversion progression over time is reported for the four samples in the Au/AC-PEG set and the 4-nitrophenol removal by adsorption on AC. However, the measured decrease in 4-nitrophenol absorbance is owed not only to catalytic activity of gold nanoparticles but also to adsorption on the surface of the support, activated carbon. Using the total conversion values at a given time, it is possible to obtain the conversion from catalytic reduction by subtraction of the 4-nitrohenol adsorption on AC expressed as conversion as in equation (3). The extrapolated conversion curves are shown in figure 51.

The conversion curves and the extrapolated conversion curves obtained for Au/AC-PVP and Au/AC-PVA sets are in the Supporting Information section (figure S1 and figure S2).
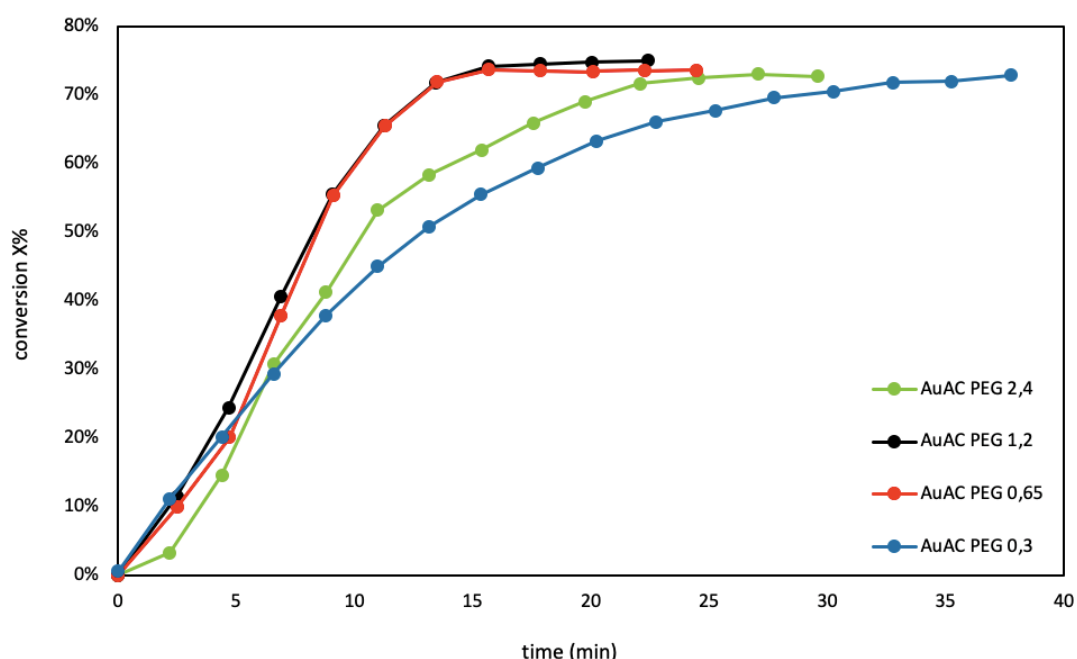

Figure 51 – Extrapolated conversion for Au/AC-PEG set, to highlight the catalytic 4-nitrophenol reduction by supported Au nanoparticles.

From the extrapolated conversion values it is possible to obtain the natural logarithmic function that allows to calculate the apparent kinetic constant for a given catalyst. From equation (2) we can express the ratio C_t/C_0 as function of the extrapolated conversion ($X_{extr}\%$):

$$(6) \qquad C_t/C_0 = 1 - (X_{extr}\% \, / \, 100)$$

Now using the C_t/C_0 as expressed in equation (6) in equation (5) it is possible to plot the graph $\ln(C_t/C_0)$ against time. In figure 52 this procedure was applied to the four curves of pseudo-first order catalytic nitrophenol reduction for the catalyst series og Au/AC-PEG, and by means of the slope of the trendline, obtain the k_{app} values for each catalyst.
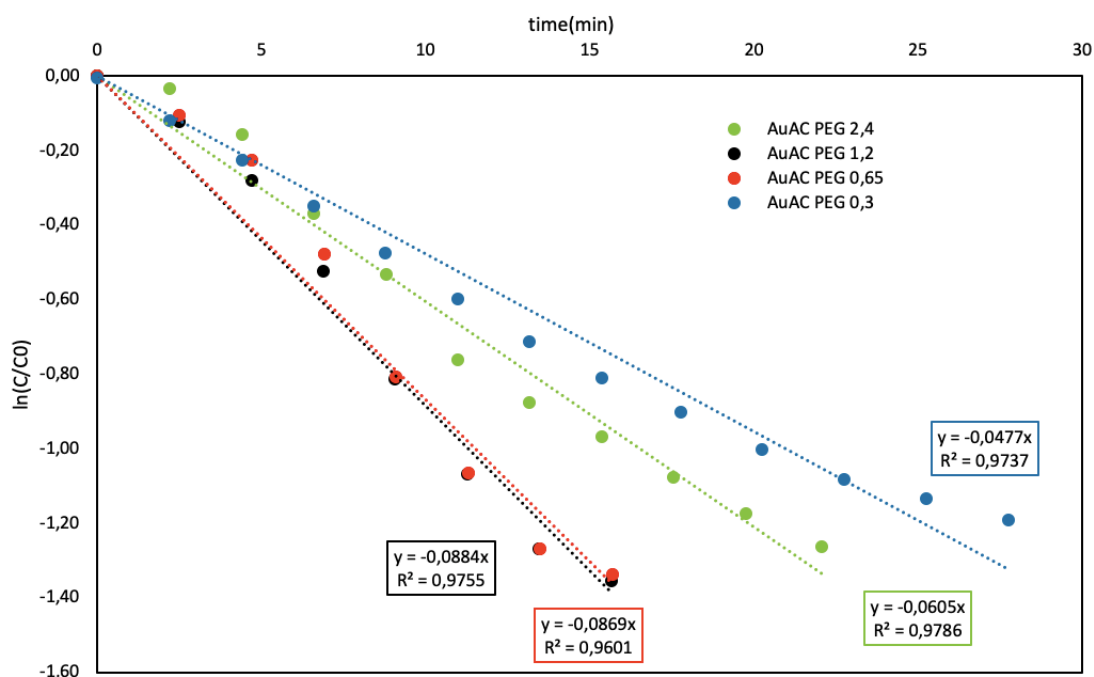
Figure 52 – The pseudo first-order reaction curves for the 4-nitrophenol catalytic reduction by Au/AC PEG set of catalysts; k_{app} values are represented by the slope of the trendlines, for which R^2 values are shown.

All the k_{app} values obtained for all the catalysts tested are grouped in table 16. The pseudo-first order plots for the Au/AC-PVP and Au/AC-PVA sets are in the supporting information section (figure S3).

Sample	k_{app} (min^{-1})	Nanoparticle size (nm)
Au/AC PEG 0,3	0,048	10,3[a]
Au/AC PEG 0,65	0,087	6,4[a]
Au/AC PEG 1,2	0,088	6,2[a]
Au/AC PEG 2,4	0,061	8[a]
Au/AC PVP 0,3	0,078	6,7[a]
Au/AC PVP 0,65	0,049	6,4[a]
Au/AC PVP 1,2	0,028	8,2[a]
Au/AC PVP 2,4	0,011	8,1[a]
Au/AC PVA 0,3	0,036	3,6[a]
Au/AC PVA 0,65	0,037	3,1[a]
Au/AC PVA 1,2	0,039	2,6[a]
Au/AC PVA 2,4	0,059	2,2[a]
Au/AC PVA 0	0,047	6,4[a]
Au/TiO$_2$ PVA 0,65 (80 mg/L)	0,178	2,3[b]

Table 16 – List of the samples with their respective obtained k_{app} and supported Au nanoparticle size. [a] Crystallite average size obtained from XRD patterns by application of Scherrer equation. [b] Average nanoparticle diameter obtained by TEM analysis.

77

4.3.4. Effect of stabiliser:Au weight ratio on nanoparticle size

Nanoparticle size can be influenced by presence of a stabilizer, its nature and its amount relative to metal. Three series of materials consisting in preformed Au nanoparticles stabilized by different polymers (PEG, PVP, and PVA) supported on activated carbon were prepared. For each polymer, Au nanoparticles were synthesised using four different polymer:Au weight ratio values, in order to study the effect of this parameter on nanoparticle size after supporting on AC. Au nanoparticle size for each sample was determined by means of XRD analysis by applying the Scherrer equation to the characteristic Au XRD peak at 38,2° 2θ value, that allows to obtain the Au crystallite average size.
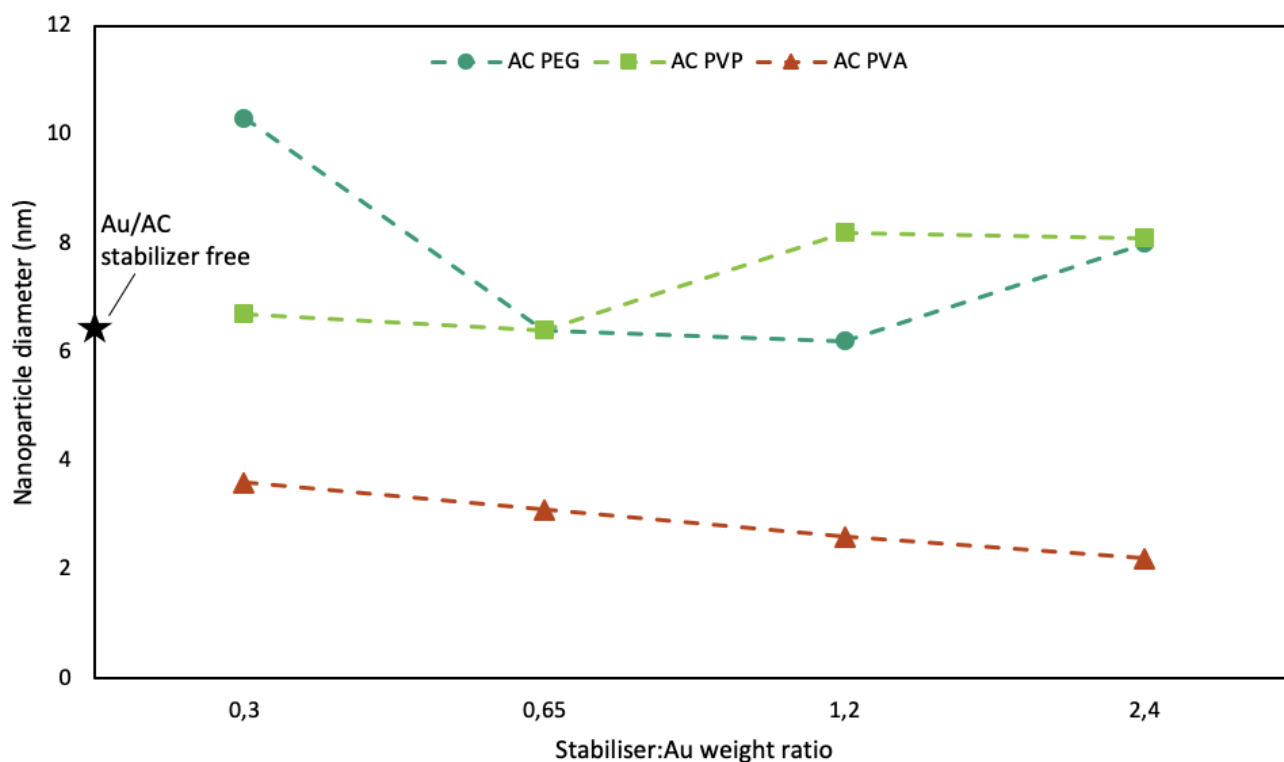

Figure 53 – AC-supported Au nanoparticle average diameter is plotted against stabiliser:Au weight ratio for the three polymers chosen as stabilisers: PEG (blue, round marker), PVP (green squared marker) and PVA (red, triangle marker). The stabiliser-free Au/AC nanoparticle size is identified with star marker.

Regarding series of Au/AC-PVA (prepared using PVA as stabilizer), increasing the PVA:Au weight ratio decreases the nanoparticle size. In sample Au/AC-PVA2,4, the supported Au nanoparticles show a diameter of 2,2 nm, the smallest obtained. The three other PVA samples are 2,6 nm (Au/AC-PVA1,2), 3,1 nm (Au/AC-PVA0,65), and 3,6 nm (Au/AC-PVA0,3). Au/AC-PVP set has an opposite trend: nanoparticle size increases as does PVP:Au weight ratio. In particular Au/AC-PVP0,3~Au/AC-PVP0,65<Au/AC-PVP1,2~Au/AC-PVP2,4 (6,7 nm, 6,4 nm, 8,2 nm, 8,1 nm respectively). Au/AC-PEG set shows yet another behaviour: nanoparticle size reaches a minimum at an intermediate ratio of PEG:Au. From Au/AC-PEG0,3 to Au/AC-PEG0,65 nanoparticle size

decrease from 10,3 nm to 6,4 nm. For Au/AC-PEG1,2 size is 6,2 nm, then increases again for Au/AC-PEG2,4 where nanoparticles are 8,0 nm in diameter.

Overall, the smaller Au nanoparticle size was obtained using PVA as stabilizer. Preformed gold nanoparticles synthesized without any stabilizer supported on AC (Au/AC-PVA0) are of an intermediate diameter: 6,4 nm.

4.3.5. Effect of stabilizer:Au weight ratio on catalytic activity

Catalytic activity of supported Au nanoparticles can be influenced by many factors, including stabiliser presence[103]. For the three catalyst series, prepared with PEG, PVP or PVA as the chosen stabiliser, we plot the obtained catalytic constant against the stabiliser:Au weight ratio to elucidate the effect of this parameter on catalytic activity.
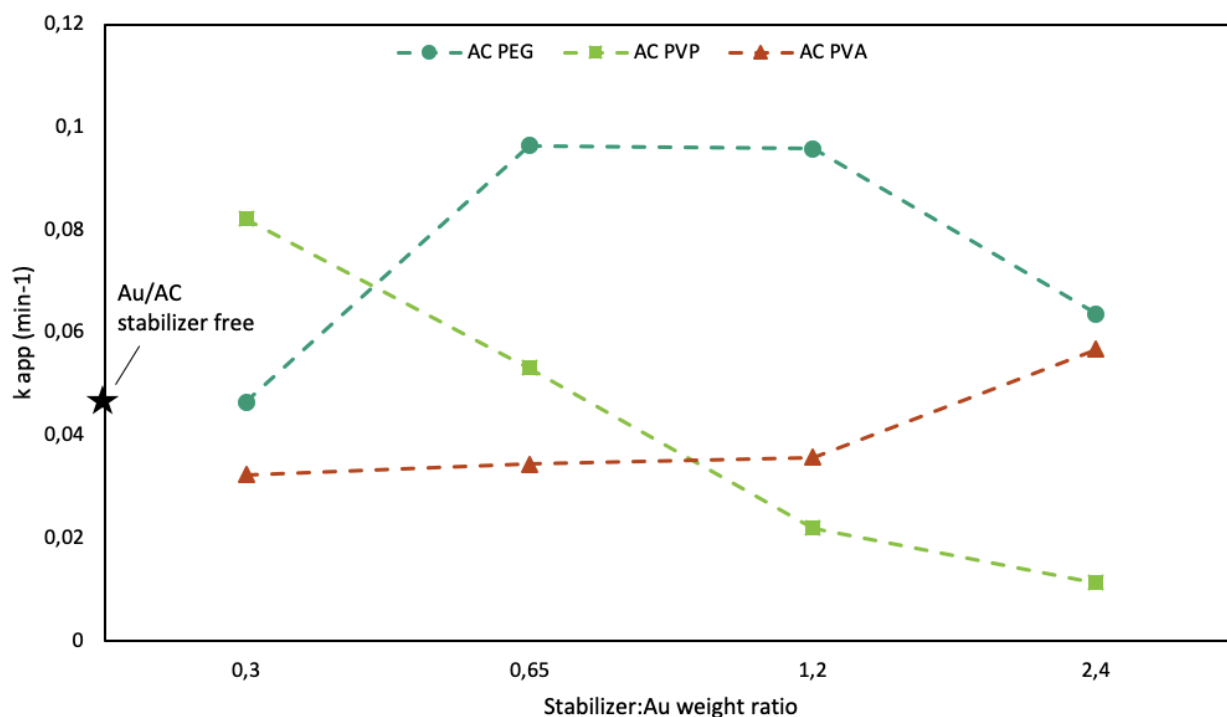

Figure 54 – The values of k_{app} of the three catalyst sets obtained for the 4-nitrphenol reduction with the cuvette setup are plotted against the stabilizer:Au weight ratio.

As far as the Au/AC-PVA set is concerned, the catalytic activity increases as the PVA:Au weight ratio increases. Although for the samples with a PVA:Au ratio from 0,3 to 1,2 k_{app} goes from 0,036 min^{-1} to 0,039 min^{-1}, sample Au/AC-PVA2,4 has a higher k_{app} of 0,059 min^{-1}.

The Au/AC-PVP set instead shows higher activity at the lower PVP:Au weight ratio. The activity decreases as the ratio increases: the catalytic activity of the lower PVP:Au (Au/AC-PVP0,3) is sevenfold the activity of the sample with the highest PVP:Au (Au/AC-PVP2,4), from k_{app} = 0,078 min^{-1} to kapp = 0,011 min^{-1} respectively. Au/AC PVP 0,65 and Au/AC PVP 1,2 show intermediate activity.

The Au/AC PEG set shows comparable activity for the PEG:Au ratios 0,65 (k_{app} = 0,087 min^{-1}) and 1,2 (k_{app} = 0,088 min^{-1}), For the PEG:Au 2,4 ratio the activity decreases (k_{app} = 0,061 min^{-1}) but the least active sample of the set is Au/AC-PEG0,3 with k_{app} = 0,048 min^{-1}.

The sample without stabilizer (Au/AC-PVA0) with a k_{app} of 0,048 min^{-1} has an activity comparable to the samples Au/AC-PEG0,3 and Au/AC-PVP0,65.

4.3.6. Effect of nanoparticle size on catalytic activity

It is well-established that nanoparticle size has a primary influence on catalytic activity. In this section the kinetic constant obtained for nitrophenol reduction with each of the AC-supported Au nanoparticle catalysts is plotted against the respective nanoparticle size, derived from the XRD diffractograms applying the Scherrer equation to obtain the crystallite average size of the Au nanoparticles.
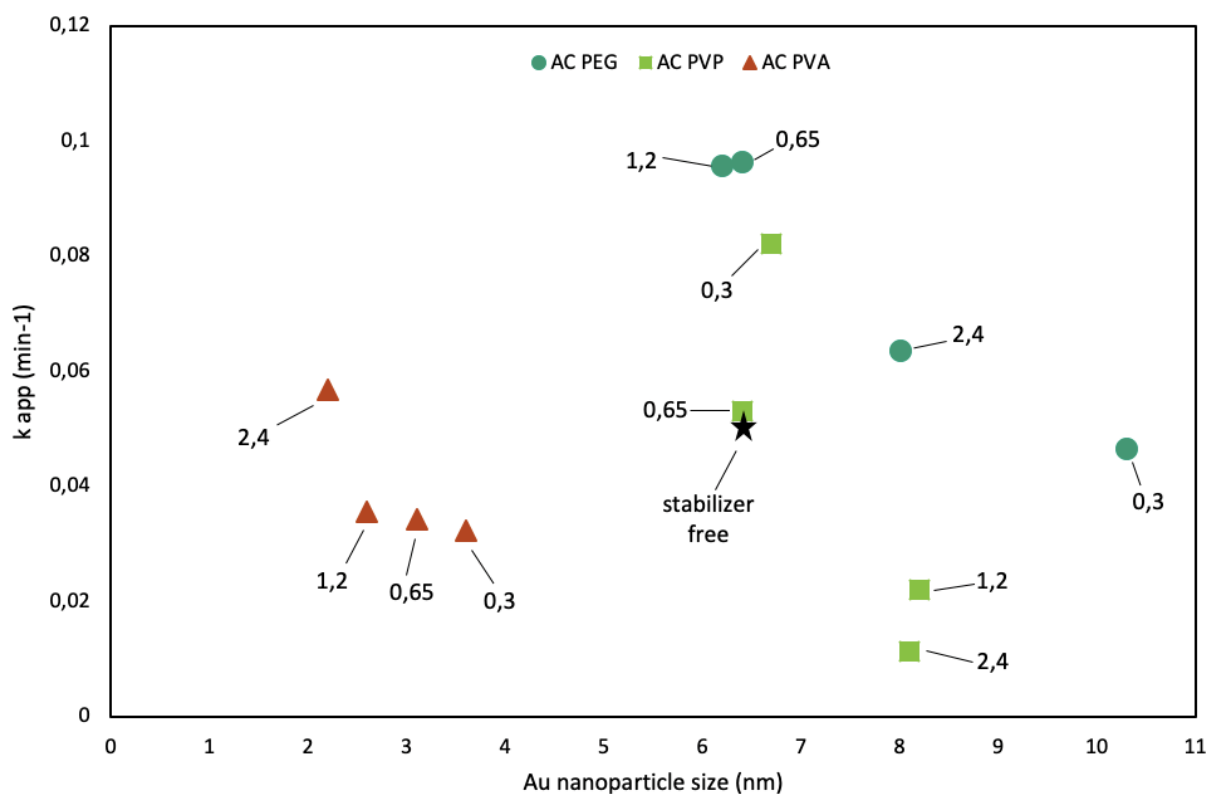

Figure 55 - The values of k_{app} of the three catalyst sets obtained for the 4-nitrphenol reduction with the cuvette setup are plotted against nanoparticle diameter. Labels indicate the polymer:Au weight ratio.

From figure 55 it is possible to notice that for each set it is noted that smaller nanoparticles show higher activity. However, although the Au/AC-PVA set shows the smaller Au nanoparticle sizes, it shows lower catalytically active compared to the other two sets. Au/AC-PEG is the set with an overall better catalytic performance, and the best catalytic performance among the three sets is obtained with the samples Au/AC PEG 0,65 and Au/AC PEG 1,2 (k_{app} = 0,087 min^{-1} and 0,088 min^{-1} respectively). On the other hand, Au/AC PVP set shows very discordant catalytic activities since the sample Au/AC-

PVP0,3 has k_{app} = 0,078 min^{-1} comparable to Au/AC-PEG0,65 and Au/AC-PEG1,2, while sample Au/AC-PVP2,4 and Au/AC-PVP1,2 (k_{app} = 0,028 min^{-1} and 0,011 min^{-1} respectively) have lower catalytic activity than Au/AC-PVA0,3 (has k_{app} = 0,036 min^{-1}).

4.3.7. Effect of support

To get insight on the effect of support for nitrophenol reduction, we tested Au nanoparticles stabilised by PVA at stabiliser:Au weight ratio of 0,65 immobilised onto two different supports, activated carbon and TiO$_2$. The reaction experimental conditions and setup were optimized in this work in section 4.3.2.
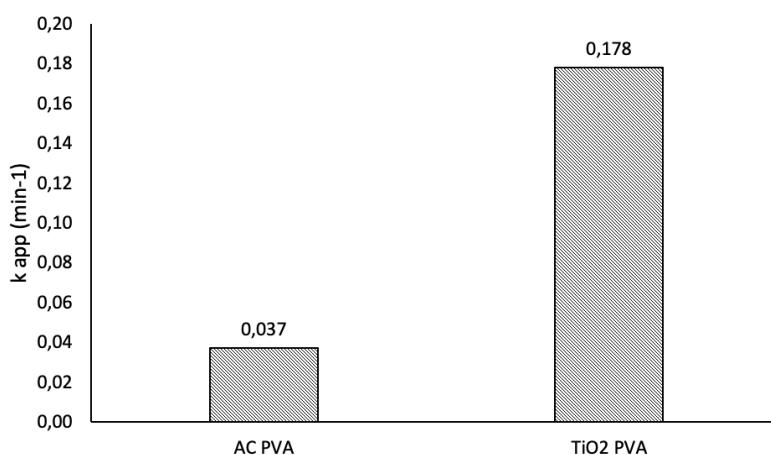

Figure 56 – Apparent kinetic constant for nitrophenol reduction reaction catalysed by Au/AC PVA0,65 (AC PVA) and by Au/TiO$_2$ PVA0,65 (TiO2 PVA). Reaction experimental conditions: [4NP]=1,0*10^{-4}M, NaBH$_4$:4NP=45:1, [catalyst]=80 mg/L, no stirring.

The apparent rate constant of 4-nitrophenol reduction by Au/TiO$_2$ PVA 0,65 (k_{app} = 0,178 min^{-1}) is almost five-fold the k_{app} of the reaction by Au/AC PVA 0,65 (k_{app} = 0,037 min^{-1}). Synergistic interaction between Au nanoparticle and TiO$_2$ appear for this reaction, possibly due to the enhanced electron transfer properties of this material as discussed in a previous paragraph (4.2.2.), however XPS analysis is required for determining the binding energy of the Au and the possible electron transfer between Au and TiO$_2$.

4.3.8. Reusability

Catalyst reusability is an important feature from the point of view of its use in industry. The reusability of the catalyst Au/AC PEG0,6 was tested by repeating the 4-nitrophenol reduction on the same portion of material for 5 cycles after the first reaction with fresh catalyst. Au/AC PEG0,65 was chosen for this test for it gave the highest apparent rate constant for 4-nitrophenol reduction in the experimental conditions optimized in paragraph 4.2.2. The catalyst was separated from the aqueous

solution by centrifugation and was directly used for another cycle, without further treatment or washing.

From figure 57 it is possible to observe that the catalyst undergoes to a gradual deactivation over the 5 cycles. The initial reaction and the first reuse cycle show a similar trend in 4-nitrophenol conversion, reaching >90% conversion in less than 20 minutes. The second reuse cycle shows some deactivation since a conversion value of 90% is reached in 45 minutes. For the third and fourth reuse cycles, the catalyst achieves a 4-nitrophenol conversion of 35% in 60 minutes, after which the reaction was stopped; at the fifth reuse cycle the conversion reached at 60 minutes is 25%.

Deactivation of Au/AC PEG0,65 could be attributed to two different mechanisms. The first is poisoning of the active sites by chemical species in the reaction environment. It is possible that since the protocol used in this test doesn't envisage any washing treatment of the catalyst, the product gradually saturates the catalyst surface. The second is leaching of Au nanoparticles from the catalyst surface to the solution. Finally, a third deactivation mechanism is Au nanoparticle growth on the catalyst surface, up to a size that is catalytically inactive.

A reuse test with a washing step could clarify if this first mechanism is responsible for catalyst deactivation. Further studies on the end-reaction solutions by ICP-AES analysis or any equivalent analytical technique able to detect metal atoms in solution would clarify the presence of Au nanoparticle leaching. TEM imaging of the used catalyst would eventually identify nanoparticle growth phenomena on the catalyst surface.
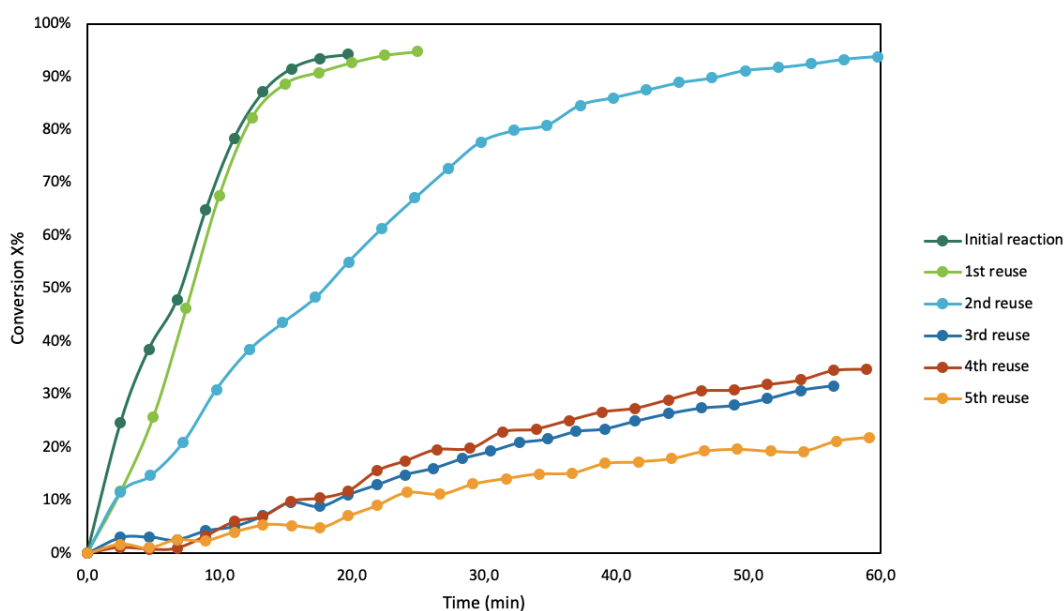

Figure 57 – 4-nitrophenol conversion over time over 5 cycles of reuse after initial reaction with fresh catalyst Au/AC PEG0,65. Reaction experimental conditions: [4NP]=1,0*10^{-4}M, NaBH$_4$:4NP=45:1, [catalyst]=80 mg/L, no stirring.

4.4. Discussion

Gold nanoparticles were synthesized using different polymers as steric stabilisers following the sol-gel procedure. The effect of the amount of stabiliser on nanoparticle formation was studied by UV-vis spectroscopy, while the effect of the polymer type on the stability of the colloidal solution was investigated by means of DLS analysis. PEG and PVP were used as stabilisers at four different values of stabiliser:Au weight ratio. Formation of Au nanoparticles was followed by recording UV-vis spectra immediately after addition of reducing agent to Au precursor solution (initial step of the reduction), and after 30 minutes to monitor if the reduction of the Au precursor has been completed). All the colloidal solutions prepared showed the appearance of the Au nanoparticles' surface plasmon resonance (SPR) peak at about λ=500 nm, with only minor shifts of the SPR peak after 30 minutes. It was possible to conclude from the SPR peak position that the Au nanoparticle colloidal solutions synthesized with PEG and with PVP, at different amounts of the chosen stabiliser, all showed nanoparticle size below 10 nm.

The effect of polymer type on the stability of Au colloidal nanoparticles was investigated. Three Au colloidal solutions prepared using PEG, PVP or PVA in the same amount were analysed at five intervals of time over 5 days. The three polymers had a different effect on nanoparticle size over time. PEG-stabilised Au colloidal nanoparticles showed that nanoparticle growth was concluded after 1h 30 minutes, after which the Au nanoparticles remain stable. PVA-stabilised Au colloidal nanoparticles show a different trend. The nanoparticle size decreased during the first 24 hours and then stabilize without further changes. PVP-stabilised Au colloidal nanoparticles are stable until the 5th day, where a sudden drop in nanoparticle size was recorded.

Polymer nature greatly affects the control over nanoparticle size. The effect of the amount of polymer over Au nanoparticle size depends on its nature. Nevertheless, stabiliser presence is fundamental because it leads to a better nanoparticle dispersion on the support and a narrower nanoparticle size distribution. The effect of PVP:Au and PEG:Au weight ratio on supported nanoparticle size was investigated, comparing the results with the effect of PVA:Au weight ratio on nanoparticle size obtained in previous work[97]. In the latter, it was found that higher PVA concentration led to smaller Au nanoparticles. In this study, we found that PVP concentration gave the opposite trend in nanoparticle size, whereas Au nanoparticle size reaches a minimum at intermediate PEG concentrations.

The catalytic performance of the nanostructured Au based catalysts was evaluated using two model reactions, such as, glucose oxidation to glucaric acid and nitrophenol reduction. We evaluated: the

effect of nanoparticle size, the effect of stabiliser concentration, and the effect of support on catalytic performance.

Catalytic activity is not only dependent on nanoparticle size, but also on polymer nature and concentration. Generally, we have observed blocking of active sites at high polymer concentration (high polymer to metal weight ratio). For both glucose oxidation and 4-nitrophenol reduction, the catalysts with higher polymer concentration showed a diminished catalytic activity. This effect was particularly evident for PVP-stabilised catalysts, where the sample Au/AC PVP 0,3 achieved the highest catalyst activity among the series.

PEG and PVA are likely interacting with Au nanoparticles through diverse active sites of the metal nanoparticle. In fact, PVA-stabilised Au/AC catalyst series showed the worst catalytic performance for 4-nitrophenol reduction, while samples Au/AC PVA 0,3 and Au/AC PVA 0,65 were able to achieve the highest selectivity towards glucaric acid (29,3% and 24,6% respectively), at glucose conversion comparable to the other catalysts. PEG-stabilised Au/AC catalyst series, on the other hand, were almost inactive for glucose oxidation to glucaric acid, with only one catalyst out of four to reach a selectivity to glucaric acid above 4%, but gave the highest apparent reaction rates for 4-nitrophenol reduction.

Furthermore, an increase in Au nanoparticle size with PVP and PEG at high concentration after immobilisation on AC indicates the need to optimize and tune the weight ratio of polymer and metal also for nanoparticle size control. We have observed that for a given catalyst series, among the PEG, PVP, and PVA-stabilised Au/AC catalysts, a better catalytic performance is linked to smaller nanoparticle size. As we have seen earlier, size control by polymer to gold weight ratio is specific to the nature of the polymer and no general trend can be derived.

Finally, Au nanoparticle catalytic activity is influenced by the nature of the support, and the choice of support needs to be optimized to the target reaction. The effect of the nature of the support on catalytic activity was assessed by testing the catalytic activity of Au nanoparticles supported on AC and on TiO_2, stabilized by an equal amount of PVA. AC resulted a better support for glucose oxidation. A higher yield of glucaric acid was obtained with AC (22,4%) against 12,7 % yield obtained with TiO_2. However, for nitrophenol reduction TiO_2-supported Au nanoparticles achieved a higher apparent reaction rate (k_{app} = 0,178 min^{-1}), which is five-fold the reaction rate obtained by AC-supported Au nanoparticles (k_{app} =0,034 min^{-1}).

To elucidate the interactions between the stabiliser-nanoparticle and the support-nanoparticle interactions more characterization is needed by means of TEM, XPS, SEM and by performing CO-DIRFTS and CO chemisorption.

5. Conclusions

Nanostructured catalysts were synthesized following two different methods, MACS and sol-immobilisation.

Materials prepared with MACS showed larger nanoparticles than expected (about 1 nm), with average nanoparticle sizes of 5,9 nm for Ag/TiO_2 and 5,3 nm for Au/TiO_2. XPS analysis showed that Ag undergo oxidation at the interface with the support, increasing oxygen vacancies on TiO_2. A negative shift in Au binding energy suggested that a process of electron transfer from the support to the Au nanoparticle, while no gold oxidation was detected. Elemental analysis of Au/TiO_2 reveled a 0,3% Au atomic composition on the material's surface. Ag/TiO_2 metal loading of 0,15 wt% was determined by ICP-AES. BET surface area of Au/TiO_2 and Ag/TiO_2 showed that the surface area decreases to 24,2 and 23,9 m^2/g respectively, against 28,0 m^2/g of TiO_2 powder. Pore radius decreased from 22,6 Å to 15,6 Å for Ag/TiO_2, that could be attributed to a surface modification after silver oxidation on titanium oxide surface; no pore radius change was measured for Au/TiO_2.

The materials were found to be effective catalysts for nitrophenol ozonation at basic pH and elevated O_3 concentration in the gas feed, with an apparent reaction rate of 0,60 min^{-1} for Au/TiO_2 and 0,55 min^{-1} for Ag/TiO_2, compared to the direct ozonation reaction rate of 0,32 min^{-1}. Isoelectric point of Ag/TiO_2 was determined at pH=4,3. Ag/TiO_2 was also tested for reusability, showing a comparable conversion level after a reaction time of 2 minutes for 5 cycles. The catalysts proved to be active also for 4-NP reduction, although more characterization of the materials is needed to compare the results. Further investigation on both 4-NP ozonation and reduction reaction mechanisms are required to better understand catalyst behavior.

The study of the materials prepared by sol-immobilisation started from the formation of Au nanoparticles in solution. The stability of Au colloidal solutions as the nanoparticles were synthesized with PVA, PEG and PVP as stabilisers was investigated by UV-vis spectroscopy and DLS analysis. Generally, the solutions remained stable without nanoparticle aggregation or precipitation even after 5 days. After nanoparticle immobilisation on AC, XRD analysis for average Au crystallite size revelaled that changing the polymer:Au weight ratio has an effect on nanoparticle size, but the effect depends on the nature of the stabiliser. PVP-stabilised Au nanoparticles increase in size as PVP:Au weight ratio increase, while it appears that a PEG:Au weight ratio between 0,65 and 1,2 gives smaller nanoparticles than lower (0,3:1) or higher (2,4:1) PEG concentrations. Studies of the catalytic activities of Au nanoaprticles supported on AC and stabilized by PVA, PEG or PVP at four different polymer:Au weight ratios showed polymer concentration and polymer nature strongly affect catalytic activity at least as much as nanoparticle size. At high polymer concentrations, catalytic activity is

inhibited regardless of the polymer nature. PEG, PVP and PVA interact with the supported Au nanoparticles through different active sites. PEG-stabilised Au/AC catalysts, compared to PVP and PVA counterparts, achieved the highest reaction rates for nitrophenol reduction, while for glucose oxidation reaction glucaric acid yield was very limited. PVA-stabilised Au nanoparticles on the other hand showed opposite behavior: they allowed the best catalytic performances for glucose oxidation to glucaric acid but were by far the least active catalysts for nitrophenol reduction. PVP as stabliser seems to have strong interactions with Au nanoparticles as catalytic activity for nitrophenol reduction drops as the PVP:Au weight ratio increases, suggesting a saturation of the active sites; a similar but less pronounced trend is observable in glucaric acid yield. Finally, the support was found to have an influence on the active sites of the Au nanoparticles. TiO_2, a semi-conductor known for allowing electron transfers with Au nanoparticles, was found to be the best support for nitrophenol reduction as the reaction rate for Au/TiO_2 PVA 0,65 was five-fold the reaction rate of Au/AC PVA 0,65. At the same time, TiO_2-supported nanoparticles are less active for glucose oxidation, indicated by a higher glucose isomer presence and lower glucaric acid yield.

6. Future work

The results presented in this thesis highlighted the importance of the different parts that compose a nanocatalyst: catalytic activity of Au nanoparticles was affected not only by its characteristics, in this case nanoparticle size, but also by the stabiliser and the support. As the research in this field moves forward, it is becoming more evident that support and stabilisers cannot be seen as passive elements on a nanostructured material.

From the results presented in this thesis, further work can be envisaged to clarify the interaction between supported Au nanoparticles and the stabilisers: a detailed characterization by TEM imaging could give more information on the nanoparticle size distribution and nanoparticle dispersion on the catalyst, XPS, SEM, CO-DRIFTS and CO chemisorption of materials are useful techniques to investigate the influence on the active sites of the nanoparticle interactions with support and stabilisers. Furthermore, new materials could be synthesized by changing the support and stabiliser, for example PEG or PVP-stabilised Au nanoparticles on TiO_2, for the investigation of support-stabiliser interactions.

Another field of study is catalyst reusability, by investigation of stability of supported Au nanoparticles after one or more reaction cycles. Clarification of deactivation mechanisms can give indications on the characteristics that should be imparted to a nanocatalyst for industrial use. ICP-AES, TEM, XPS, SEM-EDX are some of the techniques that can be used for this purpose.

7. Bibliography

1. Liu, L. & Corma, A. Metal Catalysts for Heterogeneous Catalysis: From Single Atoms to Nanoclusters and Nanoparticles. *Chem. Rev.* **118**, 4981–5079 (2018).
2. Okumura, M., Fujitani, T., Huang, J. & Ishida, T. A Career in Catalysis: Masatake Haruta. *ACS Catal.* **5**, 4699–4707 (2015).
3. Palmer, R. E., Cai, R. & Vernieres, J. Synthesis without Solvents: The Cluster (Nanoparticle) Beam Route to Catalysts and Sensors. *Acc. Chem. Res.* **51**, 2296–2304 (2018).
4. Miklos, D. B. *et al.* Evaluation of advanced oxidation processes for water and wastewater treatment – A critical review. *Water Res.* **139**, 118–131 (2018).
5. Zhao, P., Feng, X., Huang, D., Yang, G. & Astruc, D. Basic concepts and recent advances in nitrophenol reduction by gold- and other transition metal nanoparticles. *Coord. Chem. Rev.* **287**, 114–136 (2015).
6. Somorjai, G. A. & Carrazza, J. Structure sensitivity of catalytic reactions. *Ind. Eng. Chem. Fundam.* **25**, 63–69 (1986).
7. Collier, C. P., Saykally, R. J., Shiang, J. J., Henrichs, S. E. & Heath, J. R. Reversible Tuning of Silver Quantum Dot Monolayers Through the Metal-Insulator Transition. *Science* **277**, 1978–1981 (1997).
8. Schön, G. & Simon, U. A fascinating new field in colloid science: small ligand-stabilized metal clusters and possible application in microelectronics. *Colloid Polym. Sci.* **273**, 101–117 (1995).
9. Storhoff, J. J. & Mirkin, C. A. Programmed Materials Synthesis with DNA. *Chem. Rev.* **99**, 1849–1862 (1999).
10. Yu, S. & Jain, P. K. Plasmonic photosynthesis of C 1 –C 3 hydrocarbons from carbon dioxide assisted by an ionic liquid. *Nat. Commun.* **10**, 1–7 (2019).
11. Hashmi, A. S. K. & Hutchings, G. J. Gold Catalysis. *Angew. Chem. Int. Ed.* **45**, 7896–7936 (2006).
12. Villa, A. *et al.* Characterisation of gold catalysts. *Chem. Soc. Rev.* **45**, 4953–4994 (2016).
13. Buceta, D., Piñeiro, Y., Vázquez-Vázquez, C., Rivas, J. & López-Quintela, M. A. Metallic Clusters: Theoretical Background, Properties and Synthesis in Microemulsions. *Catalysts* **4**, 356–374 (2014).
14. Haruta, M., Kobayashi, T., Sano, H. & Yamada, N. Novel Gold Catalysts for the Oxidation of Carbon Monoxide at a Temperature far Below 0 °C. *Chem. Lett.* **16**, 405–408 (1987).
15. Hutchings, G. J. Vapor phase hydrochlorination of acetylene: correlation of catalytic activity of supported metal chloride catalysts. *J. Catal.* **96**, 292–295 (1985).
16. Haruta, M. Size- and support-dependency in the catalysis of gold. *Catal. Today* **36**, 153–166 (1997).
17. Prati, L. & Martra, G. New gold catalysts for liquid phase oxidation. *Gold Bull.* **32**, 96–101 (1999).
18. Araki, J. Electrostatic or steric? – preparations and characterizations of well-dispersed systems containing rod-like nanowhiskers of crystalline polysaccharides. *Soft Matter* **9**, 4125–4141 (2013).
19. Fritz, G., Schädler, V., Willenbacher, N. & Wagner, N. J. Electrosteric Stabilization of Colloidal Dispersions. *Langmuir* **18**, 6381–6390 (2002).
20. Chiu, C.-Y., Chung, P.-J., Lao, K.-U., Liao, C.-W. & Huang, M. H. Facet-Dependent Catalytic Activity of Gold Nanocubes, Octahedra, and Rhombic Dodecahedra toward 4-Nitroaniline Reduction. *J. Phys. Chem. C* **116**, 23757–23763 (2012).
21. Dimitratos, N. *et al.* Effect of the preparation method of supported Au nanoparticles in the liquid phase oxidation of glycerol. *Appl. Catal. Gen.* **514**, 267–275 (2016).
22. Jia, C.-J. & Schüth, F. Colloidal metal nanoparticles as a component of designed catalyst. *Phys. Chem. Chem. Phys.* **13**, 2457–2487 (2011).
23. Wegner, K., Piseri, P., Tafreshi, H. V. & Milani, P. Cluster beam deposition: a tool for nanoscale science and technology. *J. Phys. Appl. Phys.* **39**, R439–R459 (2006).
24. Oiko, V. T. A., Mathieu, T., Cao, L., Liu, J. & Palmer, R. E. Note: Production of silver nanoclusters using a Matrix-Assembly Cluster Source with a solid CO2 matrix. *J. Chem. Phys.* **145**, 166101 (2016).
25. Ellis, P. R. *et al.* The cluster beam route to model catalysts and beyond. *Faraday Discuss.* **188**, 39–56 (2016).
26. Haruta, M., Yamada, N., Kobayashi, T. & Iijima, S. Gold catalysts prepared by coprecipitation for low-temperature oxidation of hydrogen and of carbon monoxide. *J. Catal.* **115**, 301–309 (1989).
27. Tada, K. *et al.* DFT calculations for Au adsorption onto a reduced TiO2 (110) surface with the coexistence of Cl. *Mol. Phys.* **112**, 365–378 (2014).
28. Haruta, M. *et al.* Low-Temperature Oxidation of CO over Gold Supported on TiO2, α-Fe2O3, and Co3O4. *J. Catal.* **144**, 175–192 (1993).
29. Sharma, A. S., Kaur, H. & Shah, D. Selective oxidation of alcohols by supported gold nanoparticles: recent advances. *RSC Adv.* **6**, 28688–28727 (2016).
30. Gluhoi, A. C., Bakker, J. W. & Nieuwenhuys, B. E. Gold, still a surprising catalyst: Selective hydrogenation of acetylene to ethylene over Au nanoparticles. *Catal. Today* **154**, 13–20 (2010).
31. Segura, Y., López, N. & Pérez-Ramírez, J. Origin of the superior hydrogenation selectivity of gold nanoparticles in alkyne + alkene mixtures: Triple- versus double-bond activation. *J. Catal.* **247**, 383–386 (2007).
32. Hayashi, T., Tanaka, K. & Haruta, M. Selective Vapor-Phase Epoxidation of Propylene over Au/TiO2Catalysts in the Presence of Oxygen and Hydrogen. *J. Catal.* **178**, 566–575 (1998).

33. Suzuki, K. *et al.* Aerobic Oxidative Esterification of Aldehydes with Alcohols by Gold–Nickel Oxide Nanoparticle Catalysts with a Core–Shell Structure. *ACS Catal.* **3**, 1845–1849 (2013).

34. Wunder, S., Lu, Y., Albrecht, M. & Ballauff, M. Catalytic Activity of Faceted Gold Nanoparticles Studied by a Model Reaction: Evidence for Substrate-Induced Surface Restructuring. *ACS Catal.* **1**, 908–916 (2011).

35. Wunder, S., Polzer, F., Lu, Y., Mei, Y. & Ballauff, M. Kinetic Analysis of Catalytic Reduction of 4-Nitrophenol by Metallic Nanoparticles Immobilized in Spherical Polyelectrolyte Brushes. *J. Phys. Chem. C* **114**, 8814–8820 (2010).

36. Seo, E. *et al.* Double Hydrophilic Block Copolymer Templated Au Nanoparticles with Enhanced Catalytic Activity toward Nitroarene Reduction. *J. Phys. Chem. C* **117**, 11686–11693 (2013).

37. Hayakawa, K., Yoshimura, T. & Esumi, K. Preparation of Gold−Dendrimer Nanocomposites by Laser Irradiation and Their Catalytic Reduction of 4-Nitrophenol. *Langmuir* **19**, 5517–5521 (2003).

38. Wang, X. *et al.* Reduced state carbon dots as both reductant and stabilizer for the synthesis of gold nanoparticles. *Carbon* **64**, 499–506 (2013).

39. Hu, W. *et al.* A magnetic double-shell microsphere as a highly efficient reusable catalyst for catalytic applications. *Chem. Commun.* **49**, 7596–7598 (2013).

40. Zeng, J., Zhang, Q., Chen, J. & Xia, Y. A Comparison Study of the Catalytic Properties of Au-Based Nanocages, Nanoboxes, and Nanoparticles. *Nano Lett.* **10**, 30–35 (2010).

41. Wu, T. *et al.* Fabrication of graphene oxide decorated with Au–Ag alloy nanoparticles and its superior catalytic performance for the reduction of 4-nitrophenol. *J. Mater. Chem. A* **1**, 7384–7390 (2013).

42. Zhang, P. *et al.* Facile fabrication of faceted copper nanocrystals with high catalytic activity for p-nitrophenol reduction. *J. Mater. Chem. A* **1**, 1632–1638 (2013).

43. Wang, Z., Xu, C., Gao, G. & Li, X. Facile synthesis of well-dispersed Pd–graphene nanohybrids and their catalytic properties in 4-nitrophenol reduction. *RSC Adv.* **4**, 13644–13651 (2014).

44. Kaiser, J. *et al.* Catalytic activity of nanoalloys from gold and palladium. *Phys. Chem. Chem. Phys.* **14**, 6487–6495 (2012).

45. ATSDR - Toxicological Profile: Nitrophenols. https://www.atsdr.cdc.gov/ToxProfiles/tp.asp?id=880&tid=172.

46. Tizaoui, C., Mezughi, K. & Bickley, R. Heterogeneous photocatalytic removal of the herbicide clopyralid and its comparison with UV/H2O2 and ozone oxidation techniques. *Desalination* **273**, 197–204 (2011).

47. Xing, S. *et al.* Mechanism for catalytic ozonation of p-nitrophenol in water with titanate nanotube supported manganese oxide. *RSC Adv.* **5**, 101975–101981 (2015).

48. Xiong, Z. *et al.* Degradation of p-nitrophenol (PNP) in aqueous solution by a micro-size Fe0/O3 process (mFe0/O3): Optimization, kinetic, performance and mechanism. *Chem. Eng. J.* **302**, 137–145 (2016).

49. Loos, R. *et al.* EU-wide survey of polar organic persistent pollutants in European river waters. *Environ. Pollut. Barking Essex 1987* **157**, 561–568 (2009).

50. Gu, L., Zhang, X. & Lei, L. Degradation of Aqueous p-Nitrophenol by Ozonation Integrated with Activated Carbon. *Ind. Eng. Chem. Res.* **47**, 6809–6815 (2008).

51. Sotelo, J. L., Beltran, F. J., Benitez, F. J. & Beltran-Heredia, J. Ozone decomposition in water: kinetic study. *Ind. Eng. Chem. Res.* **26**, 39–43 (1987).

52. Beltrán, F. J., Rivas, F. J. & Montero-de-Espinosa, R. Catalytic ozonation of oxalic acid in an aqueous TiO2 slurry reactor. *Appl. Catal. B Environ.* **39**, 221–231 (2002).

53. Beltrán, F. J., Rivas, J., Álvarez, P. & Montero-de-Espinosa, R. Kinetics of Heterogeneous Catalytic Ozone Decomposition in Water on an Activated Carbon. *Ozone Sci. Eng.* **24**, 227–237 (2002).

54. Nawrocki, J. & Kasprzyk-Hordern, B. The efficiency and mechanisms of catalytic ozonation. *Appl. Catal. B Environ.* **99**, 27–42 (2010).

55. Pines, D. S. & Reckhow, D. A. Effect of Dissolved Cobalt(II) on the Ozonation of Oxalic Acid. *Environ. Sci. Technol.* **36**, 4046–4051 (2002).

56. Beltrán, F. J. *Ozone reaction kinetics for water and wastewater systems*. (Lewis Publishers, 2004).

57. Gracia, R., Cortés, S., Sarasa, J., Ormad, P. & Ovelleiro, J. L. Catalytic Ozonation with Supported Titanium Dioxide. The Stability of Catalyst in Water. *Ozone Sci. Eng.* **22**, 185–193 (2000).

58. Valand, J., Maddila, S., Friedrich, H. B. & Jonnalagadda, S. B. Heterogeneous Catalyzed Ozonation using Cu-Ni-Co Oxides for Degradation of Dichlorophenol. *Ozone Sci. Eng.* **38**, 14–24 (2016).

59. Yang, L., Hu, C., Nie, Y. & Qu, J. Catalytic Ozonation of Selected Pharmaceuticals over Mesoporous Alumina-Supported Manganese Oxide. *Environ. Sci. Technol.* **43**, 2525–2529 (2009).

60. Lin, J., Kawai, A. & Nakajima, T. Effective catalysts for decomposition of aqueous ozone. *Appl. Catal. B Environ.* **39**, 157–165 (2002).

61. Imamura, S., Ikebata, M., Ito, T. & Ogita, T. Decomposition of ozone on a silver catalyst. *Ind. Eng. Chem. Res.* **30**, 217–221 (1991).

62. Morozov, P. A., Abkhalimov, E. V., Chalykh, A. E., Pisarev, S. A. & Ershov, B. G. Interaction of silver nanoparticles with ozone in aqueous solution. *Colloid J.* **73**, 248–252 (2011).

63. Reisz, E., Naumov, S., Schmidt, W. & von Sonntag, C. Reaction of Ozone with Ag(I)—Mechanistic Considerations. *Ozone Sci. Eng.* **37**, 393–404 (2015).

64. Ramachandran, S., Fontanille, P., Pandey, A. & Larroche, C. Gluconic Acid: Properties, Applications and Microbial Production. 11 (2006).

65. Werpy, T. & Petersen, G. *Top Value Added Chemicals from Biomass: Volume I -- Results of Screening for Potential Candidates from Sugars and Synthesis Gas*. DOE/GO-102004-1992, 15008859 http://www.osti.gov/servlets/purl/15008859/ (2004) doi:10.2172/15008859.

66. Moon, T. S., Yoon, S.-H., Lanza, A. M., Roy-Mayhew, J. D. & Prather, K. L. J. Production of glucaric acid from a synthetic pathway in recombinant Escherichia coli. *Appl. Environ. Microbiol.* **75**, 589–595 (2009).

67. Merbouh, N., Francois Thaburet, J., Ibert, M., Marsais, F. & Bobbitt, J. M. Facile nitroxide-mediated oxidations of d-glucose to d-glucaric acid. *Carbohydr. Res.* **336**, 75–78 (2001).

68. Bin, D. *et al.* Controllable oxidation of glucose to gluconic acid and glucaric acid using an electrocatalytic reactor. *Electrochimica Acta* **130**, 170–178 (2014).

69. Zhang, Z. & Huber, G. W. Catalytic oxidation of carbohydrates into organic acids and furan chemicals. *Chem. Soc. Rev.* **47**, 1351–1390 (2018).

70. Biella, S., Prati, L. & Rossi, M. Selective Oxidation of D-Glucose on Gold Catalyst. *J. Catal.* **206**, 242–247 (2002).

71. Önal, Y., Schimpf, S. & Claus, P. Structure sensitivity and kinetics of d-glucose oxidation to d-gluconic acid over carbon-supported gold catalysts. *J. Catal.* **223**, 122–133 (2004).

72. Comotti, M., Della Pina, C., Falletta, E. & Rossi, M. Aerobic Oxidation of Glucose with Gold Catalyst: Hydrogen Peroxide as Intermediate and Reagent. *Adv. Synth. Catal.* **348**, 313–316 (2006).

73. R, S., N, D. & U, P. D-Glucose Oxidation with H2O2 on an Au/Al2O3 catalyst. *Appl. Catal. B Environ.* **102**, 584–589 (2011).

74. Lee, J., Saha, B. & Vlachos, D. G. Pt catalysts for efficient aerobic oxidation of glucose to glucaric acid in water. *Green Chem.* **18**, 3815–3822 (2016).

75. Derrien, E. *et al.* Aerobic Oxidation of Glucose to Glucaric Acid under Alkaline-Free Conditions: Au-Based Bimetallic Catalysts and the Effect of Residues in a Hemicellulose Hydrolysate. *Ind. Eng. Chem. Res.* **56**, 13175–13189 (2017).

76. Solmi, S., Morreale, C., Ospitali, F., Agnoli, S. & Cavani, F. Oxidation of Glucose to Glucaric Acid Using Au/C Catalysts. *ChemCatChem* **9**, 2797–2806 (2017).

77. Palmer, R. E., Cao, L. & Yin, F. Note: Proof of principle of a new type of cluster beam source with potential for scale-up. *Rev. Sci. Instrum.* **87**, 046103 (2016).

78. Lim, D. C., Lopez-Salido, I., Dietsche, R., Bubek, M. & Kim, Y. D. Size-selectivity in the oxidation behaviors of au nanoparticles. *Angew. Chem. Int. Ed Engl.* **45**, 2413–2415 (2006).

79. Radnik, J., Mohr, C. & Claus, P. On the origin of binding energy shifts of core levels of supported gold nanoparticles and dependence of pretreatment and material synthesis. *Phys. Chem. Chem. Phys.* **5**, 172–177 (2003).

80. Seah, M. P., Gilmore, I. S. & Beamson, G. XPS: binding energy calibration of electron spectrometers 5—re-evaluation of the reference energies. *Surf. Interface Anal.* **26**, 642–649 (1998).

81. Kaushik, V. K. XPS core level spectra and Auger parameters for some silver compounds. *J. Electron Spectrosc. Relat. Phenom.* **56**, 273–277 (1991).

82. Porkovich, A. *et al.* In Situ Observation of Metal to Metal Oxide Progression: A Study of Charge Transfer Phenomenon at Ru-CuO Interfaces. *ACS Nano* **13**, 12425–12437 (2019).

83. Kruse, N. & Chenakin, S. XPS characterization of Au/TiO2 catalysts: Binding energy assessment and irradiation effects. *Appl. Catal. Gen.* **391**, 367–376 (2011).

84. Yu, C.-P. & Yu, Y.-H. Mechanisms of the Reaction of Ozone with p-Nitrophenol. *Ozone Sci. Eng.* **23**, 303–312 (2001).

85. Nawrocki, J. Catalytic ozonation in water: Controversies and questions. Discussion paper. *Appl. Catal. B Environ.* **142–143**, 465–471 (2013).

86. Beltrán, F. J., Gómez-Serrano, V. & Durán, A. Degradation kinetics of p-nitrophenol ozonation in water. *Water Res.* **26**, 9–17 (1992).

87. Liu, J.-N. *et al.* Ozone/graphene oxide catalytic oxidation: a novel method to degrade emerging organic contaminant N, N-diethyl-m-toluamide (DEET). *Sci. Rep.* **6**, 31405 (2016).

88. Jin, X., Peldszus, S. & Huck, P. M. Reaction kinetics of selected micropollutants in ozonation and advanced oxidation processes. *Water Res.* **46**, 6519–6530 (2012).

89. Ershov, B. G. & Morozov, P. A. The kinetics of ozone decomposition in water, the influence of pH and temperature. *Russ. J. Phys. Chem. A* **83**, 1295–1299 (2009).

90. Dhandapani, B. & Oyama, S. T. Gas phase ozone decomposition catalysts. *Appl. Catal. B Environ.* **11**, 129–166 (1997).

91. Signoretto, M., Menegazzo, F., Di Michele, A. & Fioriniello, E. Effects of Support and Synthetic Procedure for Sol-Immobilized Au Nanoparticles. *Catalysts* **6**, 87 (2016).

92. Rahme, K., Gauffre, F., Marty, J.-D., Payré, B. & Mingotaud, C. A Systematic Study of the Stabilization in Water of Gold Nanoparticles by Poly(Ethylene Oxide)−Poly(Propylene Oxide)−Poly(Ethylene Oxide) Triblock Copolymers. *J. Phys. Chem. C* **111**, 7273–7279 (2007).

93. Deniz, A. E., Vural, H. A., Ortaç, B. & Uyar, T. Gold nanoparticle/polymer nanofibrous composites by laser ablation and electrospinning. *Mater. Lett.* **65**, 2941–2943 (2011).

94. Koczkur, K. M., Mourdikoudis, S., Polavarapu, L. & Skrabalak, S. E. Polyvinylpyrrolidone (PVP) in nanoparticle synthesis. *Dalton Trans.* **44**, 17883–17905 (2015).

95. Bianchi, C. L., Canton, P., Dimitratos, N., Porta, F. & Prati, L. Selective oxidation of glycerol with oxygen using mono and bimetallic catalysts based on Au, Pd and Pt metals. *Catal. Today* **102–103**, 203–212 (2005).

96. Dasog, M., Hou, W. & Scott, R. W. J. Controlled growth and catalytic activity of gold monolayer protected clusters in presence of borohydride salts. *Chem. Commun.* **47**, 8569–8571 (2011).

97. Soto, C. A. G., Dimitratos, N. & Monti, E. Investigation of gold-based catalysts for liquid phase oxidation of glucose to glucaric acid. (2019).

98. Sanchez, F. *et al.* Investigation of the Catalytic Performance of Pd/CNFs for Hydrogen Evolution from Additive-Free Formic Acid Decomposition. *C — J. Carbon Res.* **4**, 26 (2018).

99. McEntee, M., Stevanovic, A., Tang, W., Neurock, M. & Yates, J. T. Electric Field Changes on Au Nanoparticles on Semiconductor Supports – The Molecular Voltmeter and Other Methods to Observe Adsorbate-Induced Charge-Transfer Effects in Au/TiO2 Nanocatalysts. *J. Am. Chem. Soc.* **137**, 1972–1982 (2015).

100. Haydar, S., Ferro-García, M. A., Rivera-Utrilla, J. & Joly, J. P. Adsorption of p-nitrophenol on an activated carbon with different oxidations. *Carbon* **41**, 387–395 (2003).

101. Liu, X., Wang, F. & Bai, S. Kinetics and equilibrium adsorption study of p-nitrophenol onto activated carbon derived from walnut peel. *Water Sci. Technol.* **72**, 2229–2235 (2015).

102. Motta, D. *et al.* Preformed Au colloidal nanoparticles immobilised on NiO as highly efficient heterogeneous catalysts for reduction of 4-nitrophenol to 4-aminophenol. *J. Environ. Chem. Eng.* **7**, 103381 (2019).

103. Abis, L., Dimitratos, N., Sankar, M., Freakley, S. J. & Hutchings, G. J. The Effect of Polymer Addition on Base Catalysed Glycerol Oxidation Using Gold and Gold–Palladium Bimetallic Catalysts. *Top. Catal.* (2019) doi:10.1007/s11244-019-01212-y.
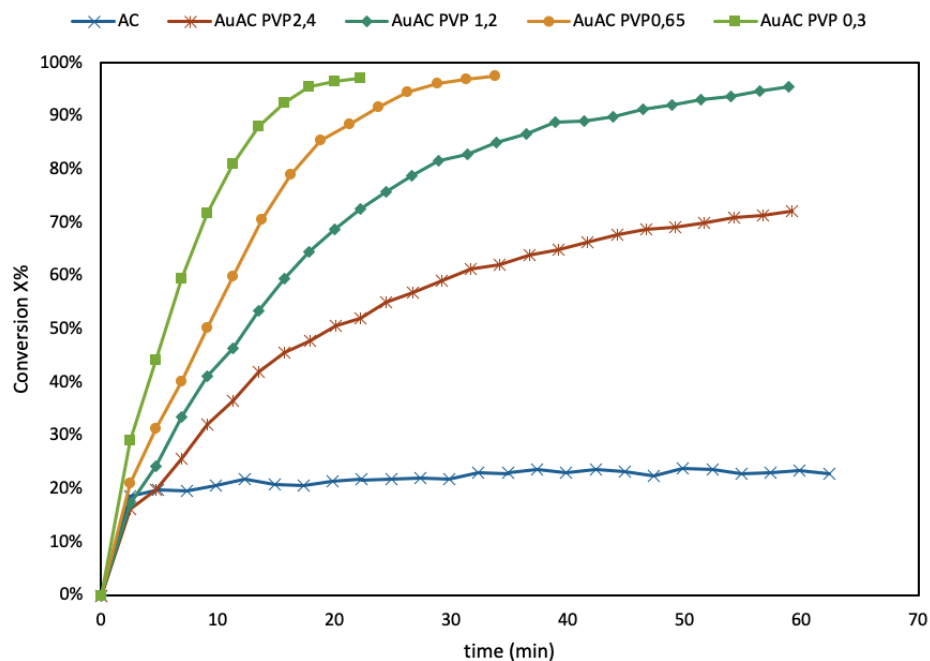
8. Supporting information

Figure S1.a – 4-nitrophenol conversion from catalytic reduction with Au/AC PVP set carried out using the cuvette setup. Reaction conditions: [4-NP] = $1,0x10^{-4}$ M, [NaBH$_4$] = $4,5x10^{-3}$ M, V= 50 mL, [catalyst] = 80 mg/L, no stirring.
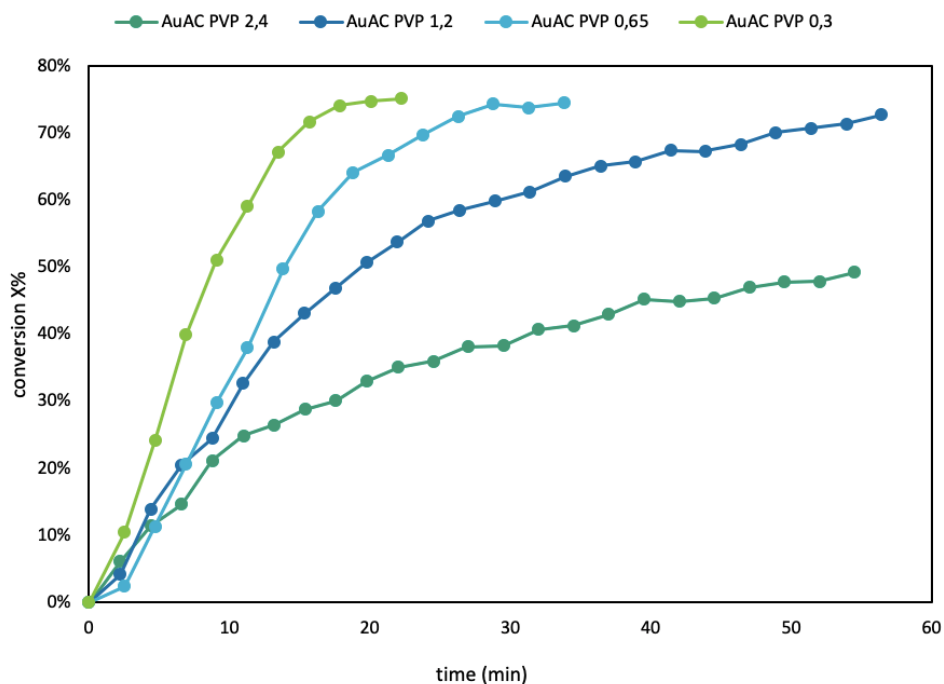

Figure S1.b - Extrapolated conversion for Au/AC PVP set, to highlight the catalytic 4-nitrophenol reduction by supported Au nanoparticles.
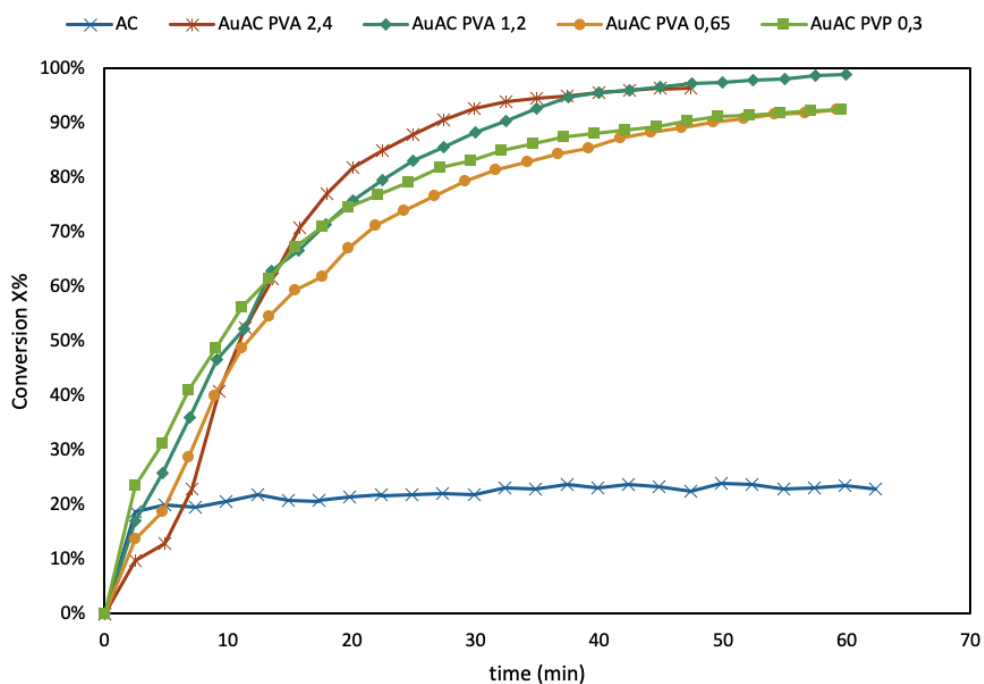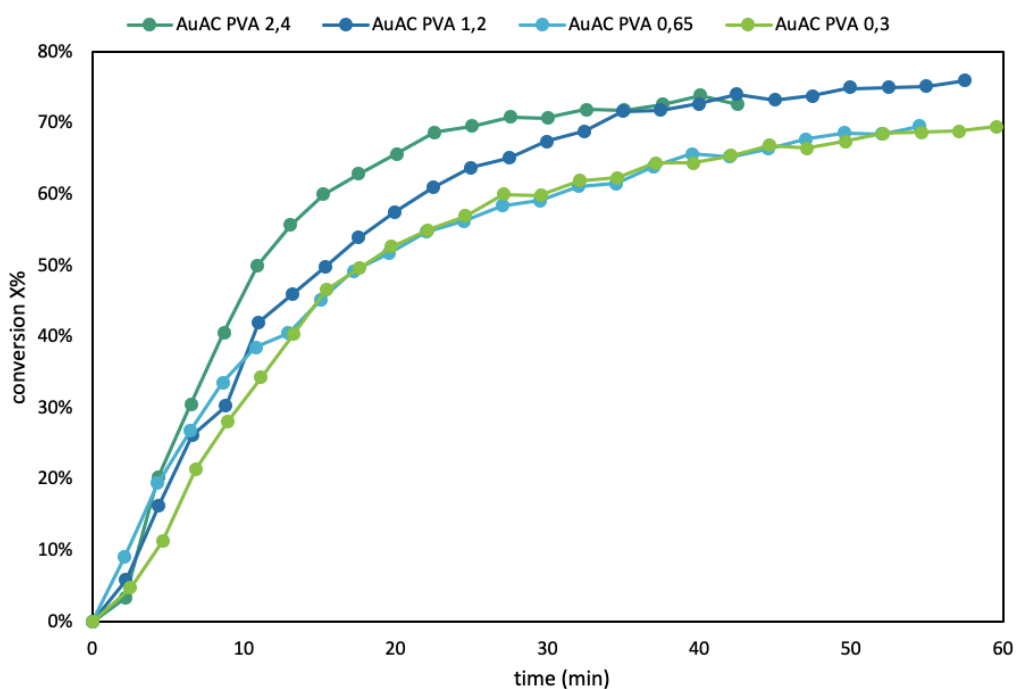
Figure S2.a – 4-nitrophenol conversion from catalytic reduction with Au/AC PVA set carried out using the cuvette setup. Reaction conditions: [4-NP] = $1{,}0 \times 10^{-4}$ M, [NaBH$_4$] = $4{,}5 \times 10^{-3}$ M, V= 50 mL, [catalyst] = 80 mg/L, no stirring.

Figure S2.b - Extrapolated conversion for Au/AC PVA set, to highlight the catalytic 4-nitrophenol reduction by supported Au nanoparticles.
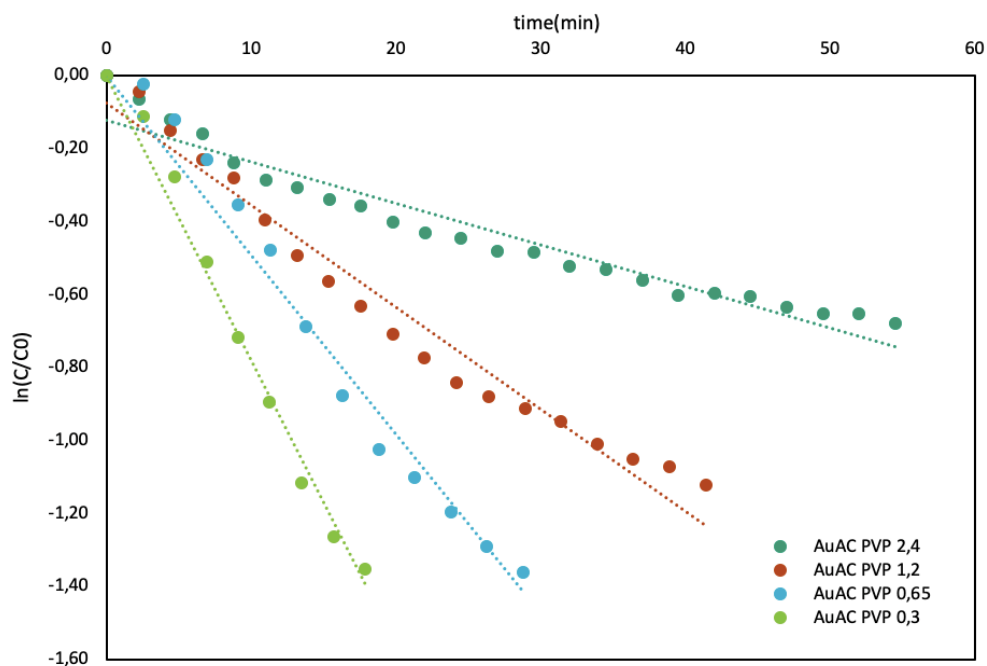
Figure S3.a - The pseudo first-order reaction curves for the 4-nitrophenol catalytic reduction by Au/AC PVP set of catalyst.
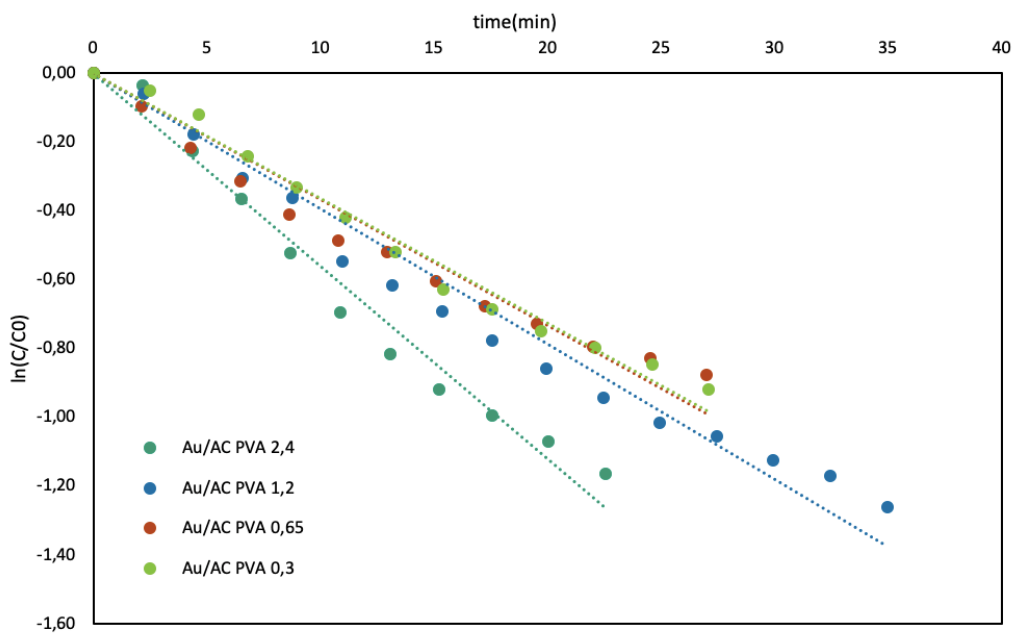

Figure S3.b - The pseudo first-order reaction curves for the 4-nitrophenol catalytic reduction by Au/AC PVA set of catalysts.